POLITECNICO DI TORINO

Corso di Laurea Magistrale
in Ingegneria Matematica

Tesi di Laurea Magistrale

A Particle-Based Analysis of the Saltation Process

Models, Numerical Methods and Tests

Relatori
prof. Luigi Preziosi
dott. Roberto Nuca

Candidato
Nicolò Perello

Anno Accademico 2020-2021

Abstract

Windblown sand transport is one of the most important natural erosion mechanism in arid zones. It is responsible for landform dynamics, dust aerosols emission and for damaging human infrastructure.
In this thesis we present a particle-based numerical model in order to simulate the *saltation* phenomenon, that is the sand transport mode involving most of the transported mass under normal wind conditions. The model takes into account the fundamental physical aspects of the saltation process, which are essentially the entrainment of particles by wind, their trajectories and their impact on the ground. Starting from basic principles of single particle behaviour, the aim of the model is to obtain information on global saltation quantities, such as the sand particle concentration with respect to ground distance and the sand mass flux with respect to the wind strenght.
In the first part of the thesis the physics of saltation is presented, highlighting its main features and the most critical aspects in the process description. This phenomenon is characterized by random behaviour, due to both the presence of a turbulent flow and the random shape and arrangement of the sand grains. This randomness makes the measurement of the descriptive quantities of saltation and its modelling complex to define. Many aspects involved in the process remain uncertain and debated. The development of numerical models can help shed light on some of these issues.
The particle trajectories are studied in detail in Chapter 2 in order to understand the role of wind flow as an external source of energy. Then, in Chapter 3 a numerical model for the saltation process is proposed, with a focus on the simulation algorithms and their extendibility to future improvements. The grain-bed impact dynamics is described by energy-based models without directly simulating the deterministic interaction between particles. We model the complex impact mechanism by means of stochastic approaches. This allows us to reproduce randomness of grain-bed impact due to random shape of particles and their arrangement on the sand bed. Several impact models are proposed in Chapter 4. In Chapter 5 we present results obtained from numerical simulations.

Acknowledgements

My most sincere and warmest thanks go to my supervisors, prof. Luigi Preziosi and Dr. Roberto Nuca, professor Preziosi for his valuable and helpful advice during my thesis work, and for his guidance in tackling this challenge, Roberto for his support during these months, for the lessons he has taught me and for his patience.
In particular, this thesis was carried out in collaboration with Roberto Nuca during his PhD. Starting from a basic idea that he introduced in the very last part of his PhD research activity we collaborated to develop his concept and to research new results. The research for his PhD has been carried out within the project: "Sand Mitigation around Railway Tracks" (SMaRT). The SMaRT project was conducted in the framework of Marie Skłodowska-Curie Actions (MSCA), Innovative Training Network (ITN), European Industrial Doctorate (EID), call H2020-MSCA-ITN-2016 (www.smart-eid.eu). The project received funding from the European Union Horizon 2020 research and innovation program under grant agreement No721798.

Contents

List of Tables

List of Figures

Chapter 1

The Wind-Blown Sand Process

The processes related to emission, transport and deposition of materials like sand and dust by the wind are called *aeolian processes*. These phenomena mainly occur in arid zones as deserts, beaches or dry lake beds where there is the availability of granular material and wind acts with a more powerful eroding force. When the wind speed increases and reaches enough force to lift particles from the ground, the process starts. First particles of a small diameter start hopping initially covering small stretches. Then, if the wind continues to blow with sufficient force, the distances covered increase. When particles gain sufficient energy from the wind during their trajectories, their impacts with the ground can mobilize other sand and dust particles which are entrained into the flow. This mechanism rapidly increase the number of particles that are carried by the wind. The general scheme briefly described above is the basis of the blowing of sand and dust in arid regions.

The windblown sand process can be seen as a balance between two different mechanism, the erosion of material from the soil and the sedimentation of material due to gravitational force. The zones in which erosion prevails are considered as sources of material, while the sand is deposited in zones in which sedimentation prevails. When these two mechanisms are in equilibrium a steady flow of sand is established. In this situation particles that stop on the ground due to sedimentation are replaced by new particles that are entrained into the flow due to erosion. Aeolian processes are then responsible for shaping the surface forming typical bedforms as *dunes* and *ripples*, eroding rocks and creating then new soil particles (see Figure 1.1-(a)).

The smallest particles, also referred to as *dust*, once entrained into the flow are affected mainly by turbulence, which prevails on the sedimentation mechanism. The dust can be transported for hundreds of kilometers forming a *dust cycle* (see Figure 1.2) whose importance in the Earth system is becoming more and more evident (see J.F. Kok et al. 2012). Mineral dust aerosols impact on ecosystems because they are responsible for transporting nutrients that influence the ecosystem productivity. It can increase in areas where dust aerosols are deposited. For example the Amazon rainforest productivity is influenced by phosphorus deposition due to dust deposition. However, the soil productivity can be reduced in areas where dust forms, contributing to desertification. Dust aerosols influence also the hydrological cycle, for example dust particles play the role of condensation nuclei for cloud formation (see J.F. Kok et al. 2012).

But the importance of the windblown sand phenomenon is not limited solely to geomorphological or climatic aspects. Since most of these areas are populated, human infrastructures are often subject to wind-blown sand and must resist from damaging (see Figure 1.1-(b)). The engineering world has therefore paid a lot of attention to the phenomenon, in order to devise solutions to mitigate its effects.

Last, aeolian processes also occurs in other planets of the Solar System as Venus and Mars. The Mars atmosphere is often affected by dust storms while typical bedforms as dunes are present in both the planets (see J.F. Kok et al. 2012 for details). Studying images of this bedforms and how they change can help in identify the atmosphere behaviour of these planets, as well as their past history.

(a) (b)

Figure 1.1: a) Dune field in Badain Jaran Desert, China (from Sherman 2020); b) Road covered by sand, United Arab Emirates - Photo: Irenaeus Herok (from *Kingdom Of Sand: Photographer Captures Apocalyptic Aerial Photos Of Sand-Covered Roads In The United Arab Emirates* n.d.).

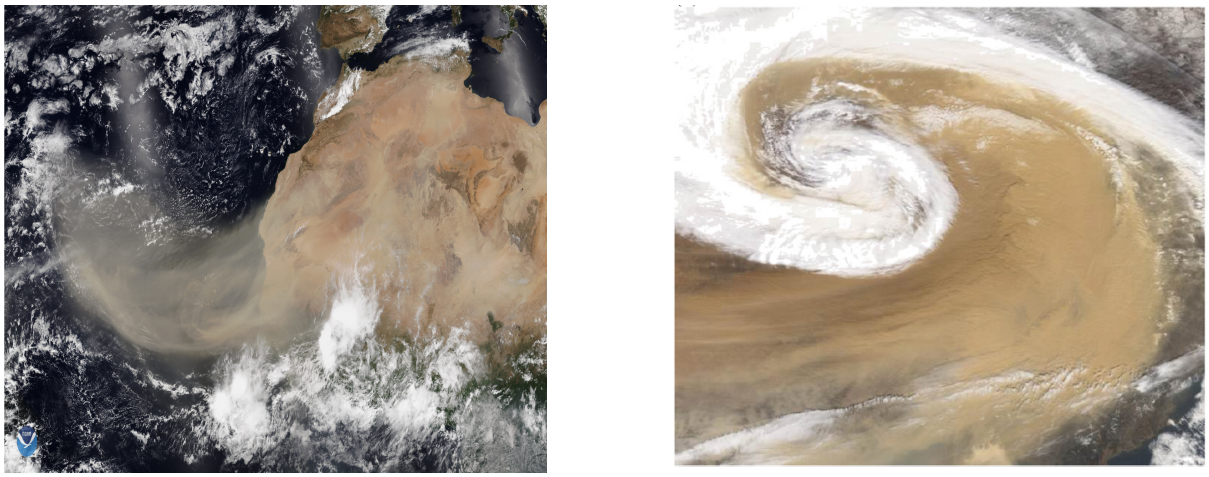

(a) (b)

Figure 1.2: a) Image of dust blowing off the Sahara Desert from the NOAA-20 satellite, June 2020 (from *National Oceanic and Atmospheric Administration* n.d.); b) Satellite image of the Mongolian dust Cyclone on 7 April 2001 taken by the MODIS (Moderate Resolution Imaging Spectroradiometer) on NASA's Aqua satellite (from J.F. Kok et al. 2012).

A deep understanding of the wind-blown sand process can lead to answers to some questions that are still unclear like what are the most appropriate tools to protect human infrastructure in arid zones and which is the influence on the Earth's climate.
Since climate change is leading to the desertification of many areas of the world (see for instance *World atlas of desertification* n.d., *The Great Green Wall* n.d.), the right answers must be found to address the problems of the future.

1.1 Computational Approaches

Computational simulations are an important tool for studying wind-blown sand phenomenon and the aspects described before. From a modelling point of view the phenomenon can be placed in

the framework of transport of particulate by wind, in which not only sand or dust but also snow, rainfall, hail and air pollutants are placed.
The main distinction that can be made in this class of problems is linked to the particulate dimension. Very small particles as dust or air pollutants particles are mainly affected by turbulence or viscosity effects so there are important differences in transport mechanisms. In this dissertation we do not consider these kind of problems.
The erosion and sedimentation of particles on the ground during the aeolian process determine the evolution of the ground. This leads to including the description of the phenomenon in the class of free-boundary value problems (Giudice, Nuca, et al. 2019).
The simulation techniques of wind-blown sand processes can be roughly divided into two groups according to how the sand is considered:

- *Eulerian approach*: the ensemble of particles is considered as a continuum that is dispersed in the air. Its behaviour is described by mass conservation and momentum balance equations (see Giudice and Preziosi 2020, Preziosi et al. 2015, Y. Zhang et al. 2020);

- *Lagrangian approach*: each particle is considered separately, solving the Newton equation for each of them and then computing its trajectory (see Z. Li et al. 2014, J. Kok et al. 2009, J. Kok et al. 2008, Huang et al. 2020, Sun et al. 2001).

The method adopted could depend on the characteristic problem dimension. Eulerian models are typically used for problems in which the characteristic dimension of the domain is many order of magnitude greater than the particle. In this case, the treatment of each particle could lead to high computational costs. Eulerian models are then used for example in studying the evolution of some bedforms as dunes, or the interaction of wind-blown sand with infrastructure (Preziosi et al. 2015, Giudice and Preziosi 2020). These models however need some bulk information, as the erosion capacity of wind, that must be obtained by experiments.
Lagrangian models indeed are typically used to study the fundamental physics of the process, because assumptions on the particles behaviour and their interaction can be easily introduced. This reduces the information needed to simulate the wind-blown sand process but also reduces the number of problems that can be addressed with this approach. As we said before the treatment of each particle could increase computational costs limiting the number of particles that can be considered.

Following the review article by Giudice, Nuca, et al. 2019 Lagrangian simulations can be classified according to the degree of coupling between wind-flow and sand particles:

- *1-way coupling*: particles passively follow the wind field, that is imposed or computed separately;

- *2-way coupling*: the presence of particles is taken into account in solving the wind flow, then there is a feedback of sand particles into the wind field (Huang et al. 2020, J. Kok et al. 2009);

- *4-way coupling*: interparticle interactions in the air are considered, as well as the particle feedback on the flow (Z. Li et al. 2014, Sun et al. 2001).

Lagrangian models also differ in the way in which the grain-bed interaction is simulated, that is an important feature of these models as we will see next. Some of these models use a Discrete Element Method (DEM) simulating the interaction between the incoming impact particle and the soil particles using contact models (Sun et al. 2001, Z. Li et al. 2014). Others use a stochastic approach sampling ejection information of particles from probability distributions obtained from experimental observations or theoretical models (J. Kok et al. 2009, Huang et al. 2020). The particle-bed interaction and the way in which it can be simulated will be discussed later.
Further computational simulations differ with respect to the way in which the wind flow is solved. Since the process is characterized by turbulent flows, *Reynolds Average Navier-Stokes equations* (RANS) (Giudice and Preziosi 2020, Preziosi et al. 2015) and *Large Eddy Simulation* (LES)

(Huang et al. 2020, Y. Zhang et al. 2020, Z. Li et al. 2014) are typically adopted.
In J. Kok et al. 2009 instead, Navier-Stokes equations are not solved but the flow is imposed as a known function, and it is considered as the sum of a mean wind velocity profile and fluctuations related to turbulence.

1.2 Sand Particles and Modes of Transport

Let us first focus on the particles that constitute the wind-blown sand process. The term *sand* refers generically to granular material composed by solid and inorganic particles that are formed by erosion of rocks. It is due to the action of atmospheric agents, the main ones being water and wind. The sand particles composition could vary because they derive from different rocks. The most common constituent for inland continental settings is silica, in the form of quarz (from Bagnold 1941). One of the aspects that makes modelling the sand transport complex is that sand particles have different shapes (see Figure 1.3). This is due to their different origins and to the transport process by wind, which causes the particles to fragment and take on irregular shapes. From a modelling point of view this leads to a complexity in describing particle-particle and particle-bed interactions.

The definition of sand depending on its dimension varies in the literature. J.F. Kok et al. 2012

Figure 1.3: Sand photomicrography from different areas in the world (from Stefan 2021): a) Australia – New South Wales – Sydney – Banks of Narrabean lake, b) United Arab Emirates – Dubai – Hatta Road, Appx. 57 km E of Dubai, c) South Africa – Western Cape – Cape Peninsula, Hout Bay, d) France – Corse-du-Sud (Corsica) – Corsica island, Marine d'Albo, Cap Corse (Ligurian Sea).

define sand as particles with diameter between 62.5 μm and 2000 μm while ISO 14688 2017 grades sand according to its particles diameter as fine (0.063 mm-0.2 mm), medium (0.2 mm-0.63 mm) and coarse (0.63 mm-2 mm). We point out that natural sand is typically a mix of particles with different diameters. Particles with diameter less than 63 μm are usually identified as dust, which is also defined as material that can be suspended by wind and that can be transported for kilometers as described before.
The transport of sand particles occurs in different modes that depend on the wind force and on the particle diameter. Once the wind has increased its velocity until grains start moving, the first particles that are lifted are the ones with small diameters. They start jumping over the

ground following the wind direction in a process called *saltation*. These particles, also reffered to as *saltators*, gain energy from the wind during their balistic-like trajectories making longer and longer jumps. When their energy is large enough they can mobilize other particles during their impacts. If the particle dimension is not too large then they become saltators, while larger particles settle back to the soil after short hops: this mode of motion is called *reptation*. If the particle inertia is large enough they can just roll or slide in a mode called *creep* (see Figure 1.4). Dust particles indeed are not mobilized by wind because their small dimensions make inter-particle forces large enough to keep them on the ground. Dust particles are typically ejected during impact events of bigger particles.
All these modes of motion depend on particle inertia and on the wind force, then typically each modes morphs into another according to the wind behaviour. Further, natural sand is composed by particles with different diameters, then all these modes are present in the sand transport process. This makes it more complex to model the process in its entirety, because each mode needs a different level of detail to be described. For example, describing *creep* or *reptation* modes involves considering the configuration of all particles on the ground, whereas this is not strictly necessary in the description of *saltation*.
Among all these different modes of sand transport during the aeolian process, saltation involves the 80% of the transported mass (Raffaele et al. 2016) so a lot of attention has been paid to this process by the engineering and geomorphologist community. We point out anyway that there is not a precise definition of each mode of transport, but typically particles that move in large ballistic hops with a maximum height h larger than the particle diameter d are referred to as *saltators* (Pahtz, Clark, et al. 2020).

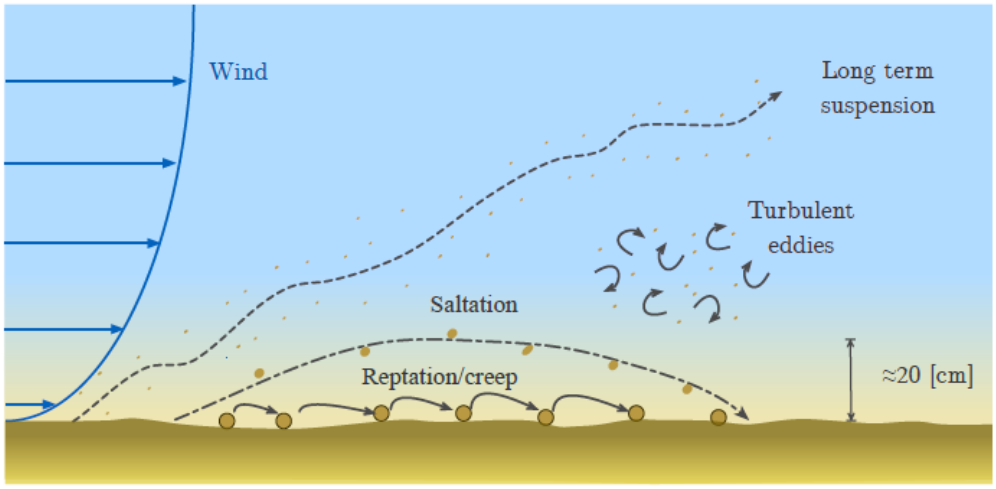

Figure 1.4: Different modes of motion for sand particles during the wind-blown sand process (from Giudice, Nuca, et al. 2019).

1.3 The Saltation Process

Let now summarise which are the main aspects of the saltation process. When wind force increases and the wind shear stress on the ground reaches a threshold value, particles are lifted and start hopping along the surface. Every time the lifted particle impacts on the ground it moves other particles, which initially have too little energy to start hopping for long distances so they settle down after a while. With each jump the lifted particle gain energy by the wind, until its impact on the ground eject new particles that have enough energy to continue the process. Then, the number of particles into the system starts growing fast.
Since during its trajectory every particles subtracts momentum from the wind, the wind slows down as the concentration of particles increases. This mechanism acts as a negative feedback by reducing particles energy and then the ejection of new particles during impacts as well as the

triggering of new particles by the wind.
These mechanisms operate until the steady-state saltation is reached. We can then roughly identify some physical aspects that together act to constitute the saltation process:

- the entrainment of particles by the wind;
- the trajectories of particles;
- the impact of particles on the ground;
- the ejection of new particles;
- the wind flow characteristics;
- the feedback of particles on the wind flow.

Each of these parts should be taken into account in the simulation of saltation process.

1.3.1 Entrainment of Particles by the Wind

As described above, the saltation process starts with a little number of particles that are lifted off the ground by wind. The mechanism of particles entrainment due to wind action is referred to as *fluid entrainment*. The value of shear stress at which particles start hopping is referred to as *fluid threshold* τ_{th}. This value is tyically expressed in Aeolian Research by the *shear velocity threshold* u^*_{th} which is obtained from τ_{th} by the definition of the shear velocity (1.1) (where ρ_a is the density of air):

$$u^* =: \sqrt{\frac{\tau}{\rho_a}} \tag{1.1}$$

The shear velocity threshold u^*_{th} represents an important parameter of the saltation process. It identifies in which condition the saltation process is triggered.
The fluid threshold depends on particle inertia. In Figure 1.5 experimental measurements of u^*_{th} with respect to particle *equivalent diameter* are shown. The equivalent diameter is defined as the diameter of a sphere of the same volume of the particle. As we can see, experimental results present a minimum, and for small diameter the value of u^*_{th} increases. As we have already mentioned, dust particles are ejected mainly by impact of bigger particles, due to the strength of the inter-particle forces for dust particles. Instead, the minimum of experimental data corresponds to diameter of the first particles to be entrained by the wind during the process. The dispersion of the data reflects the complexity in describing and measuring the shear velocity threshold. In Raffaele et al. 2016 authors identify two different approach in formulating a shear velocity threshold model.

i) The *deterministic approach* aims at identifying u^*_{th} on the basis of forces that are acting on the ground particle. These forces are the aerodynamical forces (lift and drag) that lead to the particle entrainment and the stabilizing forces that are the gravitational and inter-particle forces. This approach reveals the dependence of u^*_{th} on the particle diameter. Since not all this forces are known, as the inter-particle forces that could depend on different parameters (particles materials or ground moisture), semi-empirical models have been proposed with parameters that are fitted according to experimental data. One of the most used model was proposed by Bagnold in his pionieer studies:

$$u^*_{th} = A_B \sqrt{\frac{\rho_s - \rho_a}{\rho_a} g d} \tag{1.2}$$

where d is the equivalent particle diameter, ρ_s is the granular material density while the constant A_B encloses interparticle forces, lift forces and the Reynolds number of the flow - he obtained that $A_B = 0.10$ (Raffaele et al. 2016). His formula anyway does not identify the minimum of u^*_{th} with respect to diameters observed in experimental results (see Figure 1.5).

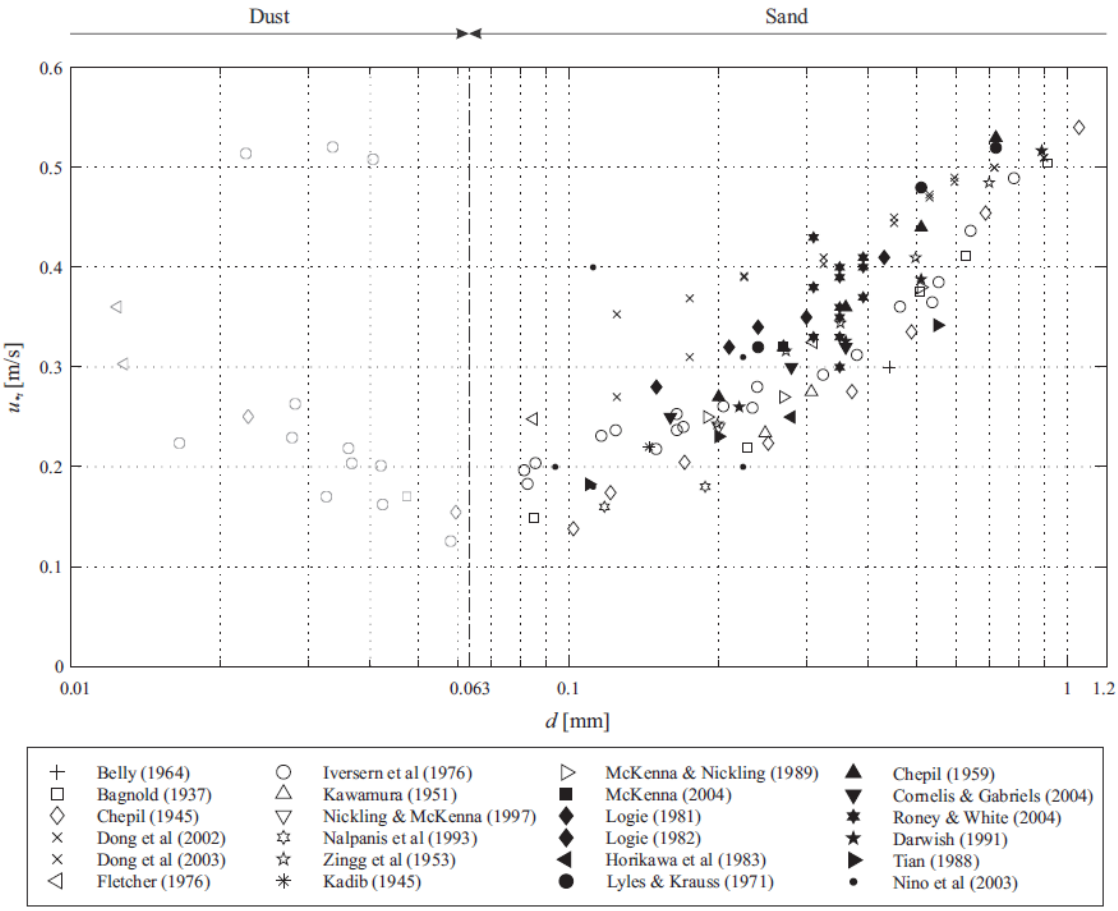

Figure 1.5: Experimental results for the shear velocity threshold u^*_{th} of wind associated to the initiation of motion. Data from different authors are reported. Experimental results show a minimum in the transition between sand and dust (from Raffaele et al. 2016).

Shao and Lu introduced a correction related to interparticle forces, that is represented by the dimensional parameter $\gamma\,[N/m]$:

$$u^*_{th} = A_S \sqrt{\frac{\rho_s - \rho_a}{\rho_a} g d + \frac{\gamma}{\rho_a d}} \tag{1.3}$$

They found that $A_S = 0.111$ and $\gamma = 2.9 \times 10^{-4}\, Nm^{-1}$. The recent work of Raffaele et al. 2016 refitted the formulas over a large dataset of experimental results from different authors founding new values for these parameters: $A_B = 0.127$, $A_S = 0.124$, $\gamma = 1.12 \times 10^{-4}\, Nm^{-1}$. We point out that in Raffaele et al. 2016 only results for sand particles are used, while data of dust particles are discarded. The relations (1.2) and (1.3) with refitted parameters are shown in Figure 1.6.

ii) The other approach that can be adopted in identifying the shear velocity threshold is a *probabilistic approach*. It is motivated by the variability in experimental data especially for small particles. Entrainment of particles by wind is a process affected by uncertainties related to the arrangement of particles on the ground, their material and size distribution, the ground conditions and the wind. In fact, particles can be lifted by turbulent flow eddies as described by Pahtz, Clark, et al. 2020. The process is then characterized by randomness due to the physics involved.
Probabilistic models try to relate u^*_{th} to random variables that represent inter-particle and aerodynamical forces, describing the shear velocity threshold itself as a random variable. This approach anyway has some modeling and technical difficulties as pointed out in Raffaele

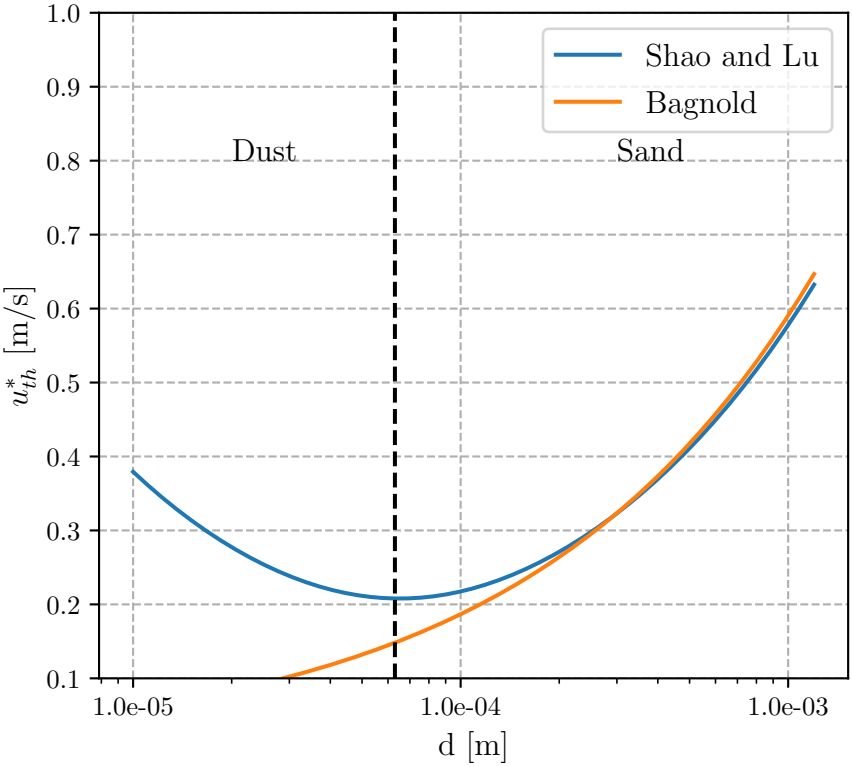

Figure 1.6: Relations (1.2) and (1.3) are shown. Particle diameter is represented on a logarithmic scale. The black dotted line identifies the division between sand particles (on the right) and dust particles (on the left).

et al. 2016, related to the difficulty in identifying all the random variables on which u^*_{th} depends and the difficulty in obtaining their probability distribution from measurements. For this reason formulas (1.2) and (1.3) obtained by a deterministic approach remain the most popular relations for the shear velocity threshold because of its simplicity and a good agreement with wind tunnel experimental results.

Despite the uncertainties related to the randomness of the process, the determination of u^*_{th} is also affected by some *epistemic uncertainties* as referred by Raffaele et al. 2016. Results obtained in wind tunnel are affected by measurement uncertainties due to errors and to the different techniques or procedures adopted. Further, there is no consensus in the aeolian community in a quantitative definition of the shear velocity threshold (as pointed out in Sherman 2020). Typically it is identified by qualitative description as the threshold at which some particles start hopping for long period. Experimental results presented by different authors are clearly affected by the lack of a unified definition of u^*_{th}.
A critical discussion on the shear velocity threshold associated to the sediment transport initiation can be found in Pahtz, Clark, et al. 2020. Authors identify different fluid thresholds that can be associated to the sediment transport. The exact definition of the shear velocity threshold then is still debated.

Once the saltation process reaches its steady state, also the role of fluid entrainment of particles remains unclear. Some studies (Pahtz and Durán 2016, Pahtz, Clark, et al. 2020, J.F. Kok et al. 2012) point out the important role of entrainment of particles due to impacts, also called *impact entrainment*, in sustaining the saltation process while some authors (J. Kok et al. 2009) consider that in steady state fluid entrainment rarely occurs.
Supporting this, Bagnold 1941 identifies a different shear velocity threshold with respect to u^*_{th}

that characterises the process, the *impact threshold* u^*_{imp}. It corresponds to the minimum value of shear velocity that sustains saltation. In fact, when the process starts impacts seem to be more efficient in transferring momentum to the ground particles with respect to the wind flow. Then the process can be sustained by a value of u^* less than the fluid threshold. This has been justified by the idea that in the steady state, flow has just to compensate the energy lost by particles during their impacts (Pahtz, Clark, et al. 2020). In applications u^*_{imp} is typically considered as the 80% of the fluid threshold (Raffaele et al. 2016).
As we pointed out before saltating particles affect the wind flow and then also the fluid entrainment. The particle feedback on the flow will be discussed later. Both fluid and impact entrainment could play an important role in the triggering of ground particles. However the exact mechanism of particles entrainments in steady state during the saltation process is still debated (Pahtz, Clark, et al. 2020).

1.3.2 The Drag Force Model

Once a particle is entrained it undergoes a ballistic-like trajectory, determined by aerodynamic and gravitational forces. Aerodynamics acts on the particle mainly through the drag force, that transfers momentum to the particle accelerating it and is expressed by:

$$\mathcal{F}_{Drag} = \frac{\pi d^2}{8}\rho_a C_D \|\vec{u}_f - \vec{u}_p\| \, (\vec{u}_f - \vec{u}_p) \tag{1.4}$$

where $\vec{u}_p$, $\vec{u}_f$ are respectively the particle and wind velocity, and d is the *equivalent diameter* of the particle. The coefficient C_D is the *drag coefficient*. For spherical particles the drag coefficient depends on the Reynolds number, that in case of a flow over a particle is called *particle Reynolds number* Re_p:

$$Re_p = \frac{\|\vec{u}_p - \vec{u}_f\| d}{\nu_a} \tag{1.5}$$

where ν_a is the cinematic viscosity of the fluid. The flow at $Re_p \ll 1$ is also called *Stokes' flow*. In this situation viscous terms prevail on the inertial terms, the drag coefficient can be analytically obtained and it corresponds to *Stokes' relation*:

$$C_D(Re_p) = \frac{24}{Re_p}$$

As Re_p increase the flow separates (at $Re_p \approx 20$) and a wake forms, then the drag coefficient starts decreasing. For values $1000 < Re_p < 3\times10^5$ vortex shedding starts and turbulence develops in the wake of the particle, while the boundary layer remains laminar: this is called *Newton's regime*. In Newton's regime the drag coefficient is almost constant. When $Re_p > 3 \times 10^5$ turbulence develops in the boundary layer and C_D decreases significantly (this threshold value is also called *critical Reynolds number*). A scheme of C_D with respect to particle Reynolds number is shown in Figure 1.7. One of most accurate relation for C_D respect to Reynolds number is the relation (1.6) obtained by Cliff and Gauin (from Bagheri et al. 2016).

$$C_D(Re_p) = \frac{24}{Re_p}(1 + 0.15\, Re_p^{0.687}) + \frac{0.42}{1 + \dfrac{42500}{Re_p^{1.16}}} \quad \text{for} \quad Re_p < 3 \cdot 10^5 \tag{1.6}$$

In general, the drag coefficient for natural sand is larger than for spherical particles. In fact, the irregular shape that characterises sand particles increases the surface area, while surface roughness triggers flow separations. Different relations of C_D for non-spherical particles have been proposed. Typically some shape descriptors, that are functions of geometric features of the particle, are introduced in these relations in order to identify the main characteristics that influence C_D. Bagheri et al. 2016 performed a large number of experiments with different shapes

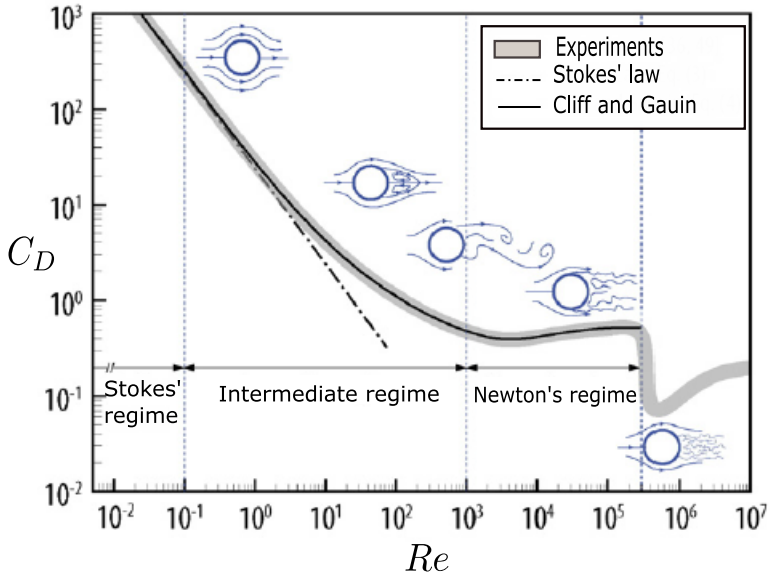

Figure 1.7: Drag coefficient of a sphere respect to the Reynolds number. The Stokes' law, the relation (1.6) and experimental data are shown (from Bagheri et al. 2016).

and diameter. They identify the following relation:

$$\frac{C_D}{k_N} = \frac{24\,k_S}{Re\,k_N}\left(1 + 0.125\left(Re\frac{k_N}{k_S}\right)^{\frac{2}{3}}\right) + \frac{0.46}{1 + \dfrac{5330}{Re\dfrac{k_N}{k_S}}} \tag{1.7}$$

where k_S and k_N are called respectively *Stokes'* and *Newton's drag corrections*. They are functions of shape descriptors identified by the authors. In Figure 1.8 results obtained in Bagheri et al. 2016 and from other authors, and the relation (1.7) are shown.

In addition to drag, other aerodynamical forces play a role in defining the particle trajectory, for example the *Magnus force* that is a lift force due to particle rotation. Further, some authors argued that during the saltation process the effect of electrostatic forces could increase particles concentration and then affect the particle behaviour. It is commonly believed that these forces play a secondary role in the particle trajectory, but further research has to highlight their importance in the saltation process.

The effect of turbulence on particle trajectories is still debated. J. Kok et al. 2009 found that the effect of turbulence increases as decreasing the particle diameter and affects the trajectory of particles with diameter $d \sim 200\,\mu m$. Anyway the characteristics of turbulence during saltation remain uncertain, as weel as its effect on particles trajectories.

The last aspect that can affect particles trajectories is the mid-air collision with other particles. The probability that a saltator impacts with another particle during its trajectory depends on particles concentration, so it is greater near the ground where concentration is bigger. Particles that have just been entrained could then perform a collision with another particle and return to the ground. However, once the particle is making a hop the probability of colliding with another saltator decreases. Further research has to establish the role of mid-air collisions in saltation, then some of numerical models do not consider them because of the increasing in modelling assumptions and computational cost (for istance in J. Kok et al. 2009).

1.3.3 The Impact of Particles on the Ground

Every saltating particle at the end of its trajectory impacts on the ground. The particle may rebound with less energy than the impact energy or it may stop. If it rebounds the collision converts part of the horizontal momentum into vertical momentum. In fact, the rebounding angle

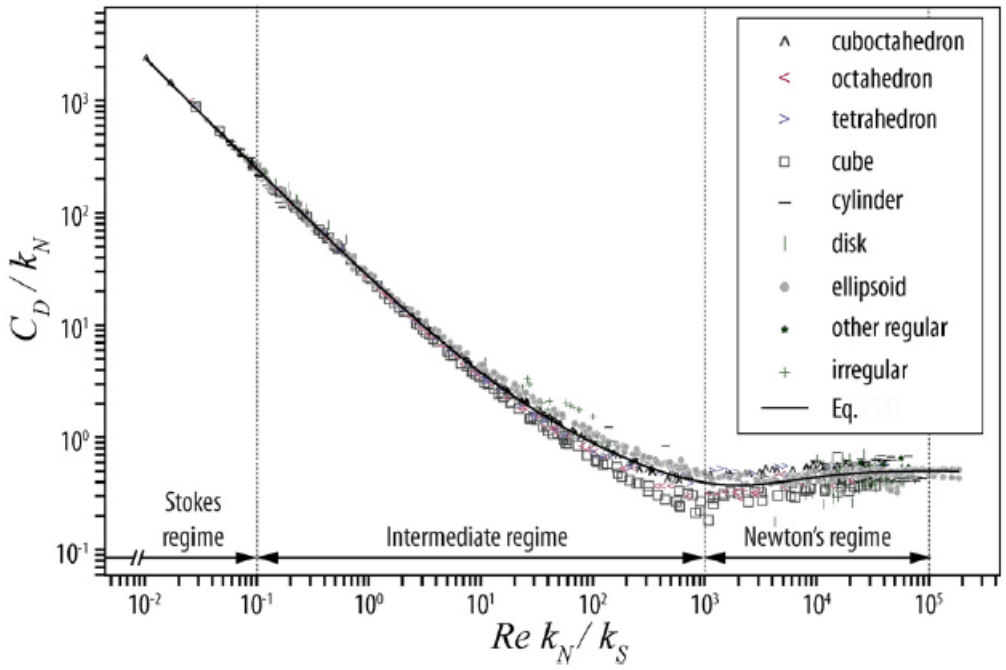

Figure 1.8: Different experimental data for non-spherical particles are shown. The equation (1.7) is also reported (from Bagheri et al. 2016).

is usually greater than the impact angle (both considered with respect to the horizontal direction). This conversion is a critical factor of the saltation process, because it returns part of the vertical momentum dissipated by the fluid drag. This allows the particle to reach heights where it can gain enough energy from the wind to continue the process. The probability of rebound and the fraction of energy retained by the impact particle is considered as foundamental parameters of the process (J.F. Kok et al. 2012).
In addition, the impact can eject new particles (i.e the *impact entrainment*), increasing the number of particles into the system. These particles are usually characterized by a speed lower than the one of the rebound particle. Most of them have too little energy and stop after a hop, while some of them gain enough energy to start hopping for longer periods, becoming *saltators* and continuing the process.

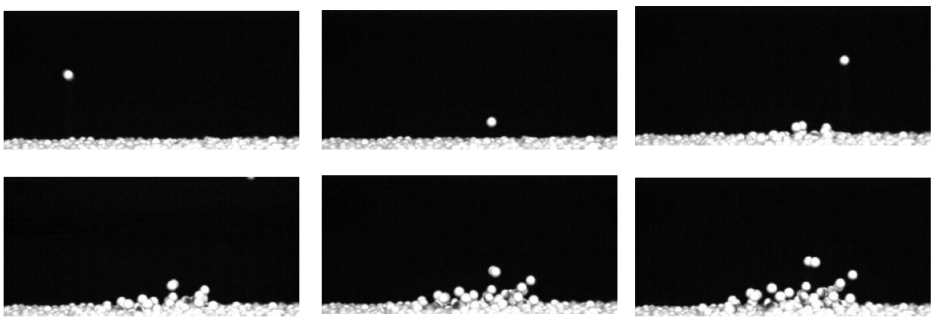

Figure 1.9: The figure shows the impact of a spherical particle on a spherical particles packing. Images are in temporal sequence, from left to right, from top to bottom (from Beladjine et al. 2007).

The impact of a sand particles on the ground is a local phenomenon, which depends on the local conditions of steady ground grains involved into the incoming impact event as well as the impact particle. The grain-bed interaction is a strongly stochastic mechanism. As described above, particle shape is varied and irregular (see Figure 1.3) and the arrangement of particles on

the ground is random, then it is not known a priori what the impact geometry is. In addition, sand composition can also be stochastic because its origin from different rocks as well as other conditions that can affect impact such as the local soil moisture.
Experiments (D. Wang et al. 2008, Beladjine et al. 2007, W. Zhang, Kang, et al. 2007, Xiao et al. 2017, LiQiang Kang et al. 2008, You-Xing et al. 2019) have been performed in order to obtain the probability distributions of characteristics of rebounding and ejected particles. This information are mainly the rebound velocity, the number of ejected particles and their velocities. The experiments can be roughly divided into two different groups.

i) The first is composed by experiments performed in wind tunnel (D. Wang et al. 2008, W. Zhang, Kang, et al. 2007, Xiao et al. 2017, LiQiang Kang et al. 2008). In this case particles velocities are measured while the saltation process acts: a turbulent flow is increased until sand particles start moving. Measurements are made in the steady state in order to make a statistical analysis of these quantities. These experiments, however, are not able to fully clarify the link between input conditions of impact and its outputs. They are performed in order to obtain information during the saltation process.

ii) The other group consists in *impact experiments* (Beladjine et al. 2007, You-Xing et al. 2019), in which a single particle is shot against the ground which is composed by static and packed particles. Velocity and angle of impact are changed to get statistics on the rebound velocity as well as statistics on the number of ejected particles and their velocities. The aim of these experiments is to characterize the probability distribution of the output conditions based on the input conditions.
The fundamental idea that is used to justify impact experiments is that the characteristic time of the impact process is less than the typical time scale of aerodynamic processes (as argued by Beladjine et al. 2007). So, impact experiments can be used to study impact events also during the saltation process. However, as pointed out in Pahtz, Clark, et al. 2020 in the saltation process, for a large frequency of impacts and for large impact energies the bed may not treated as static because particles could impact on particles that are rolling on the bed. This could affect the impact event, but to the best of our knowledge this is still an open problem. Further, some of these impact experiments are made not with natural sand as in You-Xing et al. 2019 but with identical spherical particles of a certain material (as in Beladjine et al. 2007). The obtained results could be affected by the lack of detail that characterizes natural sand.

Experiments typically use photographic method or laser Doppler method, which are two major methods to measure particle velocities (Xiao et al. 2017). The former consists in image processing. This method has the advantage of displaying the impact and it can measure particles velocities within a target area. However, it is difficult to obtain measurements if the particle concentration is too high as at very low heights in wind tunnel experiments. The laser Doppler method instead uses the Doppler effect to obtain particles velocities. It can measure velocity in a fixed point but it does not track particles.

We report the results obtained by You-Xing et al. 2019 that perform an impact experiment as defined above, in which natural sand is used. Results are obtained by a high-speed camera, and 1024 impact events are used. Results for the rebound angle θ_r and rebound velocity V_r, and for ejection angle θ_{ej} and velocity V_{ej} as well as the number of ejected particles n are collected (see Figure 1.10 for the definition of these quantities). We point out that particles are considered as ejected if they reach a height larger than one diameter. Events are divided into 9 groups, according to the impact velocity V_i and impact angle θ_i (as defined in Figure 1.10).
In order to obtain a number of samplings large enough for statistics, the nine groups are different according to the measured quantity. Figure 1.11 reports information of the groups for the rebound angle θ_r, the *restitution coefficient* e defined as the ratio between the rebound velocity V_r and the impact velocity V_i, and the number of ejected particles n (in which the rebound particle is not considered). Figure 1.12 aims at describing the angle θ_{ej} and velocity V_{ej} of ejection.

From the analysis of data collected by experiments, the authors identify the probability distributions of the output quantities of impact. Probability distributions parameters depend on the impact information V_i and θ_i.

- Angle of rebound θ_r:

$$f(\theta_r) = \frac{1}{\sqrt{2\pi}\sigma\theta_r} \exp\left(-\frac{(\ln\theta_r - \mu)^2}{2\sigma^2}\right) \qquad \begin{aligned} \mu &= 2.92 - 0.034V_i + 0.02\theta_i \\ \sigma &= 0.9 - 0.049V_i \end{aligned} \tag{1.8}$$

- Restitution coefficient e:

$$f(e) = \frac{1}{\sqrt{2\pi}\sigma} \exp\left(-\frac{(e - \mu)^2}{2\sigma^2}\right) \qquad \begin{aligned} \mu &= 0.62 + 0.0084V_i - 0.63\sin\theta_i \\ \sigma &= 0.19 - 0.0035V_i - 2.96 \cdot 10^{-5}\theta_1^2 \end{aligned} \tag{1.9}$$

- Number of ejected particles n:

$$f(n) = \frac{1}{\sqrt{2\pi}\sigma\, n} \exp\left(-\frac{(\ln n - \mu)^2}{2\sigma^2}\right) \qquad \begin{aligned} \mu &= -0.3 + 1.35\ln V_i - 0.01\theta_i \\ \sigma &= 0.55 \end{aligned} \tag{1.10}$$

- Angle of ejection θ_{ej}:

$$f(\theta_{ej}) = \frac{1}{\sqrt{2\pi}\sigma\theta_{ej}} \exp\left(-\frac{(\ln\theta_{ej} - \mu)^2}{2\sigma^2}\right) \qquad \begin{aligned} \mu &= 3.94 \\ \sigma &= 0.64 \end{aligned} \tag{1.11}$$

- Velocity of ejection V_{ej}:

$$f(V_{ej}) = \frac{1}{\sqrt{2\pi}\sigma\, V_{ej}} \exp\left(-\frac{(\ln V_{ej} - \mu)^2}{2\sigma^2}\right) \qquad \begin{aligned} \mu &= -1.67 + 0.082V_i - 0.003\theta_i \\ \sigma &= 0.616\, m^2/s^2 \end{aligned} \tag{1.12}$$

Experimental results and the theoretical probability distributions found are reported in Figure 1.11-(b),(c),(d) and in Figure 1.12-(b),(c).

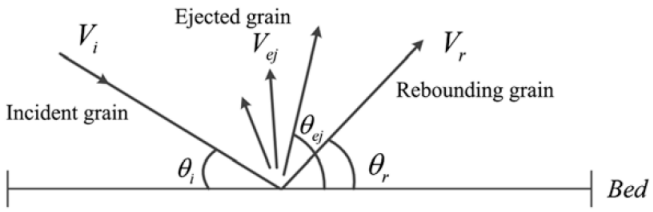

Figure 1.10: Scheme of grain-bed impact. The characteristic quantities of impact are shown: impact velocity V_i, impact angle θ_i, rebound velocity V_r, rebound angle θ_r, ejection velocity V_{ej}, ejection angle θ_{ej} (from You-Xing et al. 2019).

As we can see in Figures 1.11 and in 1.12 it is found that the rebound angle, the number of liftoff particles, the ejection velocity and angle follow a lognormal distribution, while the restitution coefficient follows a normal distribution. Further, the ejection velocity and angle are less dependent from impact velocity and angle than other quantities. The mean number of liftoff particles increase with the impact velocity.

Numerical simulations performed by Yin et al. 2021 are designed to reproduce the impact experiments described above. They use a Discrete Element Method (DEM) to simulate the impact of a single particle on a random arrangement of ground particles. This method simulate spherical particles with a specific inter-particle contact force model. Numerical experiments have the advantage of being able to easily modify some aspects of the process. For example, introducing a

Group no.	V_i (m/s)		θ_i (°)	
	Mean	Standard deviation	Mean	Standard deviation
1	3.2	0.4	23.2	2.0
2	4.1	0.2	21.8	2.6
3	5.4	0.7	21.9	2.5
4	2.6	0.4	30.7	3.4
5	3.7	0.3	30.6	4.8
6	5.4	0.8	37.6	4.9
7	4.0	0.4	47.1	2.9
8	5.0	0.2	46.6	2.1
9	6.2	0.5	46.0	1.8

(a)

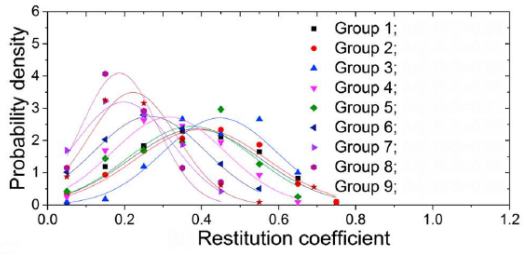

(b)

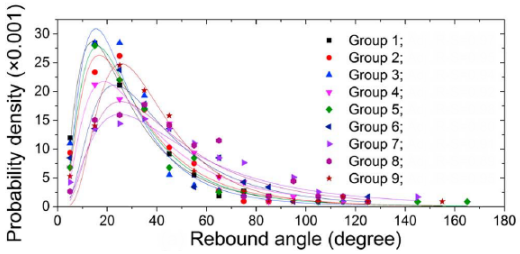

(c)

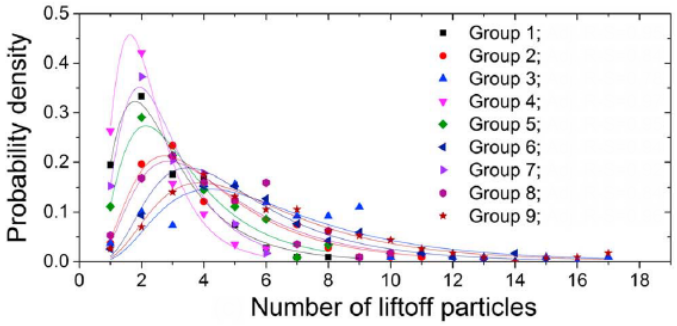

(d)

Figure 1.11: Results of an impact experiment with natural sand, from You-Xing et al. 2019. In (a) are identified the impact information of the nine groups of impact events considered in the data analysis. The statistics of the following quantities are reported: (b) restitution coefficient, defined as V_r/V_i; (c) rebound angle; (d) number of liftoff particles.

random distribution over the diameter of particles in order to reproduce natural sand conditions or introducing a bed slope as in Yin et al. 2021. Numerical experiments also allow to modify some parameters related to the contact between the two particles, as the elastic constants of the particle material. Anyway, an important feature of the process involving the natural sand, that is the random particle shape, is overlooked because of computational costs. Then, numerical results can be affected by the lack of this important aspect.

We have already pointed out that some authors consider the impact entrainment of particles as the main source of particles during the saltation process (Pahtz and Durán 2016, Pahtz, Clark, et al. 2020, J.F. Kok et al. 2012). Despite its key role on describing the saltation process, the impact dynamics is still poorly understood due to the great number of variables involved. A systematic study on a large amount of data for natural sand could help to clarify the fundamental physics of grain-bed interaction.
Due to its importance, a numerical model of the saltation process has to take account of the grain-bed impact mechanisms. Due to its random nature, a stochastic description of the impact entrainment is typically adopted (J. Kok et al. 2009, Z. Li et al. 2014, Andreotti 2004, Huang

Group No.	V_i (m/s)		θ_i (°)	
	Mean	Standard deviation	Mean	Standard deviation
1	3.5	0.4	22.7	2.2
2	4.5	0.3	21.6	2.7
3	5.8	0.6	21.2	2.3
4	3.2	0.5	30.3	4.2
5	4.6	0.4	35.2	6.4
6	6.0	0.7	38.7	4.6
7	4.4	0.5	47.5	2.7
8	5.5	0.2	46.2	2.2
9	6.6	0.6	46.3	2.1

(a)

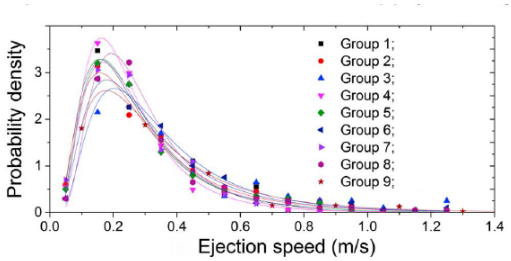

(b)

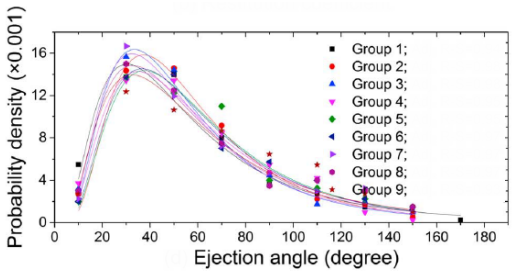

(c)

Figure 1.12: Results of an impact experiment with natural sand, from You-Xing et al. 2019. In (a) are identified the impact information of the nine groups of impact events considered in the data analysis. The statistics of the following quantities are reported: (b) velocity of ejection; (c) angle of ejection.

et al. 2020). The grain-bed impact event in numerical models of saltation can be achieved in two ways.

i) The first consists in simulating an interaction between the impacting particle and a soil particle defining the contact forces. It corresponds to a DEM approach. In order to maintain the stochastic nature of the process, Z. Li et al. 2014 simulate a random arrangement of particles on the ground during the impact process. Anyway, this approach leads to the simulation of spherical particles due to computational costs, not taking into account the characteristic random shape of sand particles.

ii) The other method consists in defining the so-called *splash functions* which link the characteristics of impact (as the velocity and angle of the incoming impact particle) to the characteristics of the ejected particles (both the rebounding particle and the new ejected particles). The splash functions are usually expressed by probability distributions for angles and velocities of the rebound and the new ejected particles, as well as their number. Splash functions can be identified by the impact experiments we presented before (as done in Huang et al. 2020) or it can be implicitly expressed by defining an *impact model* that simulate the impact dynamics. Impact models are typically based on some basic principles as the momentum and/or energy balance (see J. Kok et al. 2009, Crassous et al. 2007, Valance et al. 2009).

1.3.4 The Wind Flow and the Particles Feedback

The flow in the atmospheric boundary layer in which saltation occurs is turbulent. Typically the logarithmic *law of the wall* (1.13) is considered in simulations of the saltation process:

$$U_x(z) = \frac{u^*}{k} \ln\left(\frac{z + z_0}{z_0}\right) \tag{1.13}$$

where $U_x(z)$ is the mean horizontal fluid velocity at height z, u^* is the shear velocity (see (1.1)) related to the wind shear stress τ, z_0 is the *aerodynamic surface roughness* and k is the *von Kármán's constant* (that is $k \approx 0.40$). Equation (1.13) has been derived for flat and homogeneous surfaces assuming that the shear stress in surface layer is constant with height. This could be unrealistic for other conditions as non-uniform roughness of the surface. Further, the equation should be valid only for a neutral atmospheric condition otherwise corrections are needed. However these corrections are small near the surface where saltation takes place, and could be ignored. So, equation (1.13) is still considered sufficient in most of saltation studies (J.F. Kok et al. 2012). The aerodynamic surface roughness z_0 is related to the rougness of the surface. From an aerodynamic point of view the roughness is related to the presence of a viscous sublayer in which viscous forces prevail over inertial forces. For a smooth surface the thickness δ_{vis} of this sublayer is approximately

$$\delta_{vis} \approx \frac{5\nu_a}{u^*}$$

(see J.F. Kok et al. 2012). Elements present in the viscous sublayer can enchance turbulence, destroying the viscous sublayer. The roughness of the surface is expressed by the *roughness Reynolds number*:

$$Re_r = \frac{k_s u^*}{\nu_a} \tag{1.14}$$

where k_s is called *Nikuradse roughness* and it depends on the dimension of the surface elements. For an irregular surface of natural sand is $k_s \sim 2 \div 5\,D$ with D is the mean particle size. If $Re_r > 60$ the surface is termed *aerodynamically rough* because the viscous sublayer is destroyed and we have that

$$z_0 = \frac{k_s}{30} \tag{1.15}$$

while if $Re_r < 4$ the surface is termed *aerodynamically smooth*, the viscous sublayer is almost unperturbed and

$$z_0 = \frac{\nu_a}{9u^*} \tag{1.16}$$

Saltation process in Earth takes place in a transition regime between these two cases. So most studies used (1.15) because the transition regime does not differ too much from the rough regime (J.F. Kok et al. 2012).

J.F. Kok et al. 2012 suggest that the feedback of particles on the flow is responsible for limiting the number particles during the saltation process. In fact, once the saltation process starts there is an extraction of wind momentum by the saltating particles. As pointed out by authors the Equation (1.13) should be then modified for the layer in which saltation take place, the so-called *saltation layer*, in general decreasing the wind speed.
Experimental measurements suggest that if u^* increases during the saltation process, the wind speed increases above the saltation layer while it decreases in the saltation layer. This effect leads wind speed profiles to intersect in a point at a height of $\sim 1\,cm$ above the surface. This feature is called *Bagnold focus*. The effect of saltating particles then acts as a roughness: the wind velocity profile is modified within the saltation layer and the aerodynamic roughness length for the flow above the saltation layer is increased (see Figure 1.13).
The presence of saltating particles also influence turbulence. It has been observed that particles increase the turbulence of the flow, in particular the magnitude of burst-sweep events is increased probably due to particle wakes (see B. Li et al. 2012 and Figure 1.14). However, the effect of saltating particles on the flow is still debated and needs to be clarified.

As dalready mentioned, in numerical simulations of saltation process the wind flow is typically solved by the use of RANS or LES, or by the description of the mean flow and pointwise fluctuations. If it is considered, the effect of saltating particles on the wind flow in simulations depends on the flow description. It can be expressed by the addition of a term into the Navier-Stokes equations (as in Z. Li et al. 2014 and Huang et al. 2020) or by the modification of the mean wind velocity profile as in J. Kok et al. 2009.

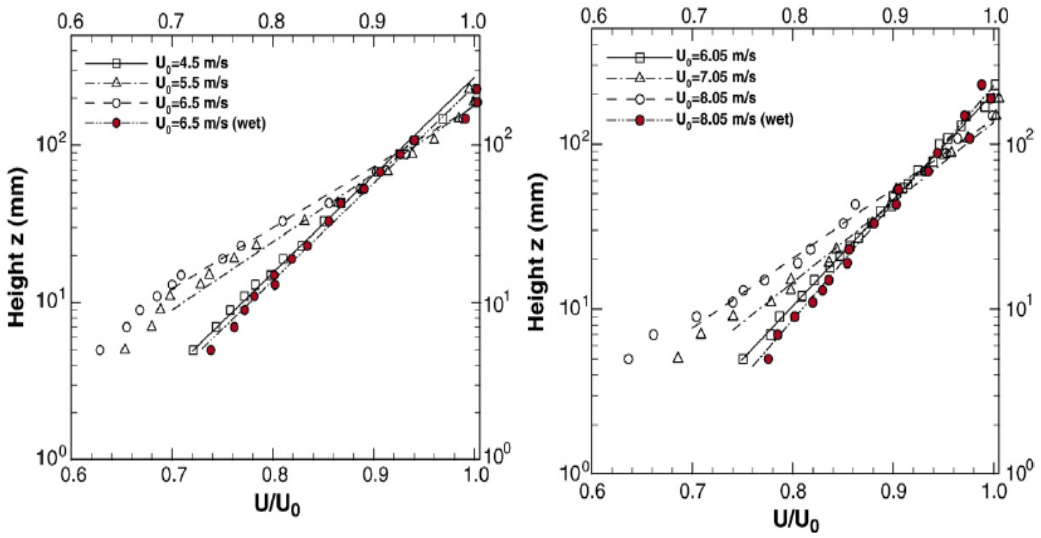

Figure 1.13: Results of wind tunnel experiments form W. Zhang, Y. Wang, et al. 2007. The figure shows the ratio between the mean wind velocity profile measured during the steady state of saltation and the free streem velocity profile. Results for different values of free streem velocities are reported (their values are shown in the figure).

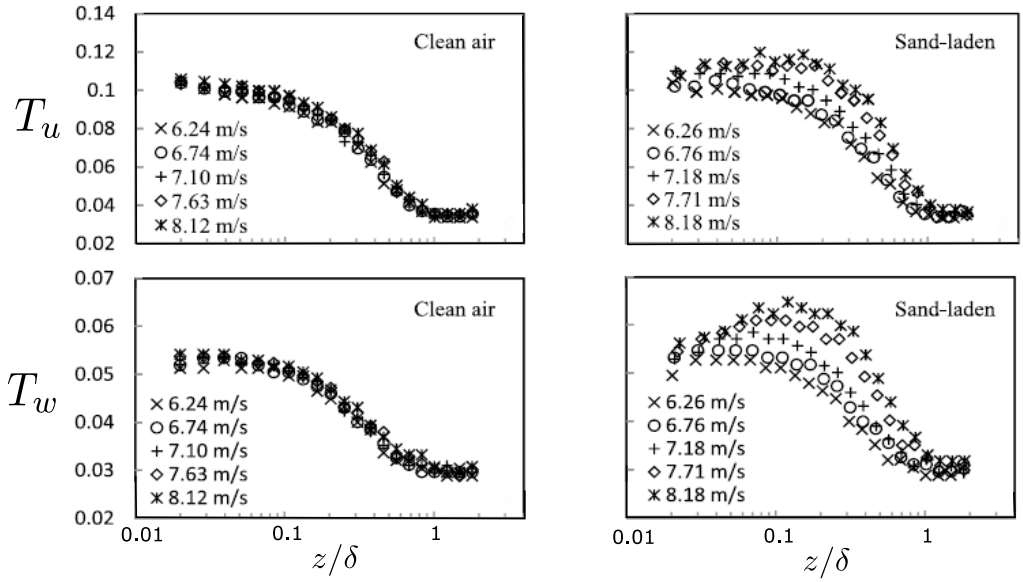

Figure 1.14: Experimental results obtained from B. Li et al. 2012. The figure shows the turbulence intensities T_u and T_w respectively defined as the ratio between horizontal and vertical velocity fluctuations with respect to the free streem velocity U_∞. Results for different free streem velocities are reported (their values are shown in the figure). In the horizontal axis, the ratio between height of measurement and the boundary layer depth $\delta =: 0.15\,m$.

1.3.5 Steady State of the Saltation Process

The several mechanisms presented before all together allow the saltation process to reach a steady state. A qualitative idea of what characterises the steady state of saltation is provided in J.F. Kok et al. 2012. Authors pointed out that in steady state one particle is input into the system (for impact or fluid entrainment) for each particle that is lost due to impacts.
The distance that is required by the process to reach the steady state is called *saturation length*. It depends on different length scales involved in saltation, as the typicall length of particle jumps, the lenght needed by the flow to accelerate particles and the length needed by the particles to modify the wind speed profile. Since the saturation length encloses all the processes involved

in saltation and the complexities associated with, there is a large range in measurements of the saturation length, from $\sim 1\,m$ to $\sim 10 - 20\,m$ (J.F. Kok et al. 2012).
The steady state is identified by quantities that remain approximately constant in time and distance. Since the system is characterized by turbulence, fluctuations of these quantities are still observed. The steady state is typically observed in wind tunnel experiments. However Sherman 2020 suggest that in field measurement these quantities could not reach a steady state due to the presence of large turbulent structures that are not replicable in wind tunnel experiments.
Two of the main quantities measured during wind tunnel experiments are the volumetric particle concentration with respect to the ground distance (see Figure 1.15-(a)) and the *horizontal mass flux* $q(z)$ ($[g\,cm^{-2}\,s^{-1}]$) which expresses the quantity of sand that flows per unit time and unit area at height z (see Figure 1.15-(b)). The horizontal mass flux is typically decreasing with the height, as well as the particles concentration, because the presence of particles in the wind flow decreases with height. Vertical integration of $q(z)$ gives the total mass flux Q of sand during the saltation process, which is an importat information for applications. In fact, it measures the rate of sand transport. The height of the saltation layer is typically defined by the mass flux as the height at which the 50% of the total mass flux occurs (J.F. Kok et al. 2012).

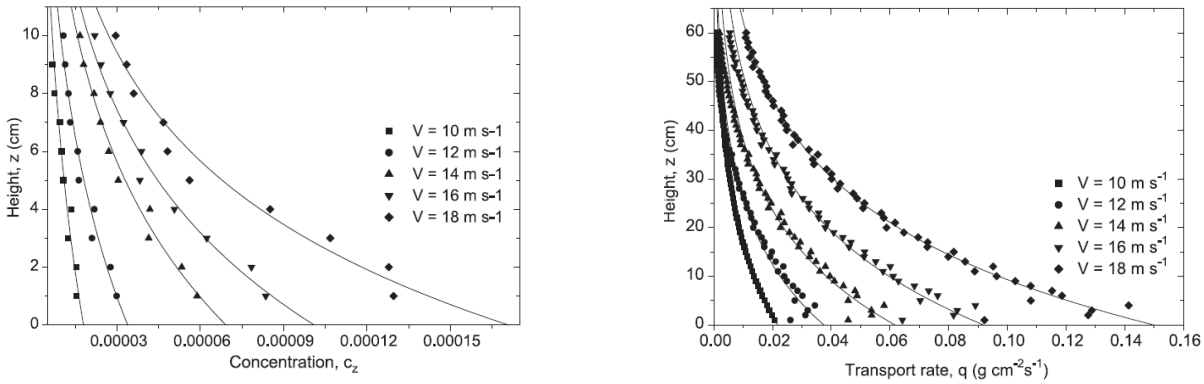

(a) (b)

Figure 1.15: Results of wind tunnel experiments. The following quantities are reported: (a) particles concentration, (b) horizontal mass flux with respect to height from the ground. Results are reported for different free stream wind velocities (the values are shown in the figure), while the sand particle diameters are in $[0.5,0.6]\,mm$ (from Liu et al. 2004).

Chapter 2

Particles Trajectories

Every saltating particles follows a trajectory mainly affected by gravitational and aerodynamical forces. The specific trajectory and the energy gain determine a connection between ejection velocity and impact velocity. The impact model instead establishes the link between impact velocity and ejection velocity of particles (as will be discussed in Chapter 4). The way in which these two aspects are linked contributes to the regulation of saltation phenomenon. In this chapter a single trajectory is computed from particle emission to its impact. Trajectory is solved for different initial conditions and parameters that influence it. Different information about particle trajectories are collected in order to build a *trajectory database*. They specify particle behaviour in the wind flow according to initial conditions, particle characteristic (i.e. particle diameter) and wind flow conditions. Turbulence fluctuations are neglected so that trajectory database corresponds to mean behaviour of particles. For the whole chapter we consider particles in a flat sand bed with a unidirectional wind in the x direction (see Figure 2.1).

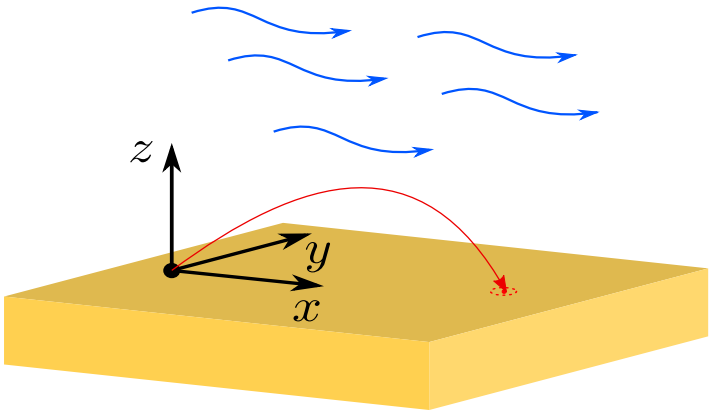

Figure 2.1: Scheme of a single trajectory on a flat sand bed.

2.1 Trajectory Equation

As described in Chapter 1 a particle ballistic trajectory is mainly determined by gravitational and aerodynamic forces, while the role of other forces is still debated. We consider the drag as the main aerodynamic force that acts on particles, as suggested in the literature (see J.F. Kok et al. 2012). So, we neglect other aerodynamic forces as well as the effect of electrostatic forces. Further, we do not consider the rotational dynamics of particles. Under these assumptions the

equation of motion writes:

$$m\frac{d^2\vec{x}}{dt^2} = \frac{\pi d^2}{8}\rho_a C_D(Re_p)\left\|\vec{u}_f(\vec{x}) - \frac{d\vec{x}}{dt}\right\|\left(\vec{u}_f(\vec{x}) - \frac{d\vec{x}}{dt}\right) - mg\vec{e}_z \tag{2.1}$$

where $\vec{u}_f$ is the wind velocity, ρ_a and ρ_s are respectively the fluid and granular material density and d is the *equivalent diameter* of particle. The particle mass m is computed from the particle diameter d by:

$$m = \rho_s\frac{\pi}{6}d^3 \tag{2.2}$$

The drag coefficient C_D is computed using Eq. (1.6).
We neglect turbulence fluctuations in order to study the mean behaviour of particles during their trajectories. The logarithmic profile for the mean wind velocity is imposed (see Eq. (1.13)). As previously mentioned, Eq. (2.1) is solved by changing initial conditions and parameters influencing it:

i) The homogeneity of the soil and wind flow makes the starting positions of particles irrelevant with respect to x and y coordinates. Initial positions of particles are set equal to the origin of axis.

ii) Initial particles velocities are expressed by the ejection kinetic energy e_1 and the ejection direction. This direction is identified by angles θ_1 and φ_1 with respect to vertical and wind flow direction (see Figure 2.2).

iii) Following the equation of motion and the wind flow imposed, parameters that influence trajectories are particle diameter d and the wind flow parameters, i.e. the shear velocity u^* and the aerodynamic surface roughness z_0.

The trajectories are then computed for each value of a grid of parameters $e_1, \theta_1, \varphi_1, d, u^*, z_0$. The numerical integration for a given particle is stopped as soon as it impacts on the ground which means:

$$z \leq 0$$

We point out that the *ground* is composed by sand particles arranged in random geometries, then the sand bad is not exactly *flat*. Anyway, the ground surface can be thought as the mean surface that follows the particles geometries. The lack of detail is balanced by numerical errors introduced by numerical integration of Eq. (2.1). Since Eq. (2.1) solves for particle velocity, initial conditions $(e_1, \theta_1, \varphi_1)$ and d are converted into ejection velocity $\vec{v}_{ej}$ by:

$$\begin{cases} \|\vec{v}_{ej}\| &= \sqrt{\dfrac{2e_1}{m}} \\ \vec{v}_{ej} &= (\|\vec{v}_{ej}\|\cos\varphi_1\sin\theta_1,\ \|\vec{v}_{ej}\|\sin\varphi_1\sin\theta_1,\ \|\vec{v}_{ej}\|\cos\theta_1) \end{cases} \tag{2.3}$$

where particle mass is computed from particle diameter d by (2.2). The collected information for each trajectory are:

i) impact position;

ii) impact kinetic energy e_0;

iii) impact angles θ_0 and φ_0 as defined previously (see Figure 2.3);

iv) time required to execute the trajectory, called *impact time*;

v) the maximum height reached by particle during its trajectory.

These information are presented in next sections. The impact velocity $\vec{v}_{imp}$ obtained at the end of the integration of (2.1) is converted into e_0, θ_0 and φ_0 by:

$$\begin{cases} e_0 &= \frac{1}{2} m \|\vec{v}_{imp}\|^2 \\ \theta_0 &= \arctan\left(\frac{\sqrt{(v_{imp,x})^2 + (v_{imp,y})^2}}{\mid v_{imp,z} \mid}\right) \\ \varphi_0 &= \arctan\left(\frac{v_{imp,y}}{v_{imp,x}}\right) \end{cases} \tag{2.4}$$

where m is computed by (2.2).

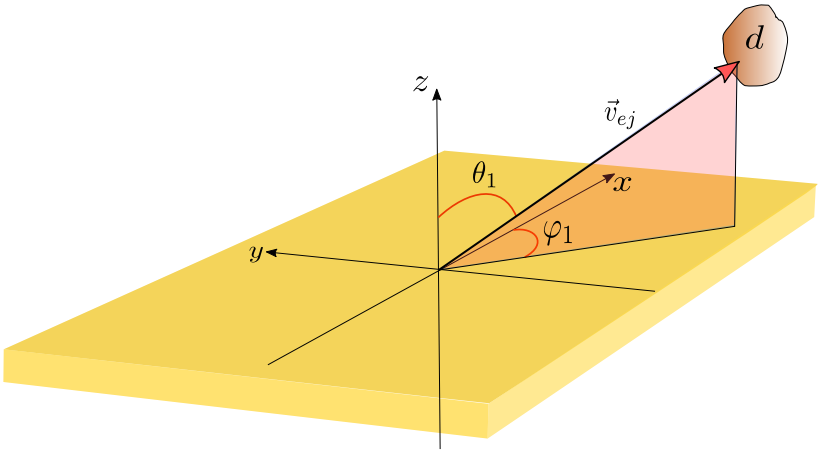

Figure 2.2: Scheme of particle ejection, with the definition of angles θ_1 and φ_1; d is the particle equivalent diameter and $\vec{v}_{ej}$ is the ejection velocity.

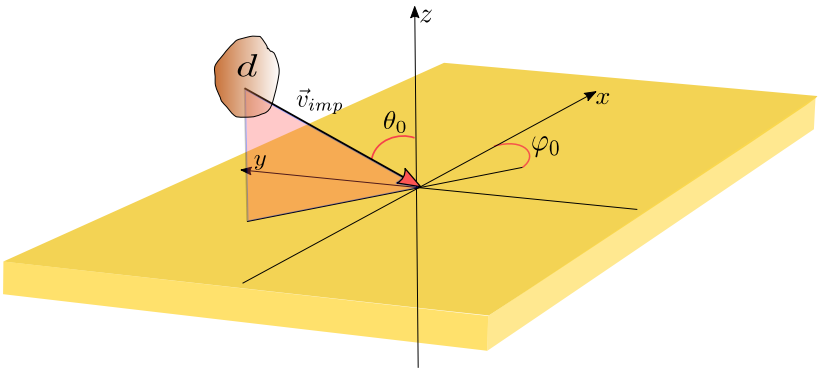

Figure 2.3: Scheme of particle impact, with the definition of angles θ_0 and φ_0; d is the particle equivalent diameter and $\vec{v}_{imp}$ is the impact velocity.

Computational Considerations The values of initial conditions and parameters chosen for the trajectory database are reported in Table 2.1. Wind flow imposes a symmetry of trajectories with respect to the x-axis, then we have chosen $\varphi_1 \in [0°, 180°]$. The equation (2.1) has been integrated using the explicit Newmark method (see Newmark 1959). Time step used for integrating the equation of motion has been chosen according to the value of ejection energy e_1 and diameter of particle d. In fact, the larger the diameter and the lower the ejection energy are, the shorter the trajectory is. So, for low values of energy and large values of diameter, time step has been chosen shorter in order to reduce numerical errors. We have considered the time step as function of particle diameter and ejection energy. This relation has been obtained by a finite linear element

on rectangle by imposing time steps for minimum and maximum values of energy e_1 and diameter (see Table 2.2 and Figure 2.4).

Parameter	Value
$e_1\,[J]$	$1 \cdot 10^{-9}$, $2 \cdot 10^{-9}$, ..., $9 \cdot 10^{-9}$, $1 \cdot 10^{-8}$, $2 \cdot 10^{-8}$, ..., $9 \cdot 10^{-8}$, $1 \cdot 10^{-7}$, $2 \cdot 10^{-7}$, ..., $9 \cdot 10^{-7}$, $1 \cdot 10^{-6}$, $2 \cdot 10^{-6}$, ..., $9 \cdot 10^{-6}$, $1 \cdot 10^{-5}$
$\theta_1\,[deg]$	10°, 20°, 30°, 40°, 50°, 60°, 70°, 80°
$\varphi_1\,[deg]$	0°, 30°, 60°, 90°, 120°, 150°, 180°
$Diameter\,[m]$	$2 \cdot 10^{-4}$, $3 \cdot 10^{-4}$, $4 \cdot 10^{-4}$, $5 \cdot 10^{-4}$, $6 \cdot 10^{-4}$, $7 \cdot 10^{-4}$, $8 \cdot 10^{-4}$, $9 \cdot 10^{-4}$, $1 \cdot 10^{-3}$
$u^*\,[m/s]$	0.2, 0.3, 0.4, 0.5, 0.6, 0.7
$z_0\,[m]$	0.001

Table 2.1: Values of initial conditions and parameters used in the trajectory database.

	e_1^{min}	e_1^{max}
d^{min}	$1 \cdot 10^{-5}$	$1 \cdot 10^{-4}$
d^{max}	$1 \cdot 10^{-6}$	$1 \cdot 10^{-5}$

Table 2.2: Values of time steps imposed for minimum and maximum values of ejection energy e_1 and partice diameter d.

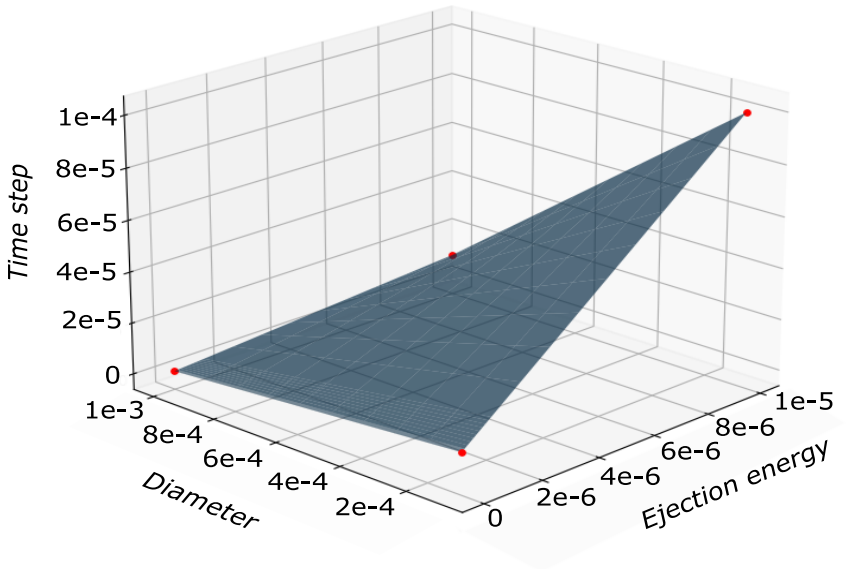

Figure 2.4: Time step used for numerical integration. It is imposed as a function of particle diameter and ejection energy in order to reduce numerical errors.

2.2 Geometry and Lifetime of the Trajectories

In Figures 2.5, 2.6 and 2.7 the projection of trajectories in the $x-z$ plane and the impact position in the $x-y$ plane are reported for different values of energy e_1 and angles θ_1, φ_1. In general, the larger the diameter is, the stronger the wind must be to influence trajectory of particle. It can be observed by the impact position in the $x-y$ plane that the more the impact points deviate from forming circles around the particle, the stronger the influence of wind on the trajectories is.

The particles displacement is reported in Figures 2.8 and 2.9. It corresponds to the distance of the impact point with respect to the ejection point. The initial angle φ_1 is fixed to 0° which means ejections in the wind direction. This case corresponds to the maximum displacement case. In Figure 2.8 the dependence on u^* is shown. The displacement is reported with contour plots with respect to initial conditions of energy e_1 and angle θ_1. The red lines identify initial conditions for which particles move one centimetre only. These initial conditions have little dependence on u^*. In Figure 2.9 the dependence on particle diameter is shown. In general, the stronger the wind is, the more the distance travelled with a certain initial energy e_1 increases. Anyway, displacement is also dependent on ejection direction. For a fix value of e_1, there is an angle θ_1^* for which displacement is maximum. This angle depends both on u^* and particle diameter. Further, the larger the particle is, the smaller the distance travelled with a certain initial energy is.

The maximum height reached by particles during their trajectories is shown in Figures 2.10 and 2.11 as contour plots with respect to initial conditions e_1 and θ_1. We set $\varphi_1 = 0°$. The figures show the dependence of the maximum height with respect to u^* and particle diameter. The red lines identify the initial conditions for which particles reach a maximum height equal to their diameters. The maximum height reached is strongly influenced by particle diameter, i.e. particle mass. In general, the maximum height is greater for quasi-vertical ejection directions.

The impact time is reported in Figures 2.12 and 2.13 as contour plots with respect to initial conditions e_1 and θ_1 while $\varphi_1 = 0°$. The figures show the dependence of the impact time with respect to u^* and particle diameter. The impact time is mainly influenced by particle mass i.e. its diameter. In general, fixing initial conditions for e_1 and θ_1 the impact time decreases as the particle diameter is increased. This is due to shorter trajectories. Further, the impact time increases for quasi-vertical ejection directions.

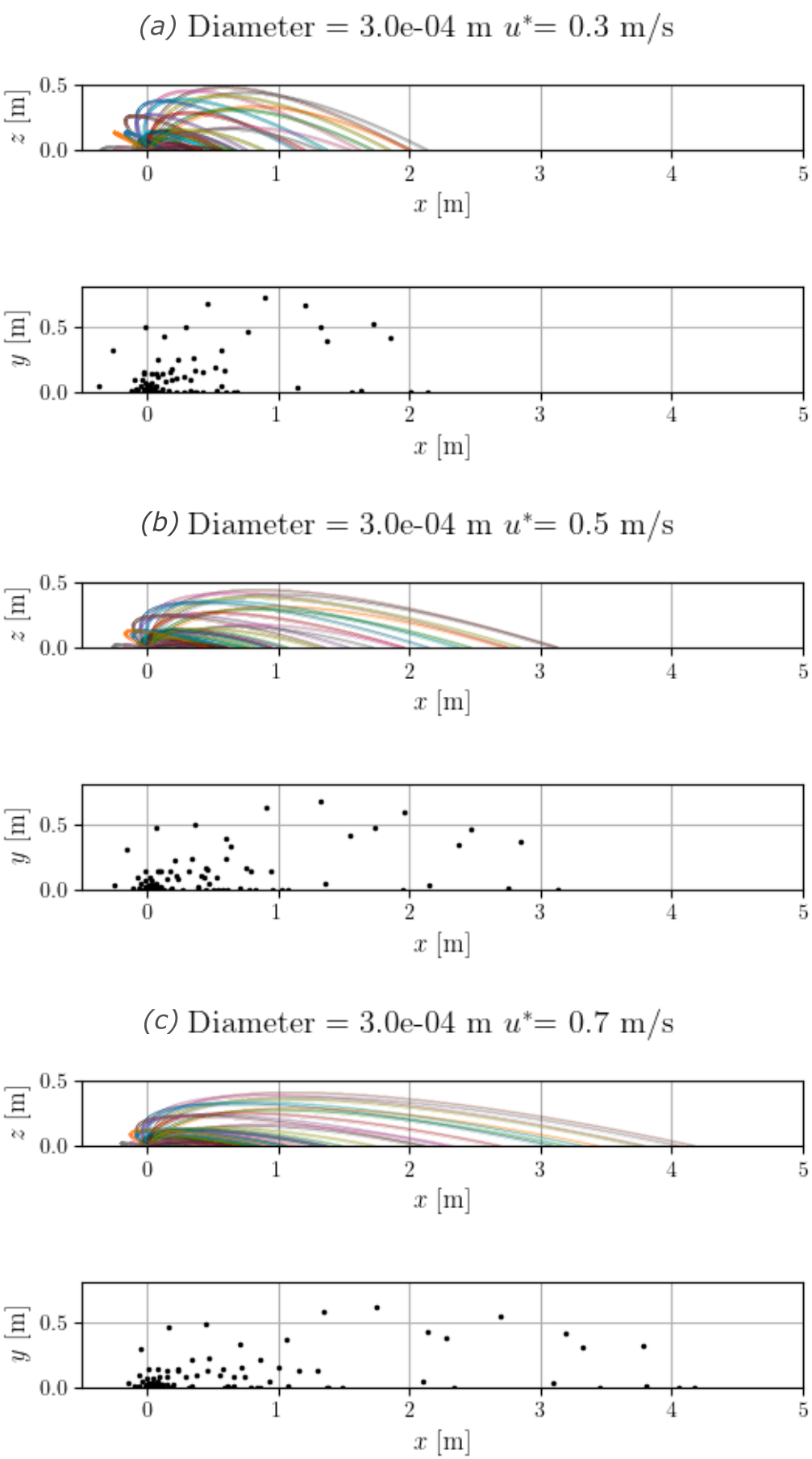

Figure 2.5: Trajectories of particle with diameter $d = 3 \cdot 10^{-4}\, m$ for different values of shear velocity: (a) $u^* = 0.3\, m/s$; (b) $u^* = 0.5\, m/s$; (c) $u^* = 0.7\, m/s$. The projections of trajectories in the $x - z$ plane are reported in the upper graphs and the impact position on the $x-y$ plane in the lower ones. Trajectories are computed for different values of ejection energy $e_1 \in \{1{\cdot}10^{-9}, 5{\cdot}10^{-9}, 1{\cdot}10^{-8}, 5{\cdot}10^{-8}, 1{\cdot}10^{-7}, 5{\cdot}10^{-7}\}\, J$ and five equally spaced values of angles $\theta_1 \in [10°, 80°]$ and $\varphi_1 \in [0°, 175°]$.

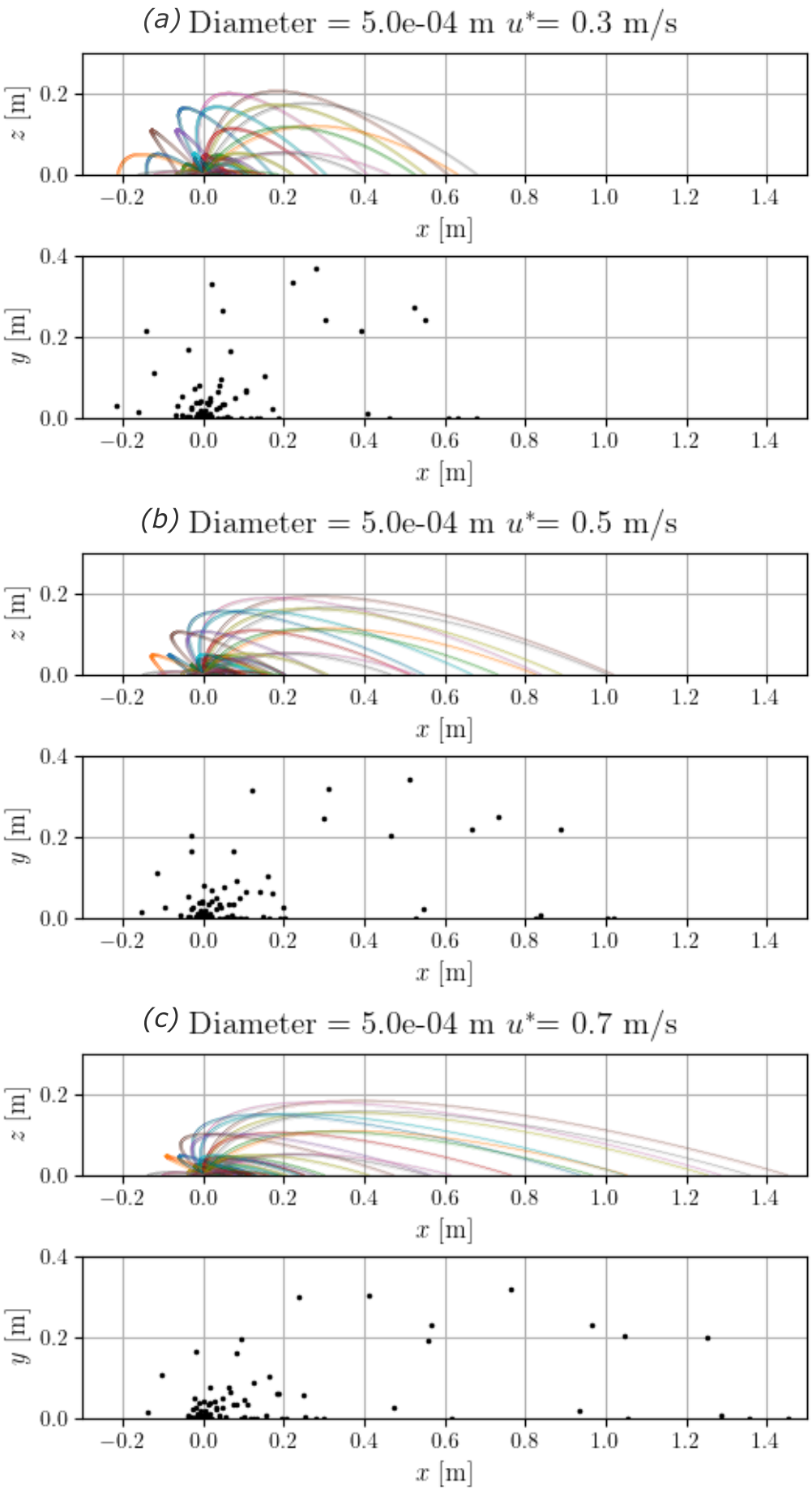

Figure 2.6: Trajectories of particle with diameter $d = 5 \cdot 10^{-4}\, m$ for different values of shear velocity: (a) $u^* = 0.3\, m/s$; (b) $u^* = 0.5\, m/s$; (c) $u^* = 0.7\, m/s$. The projections of trajectories in the $x - z$ plane are reported in the upper graphs and the impact position on the $x-y$ plane in the lower ones. Trajectories are computed for different values of ejection energy $e_1 \in \{1{\cdot}10^{-9}, 5{\cdot}10^{-9}, 1{\cdot}10^{-8}, 5{\cdot}10^{-8}, 1{\cdot}10^{-7}, 5{\cdot}10^{-7}\}\, J$ and five equally spaced values of angles $\theta_1 \in [10°, 80°]$ and $\varphi_1 \in [0°, 175°]$.

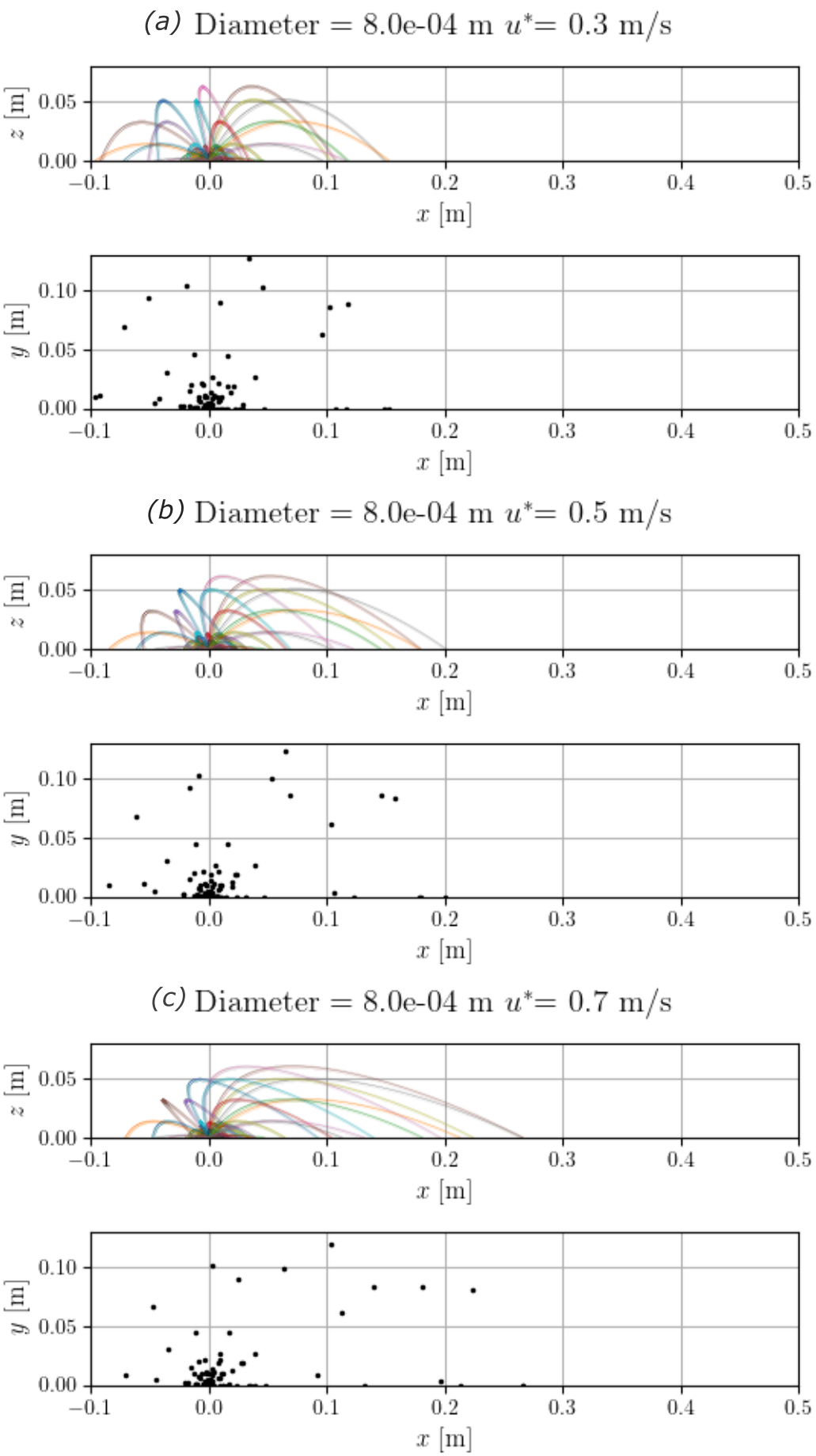

Figure 2.7: Trajectories of particle with diameter $d = 8 \cdot 10^{-4}\, m$ for different values of shear velocity: (a) $u^* = 0.3\, m/s$; (b) $u^* = 0.5\, m/s$; (c) $u^* = 0.7\, m/s$. The projections of trajectories in the $x - z$ plane are reported in the upper graphs and the impact position on the $x-y$ plane in the lower ones. Trajectories are computed for different values of ejection energy $e_1 \in \{1{\cdot}10^{-9}, 5{\cdot}10^{-9}, 1{\cdot}10^{-8}, 5{\cdot}10^{-8}, 1{\cdot}10^{-7}, 5{\cdot}10^{-7}\}\, J$ and five equally spaced values of angles $\theta_1 \in [10°, 80°]$ and $\varphi_1 \in [0°, 175°]$.

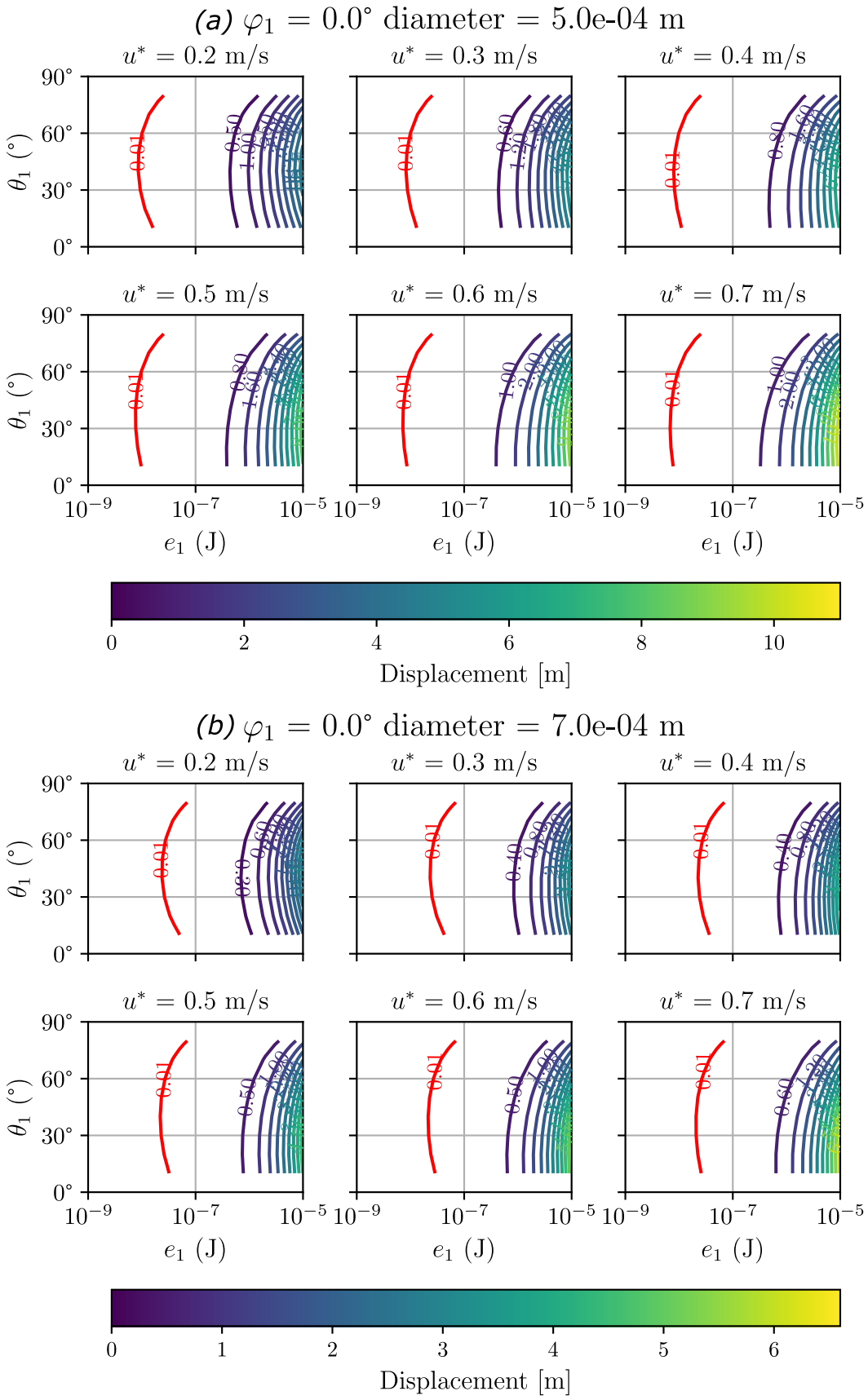

Figure 2.8: Particle displacement from its starting point for (a) $d = 5 \cdot 10^{-4}\, m$ and (b) $d = 7 \cdot 10^{-4}\, m$, and for $u^* = 0.2$, 0.3, 0.4, 0.5, 0.6, $0.7\, m/s$. Displacements are reported as contour plots with respect to initial conditions of energy e_1 and angle θ_1 while angle φ_1 is set equal to 0°. The red lines identify initial conditions for which particles moves one centimetre only.

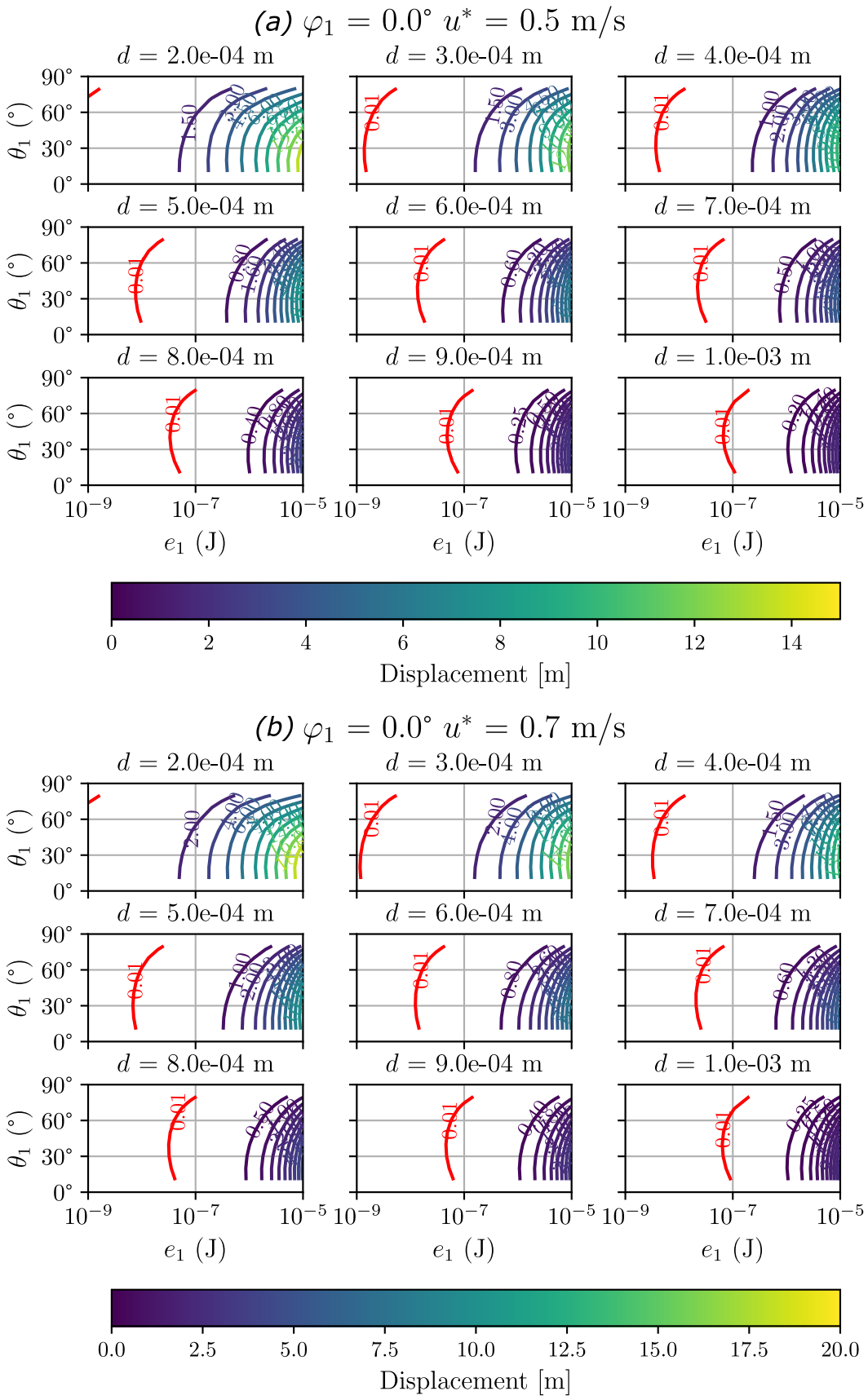

Figure 2.9: Particle displacement from its starting point for (a) $u^* = 0.5\,m/s$ and (b) $u^* = 0.7\,m/s$, and for $d = 2 \cdot 10^{-4}$, $3 \cdot 10^{-4}$, $4 \cdot 10^{-4}$, $5 \cdot 10^{-4}$, $6 \cdot 10^{-4}$, $7 \cdot 10^{-4}$, $8 \cdot 10^{-4}$, $9 \cdot 10^{-4}$, $1 \cdot 10^{-3}\,m$. Displacements are reported as contour plots with respect to initial conditions of energy e_1 and angle θ_1 while angle φ_1 is set equal to 0°. The red lines identify initial conditions for which particles moves one centimetre only.

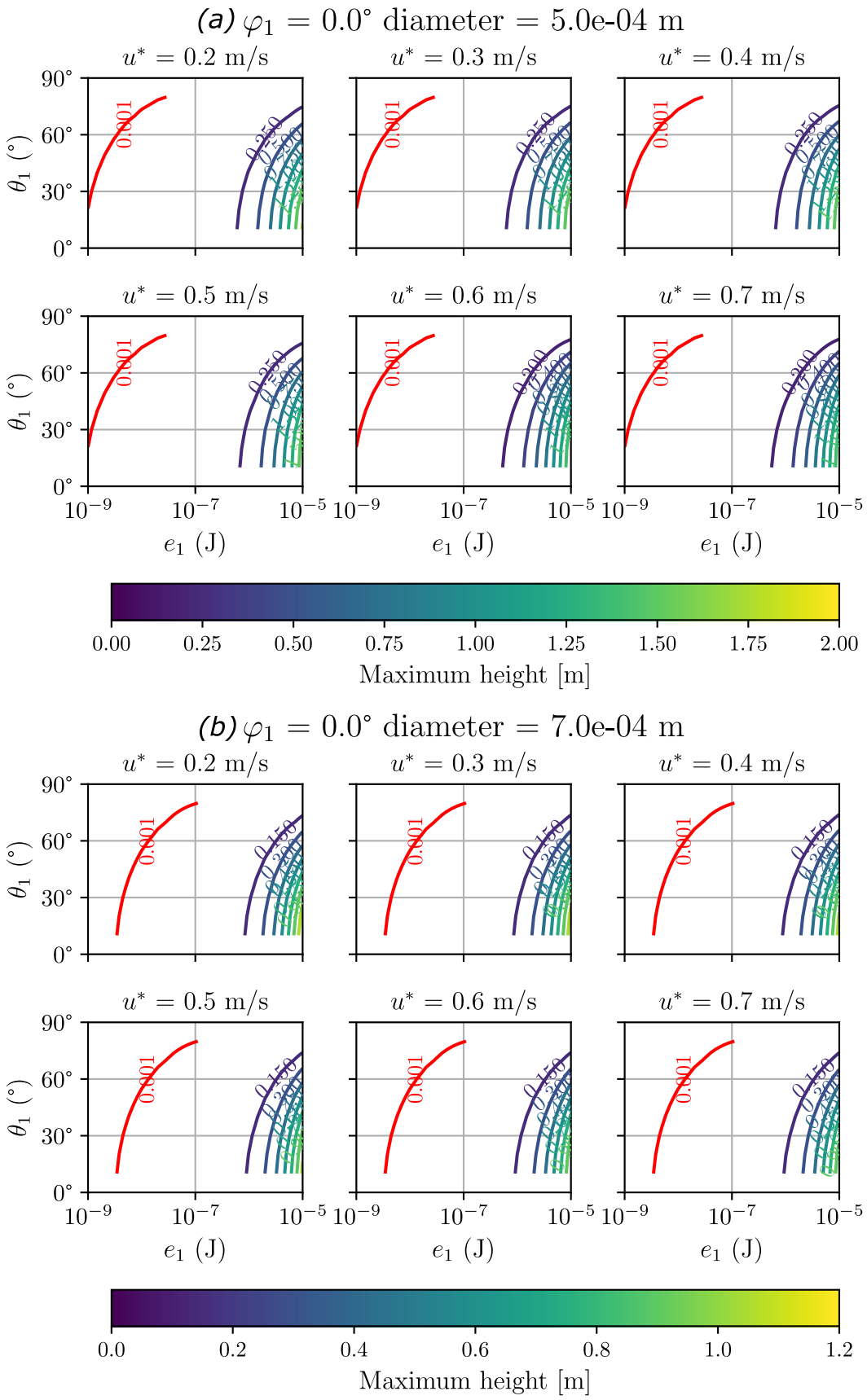

Figure 2.10: Maximum height reached by particle during its trajectory for (a) $d = 5 \cdot 10^{-4}\, m$ and (b) $d = 7 \cdot 10^{-4}\, m$, and for $u^* = 0.2$, 0.3, 0.4, 0.5, 0.6, $0.7\, m/s$. It is reported as contour plots with respect to initial conditions of energy e_1 and angle θ_1 while angle φ_1 is set equal to 0°. The red lines identifies initial conditions for which particles reach a maximum height equal to their diameters.

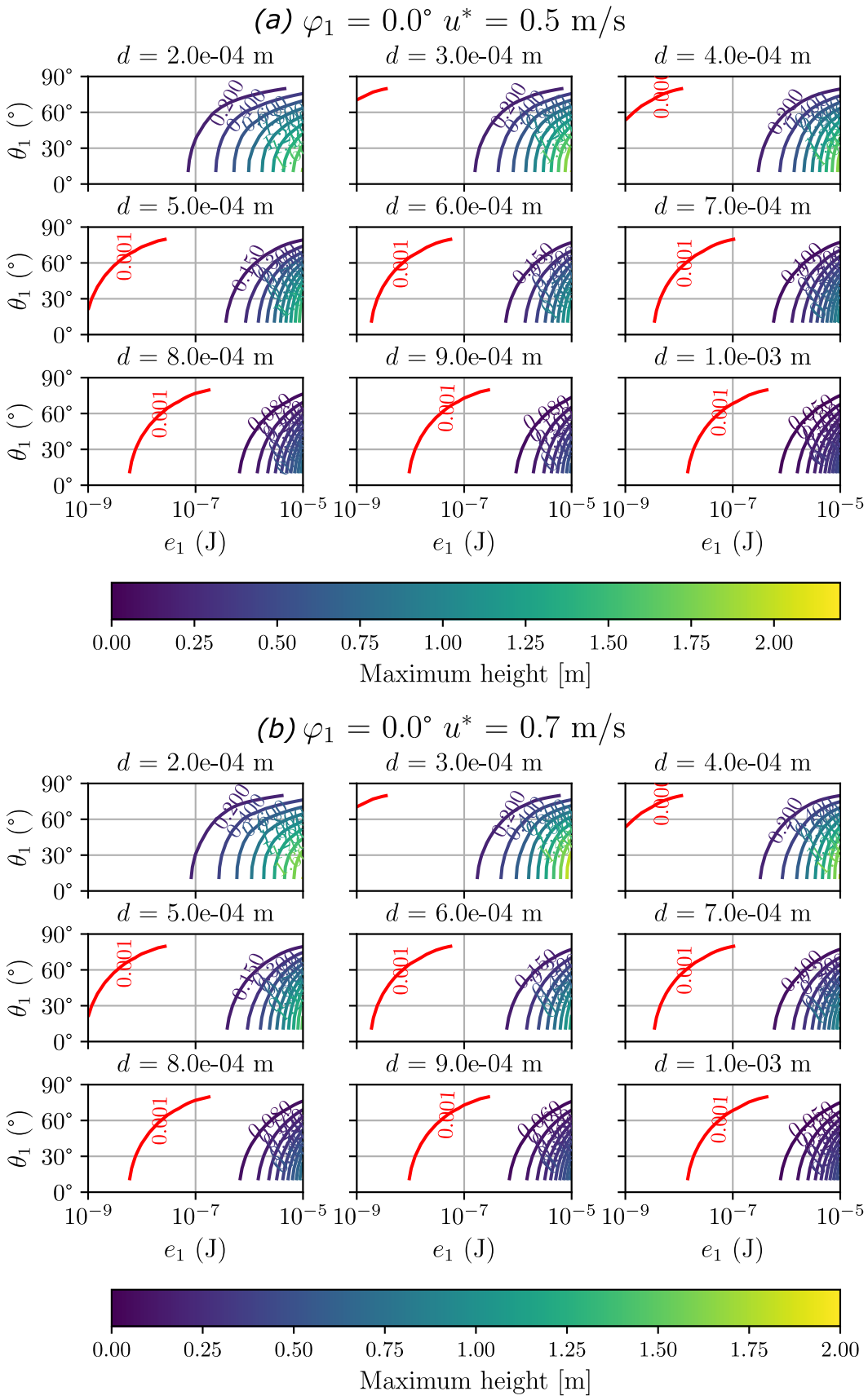

Figure 2.11: Maximum height reached by particle during its trajectory for (a) $u^* = 0.5\,m/s$ and (b) $u^* = 0.7\,m/s$, and for $d = 2\cdot10^{-4}$, $3\cdot10^{-4}$, $4\cdot10^{-4}$, $5\cdot10^{-4}$, $6\cdot10^{-4}$, $7\cdot10^{-4}$, $8\cdot10^{-4}$, $9\cdot10^{-4}$, $1\cdot10^{-3}\,m$. It is reported as contour plots with respect to initial conditions of energy e_1 and angle θ_1 while angle φ_1 is set equal to 0°. The red lines identifies initial conditions for which particles reach a maximum height equal to their diameters.

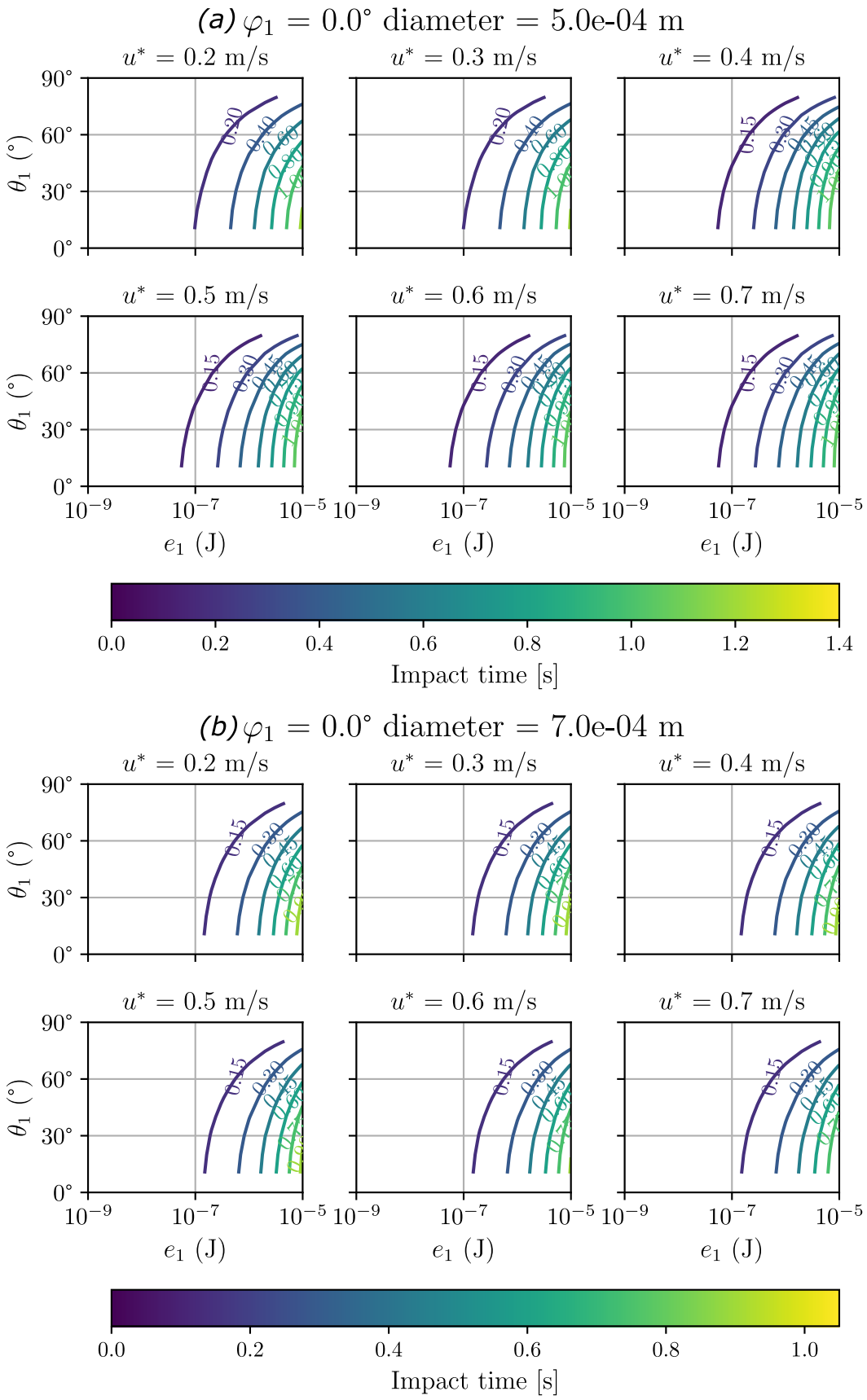

Figure 2.12: Impact time for (a) $d = 5 \cdot 10^{-4}\,m$ and (b) $d = 7 \cdot 10^{-4}\,m$, and for $u^* = 0.2, 0.3, 0.4, 0.5, 0.6, 0.7\,m/s$. It is reported as contour plots with respect to initial conditions of energy e_1 and angle θ_1 while angle φ_1 is set equal to 0°.

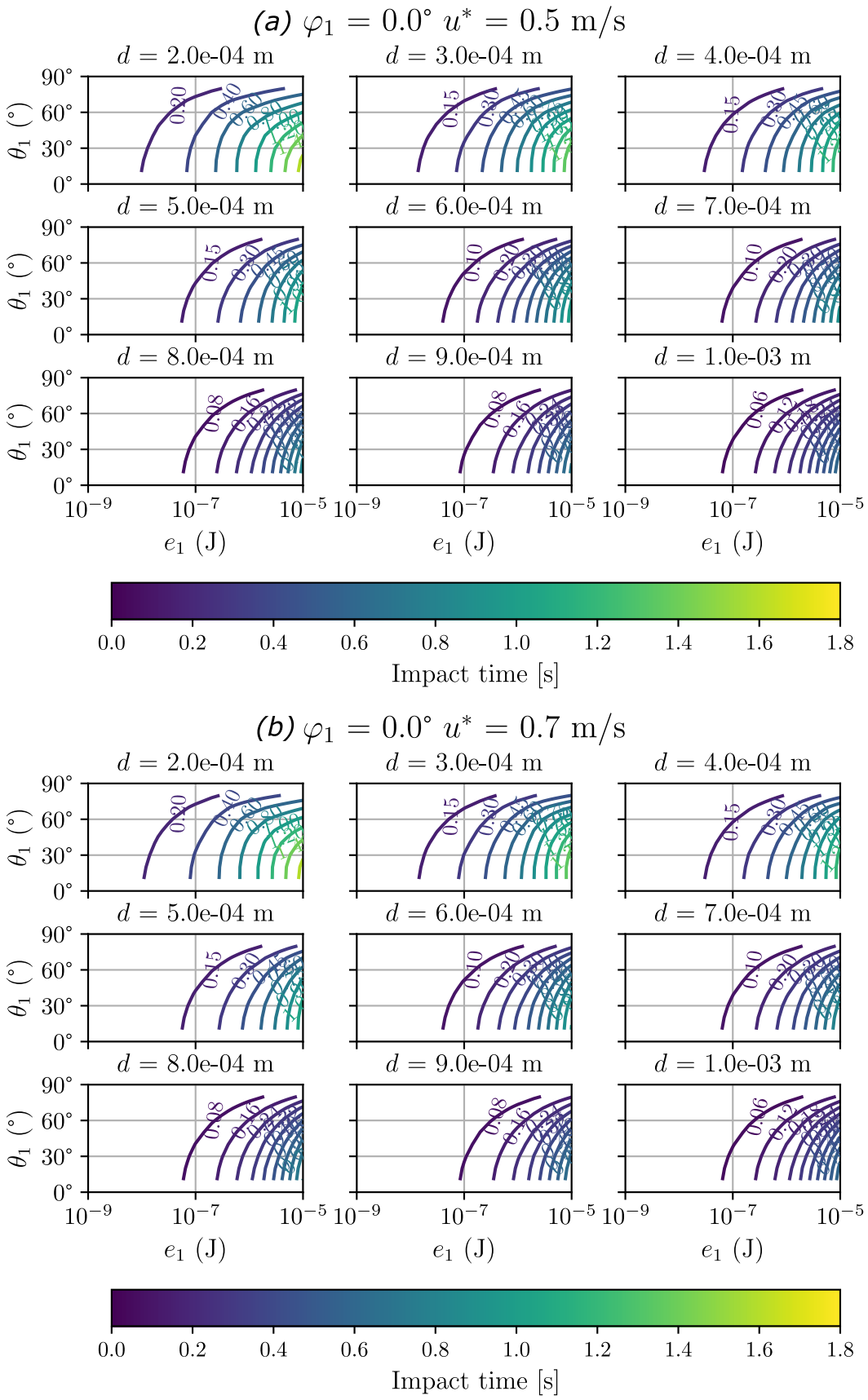

Figure 2.13: Impact time for (a) $u^* = 0.5\,m/s$ and (b) $u^* = 0.7\,m/s$, and for $d = 2 \cdot 10^{-4}$, $3 \cdot 10^{-4}$, $4 \cdot 10^{-4}$, $5 \cdot 10^{-4}$, $6 \cdot 10^{-4}$, $7 \cdot 10^{-4}$, $8 \cdot 10^{-4}$, $9 \cdot 10^{-4}$, $1 \cdot 10^{-3}\,m$. It is reported as contour plots with respect to initial conditions of energy e_1 and angle θ_1 while angle φ_1 is set equal to 0°.

2.3 Energy Gain

Trajectories have a key role in saltation: particles gain (or eventually lose) energy as they move through the wind flow. We can identify the *saltation system* as the ensemble of saltating particles. The energy of the system (i.e. the sum of the kinetic energy of particles) could be a good proxy for the saltation process. In fact, the more particles are energised by the wind, the more they are able to lift other particles off the ground during impacts. It depends on the *impact model* and it will be discussed in Chapter 4. Then the particles number increases as the energy of system increases. The wind flow can be thought as an external source that transmits energy through trajectories.
The ratio between the impact energy e_0 and the ejection energy e_1 is reported in the figures below. It represents the gain or loss of energy during trajectory: particle gains energy by the wind flow if the ratio is greater than one. In fact, it impacts the ground with a higher energy than when it leaves it. A region of positive energy gain in the space of initial conditions $(e_1, \theta_1, \varphi_1)$ is identified, i.e. a region of initial conditions for which particle gain energy by the wind. For ease of reading the contour plot of e_0/e_1 is reported for different values of φ_1 in Figure 2.14. The region of energy gain is enclosed by the red lines. The energy loss for large values of ejection energy is due to the drag effect on too fast particles. Instead, the energy loss for small values of ejection energy is due to trajectories that are too low. In fact, the logarithmic profile of wind imposes that particles executing low trajectories move on almost stationary air, experiencing friction. This is also the reason for energy loss for almost horizontally oriented ejections.
We point out that the impact and fluid entrainment models identify the ejection conditions for particles (see Chapter 3), and the energy gain of particles depends on their ejection conditions. Then the impact and fluid entrainment models also has control over the energy gain of the system. They play a crucial role in the saltation process simulation.

The region of energy gain depends on particle diameter and wind flow. The dependence of the energy gain from particle diameter and shear velocity u^* is shown in Figures 2.16 and 2.15. As the diameter increases, e_1 must also increase in order to gain energy from the wind flow. So, the region of energy gain moves to the right. Instead, fixing the particle diameter and increasing the shear velocity u^*, the region of energy gain expands, i.e. the number of initial conditions for which particle gain energy increases.

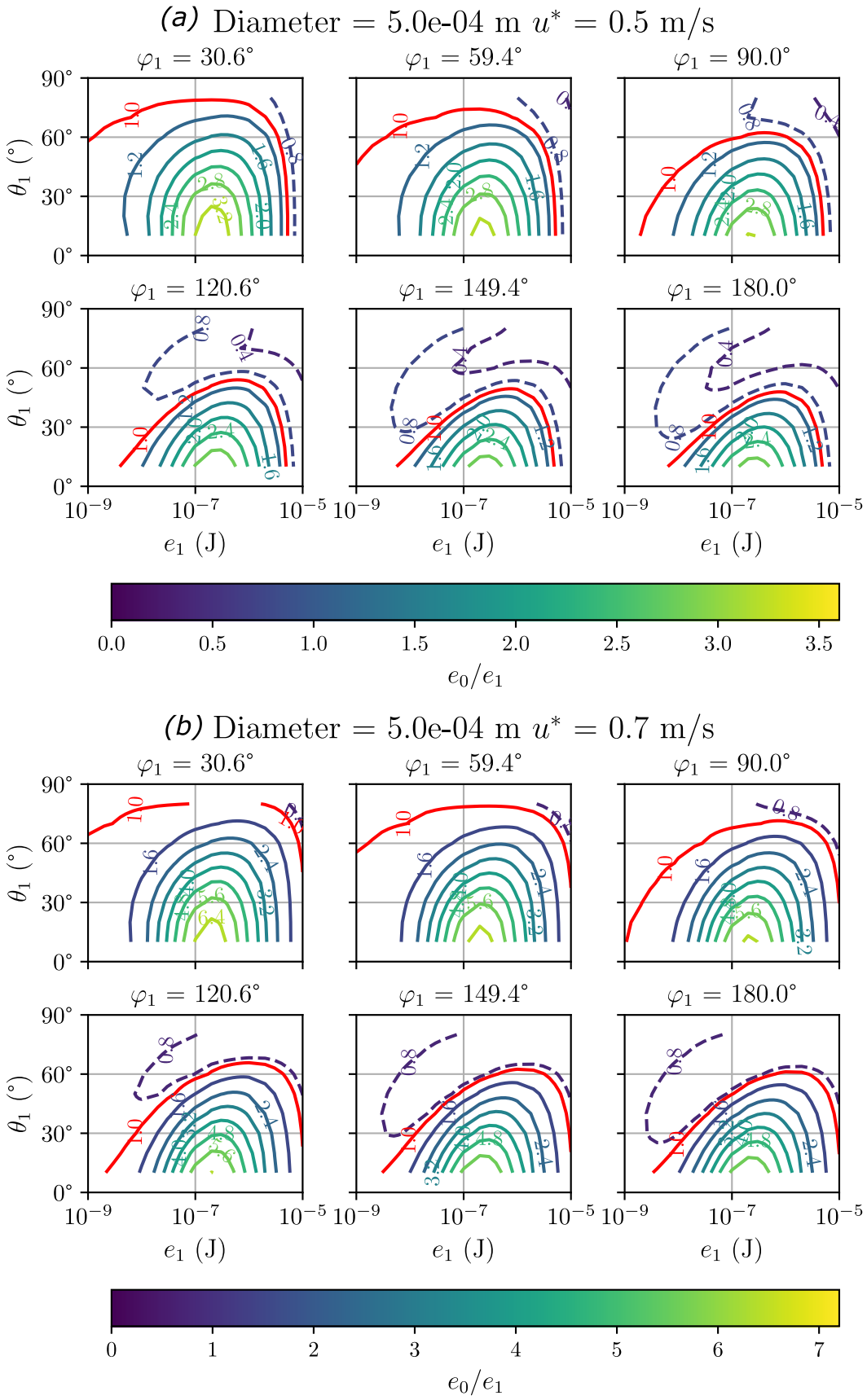

Figure 2.14: Ratio between impact energy e_0 and ejection energy e_1 represented by contour plots in the $e_1 - \theta_1$ plane, for different values of angle φ_1. The region of energy gain is enclosed by red lines. Particle diameter is fixed to $5 \cdot 10^{-4}\, m$ while we set (a) $u^* = 0.5\, m/s$ and (b) $u^* = 0.7\, m/s$. The region of energy loss is identified by the dotted lines.

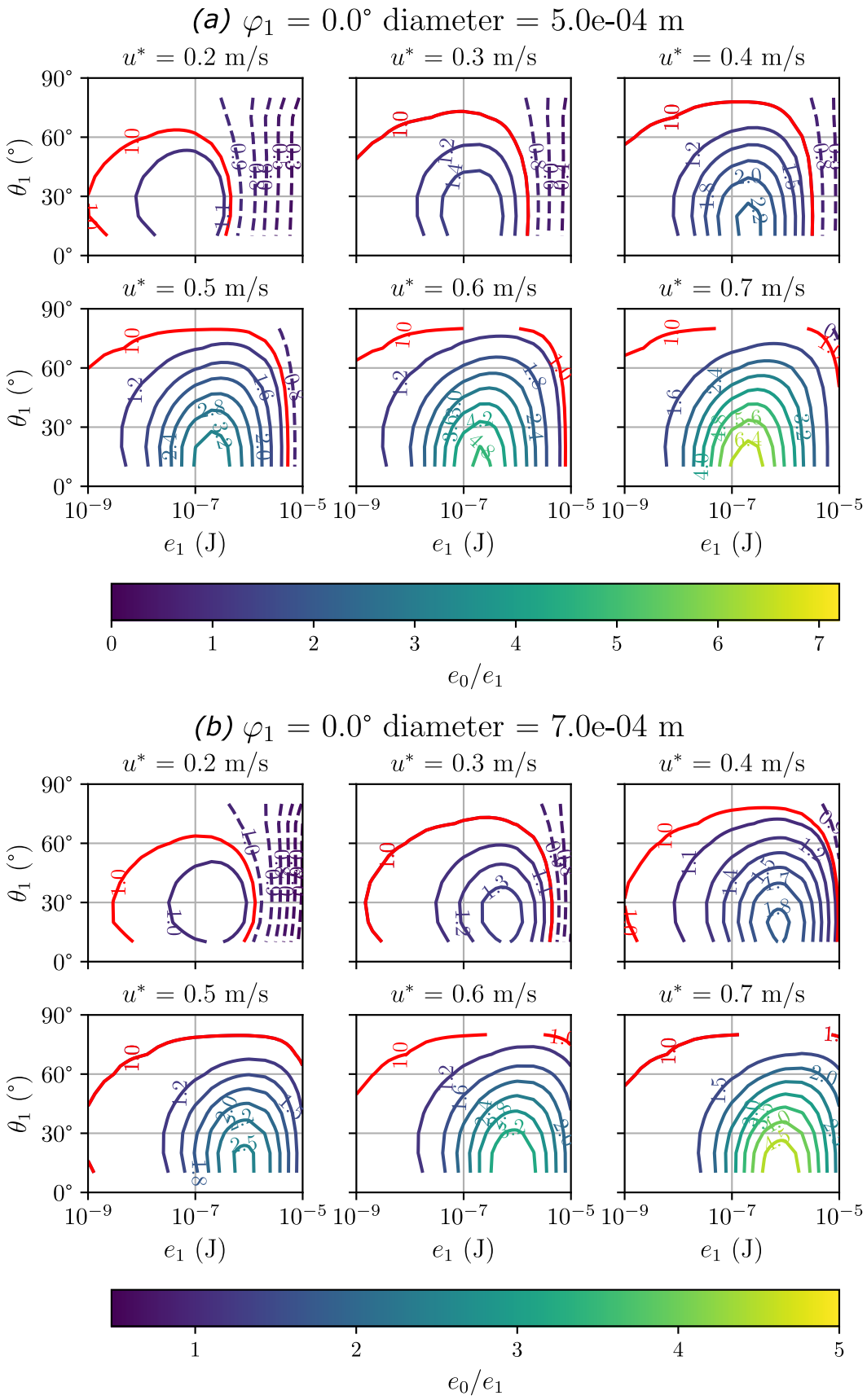

Figure 2.15: Ratio between impact energy e_0 and ejection energy e_1 for (a) $d = 5 \cdot 10^{-4}\,m$ and (b) $d = 7 \cdot 10^{-4}\,m$, and for $u^* = 0.2$, 0.3, 0.4, 0.5, 0.6, $0.7\,m/s$ It is represented by contour plots with respect to initial conditions of energy e_1 and angle θ_1 while angle φ_1 is set equal to 0°. The region of energy gain is enclosed by red lines. The region of energy loss is identified by the dotted lines.

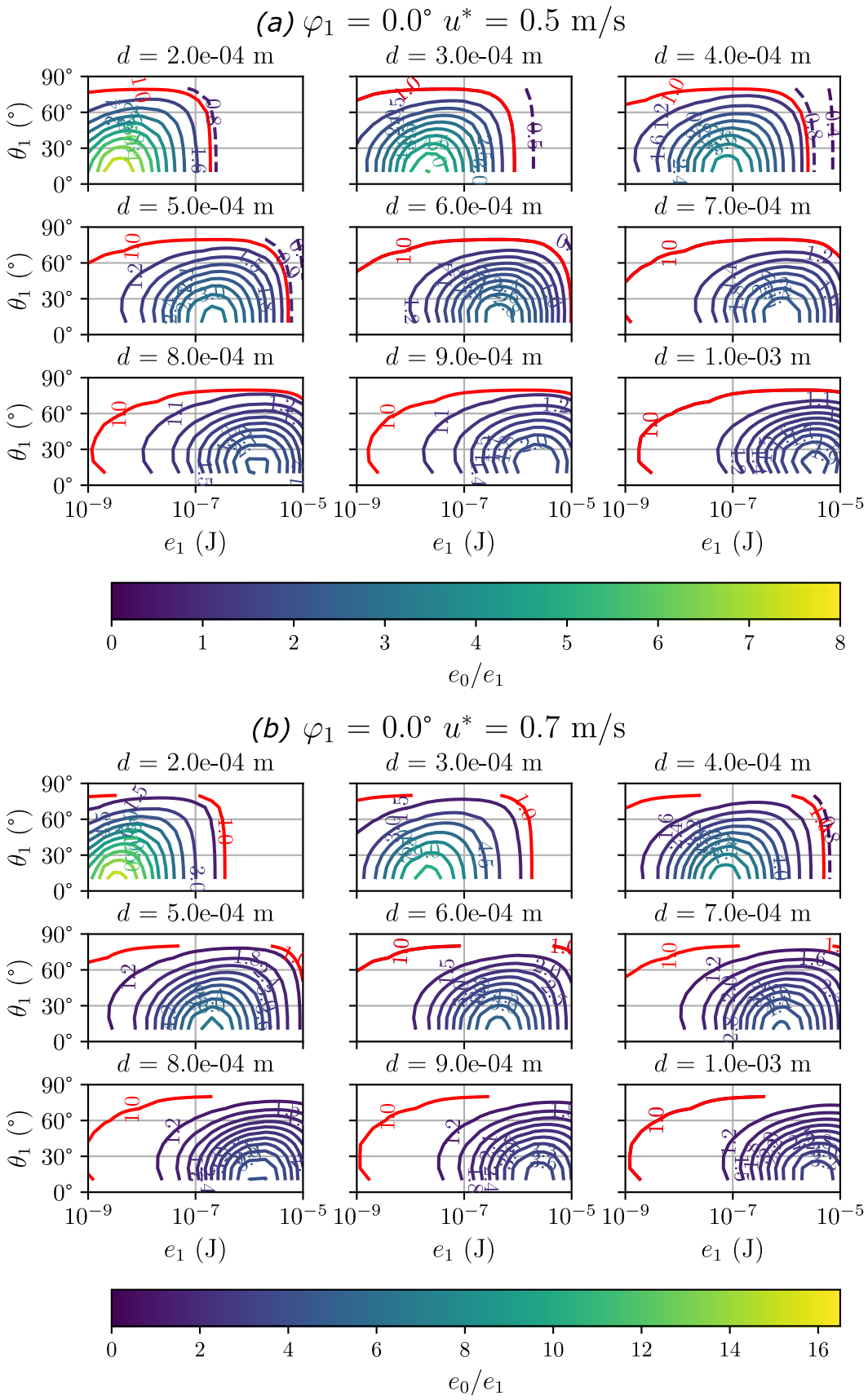

Figure 2.16: Ratio between impact energy e_0 and ejection energy e_1 for (a) $u^* = 0.5\,m/s$ and (b) $u^* = 0.7\,m/s$, and for $d = 2\cdot10^{-4}$, $3\cdot10^{-4}$, $4\cdot10^{-4}$, $5\cdot10^{-4}$, $6\cdot10^{-4}$, $7\cdot10^{-4}$, $8\cdot10^{-4}$, $9\cdot10^{-4}$, $1\cdot10^{-3}\,m$. It is represented by contour plots with respect to initial conditions of energy e_1 and angle θ_1 while angle φ_1 is set equal to 0°. The region of energy gain is enclosed by red lines. The region of energy loss is identified by the dotted lines.

2.4 Trajectories as Vector Field

Assuming to omit turbulence effects on particle motion, particle trajectories could be seen as a deterministic function $\mathcal{T}$, that we call *trajectory function*, linking ejection information to impact information. So, the input is represented by:

i) the kinetic energy e_1 of ejection;

ii) the angles θ_1 and φ_1 of ejection (see Figure 2.2).

while the output of the trajectory function gives:

i) the kinetic energy e_0 of impact;

ii) the angles θ_0 and φ_0 of impact as defined previously (see Figure 2.3).

The particle diameter d is a parameter of the trajectory function, as well as the shear velocity u^* and the aerodynamic surface roughness z_0 that describe the wind flow. We can then define a vector field $\mathcal{T}_{(d,u^*,z_0)}$ on the space of energy and angles (e, θ, φ) which depends on parameters (d, u^*, z_0):

$$\begin{aligned} \mathcal{T}_{(d,u^*,z_0)} : \mathbb{R}_+ \times \left[0, \frac{\pi}{2}\right] \times [0,2\pi] &\longrightarrow \mathbb{R}_+ \times \left[0, \frac{\pi}{2}\right] \times [0,2\pi] \\ (e_1, \theta_1, \varphi_1) &\longmapsto (e_0, \theta_0, \varphi_0) \end{aligned} \tag{2.5}$$

We point out that outputs of trajectory function correspond to input information used in the *impact model* that will be discussed in Chapter 4. In fact, the impact model is based on impact energy and angles and it defines the energy e_1, angles θ_1, φ_1 and diameter d of each ejected particles. In the same way, outputs of the impact model corresponds to inputs of the trajectory function. The process of particles ejections and impacts could then be described through the combination of the trajectory function $\mathcal{T}$ and the impact model (see Figure 2.17).

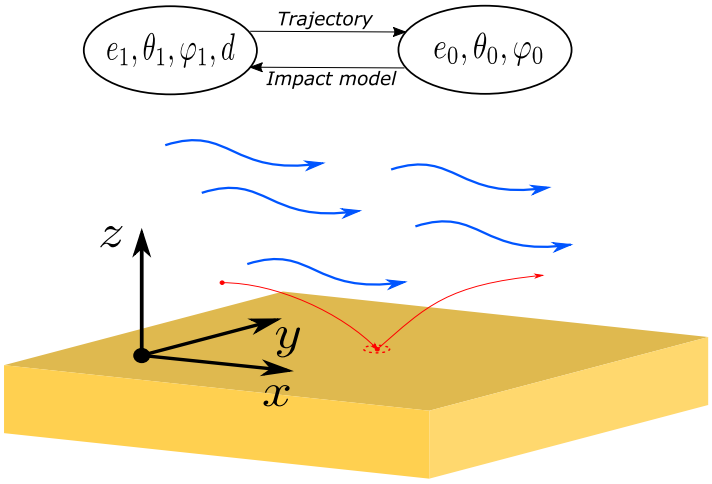

Figure 2.17: Scheme of the process of particle ejections and impacts described through the combination of the trajectory function $\mathcal{T}_{(d,u^*,z_0)}$ and the impact model.

For ease of reading in Figure 2.18 the simulated inputs of the trajectory function are reported, while the outputs are reported in Figures 2.19 and 2.20 for different values of diameters and shear velocities u^*. As we can see, the smaller the particle or the stronger the wind is, the more likely particle is forced to impact with $\varphi_0 = 0°$, that is, it tends to align with the wind direction.
The projection of the vector field in the $e-\theta$ plane is reported in Figures 2.21 and 2.22 for $\varphi_1 = 0°$

and several values of d and u^*. Since ejection direction is parallel to wind direction, impact angle φ_0 will be 0°. So, for $\varphi_1 = 0°$ the vector field lives in the $e - \theta$ plane. In Figure 2.21 the effect of increasing the wind strenght is reported. Increasing u^*, particles impact at an increasingly horizontal angle and increased energy with respect to ejection energy. For large values of e_1 particles impact with less energy than ejection energy, due to drag effect on too fast particles with respect to wind speed. It can be seen also from the energy gain plots of the previous section. The effect of changing particle diameter is reported in Figure 2.22. As we can see, the effect of decreasing particle diameter and fixed u^* is similar to increasing the wind strenght and keeping a fixed diameter.
To summarise the smaller the particle or the stronger the wind is, the more particle will tend to align to the wind, gain more energy and impact at very large angles (which means horizontal impacts).

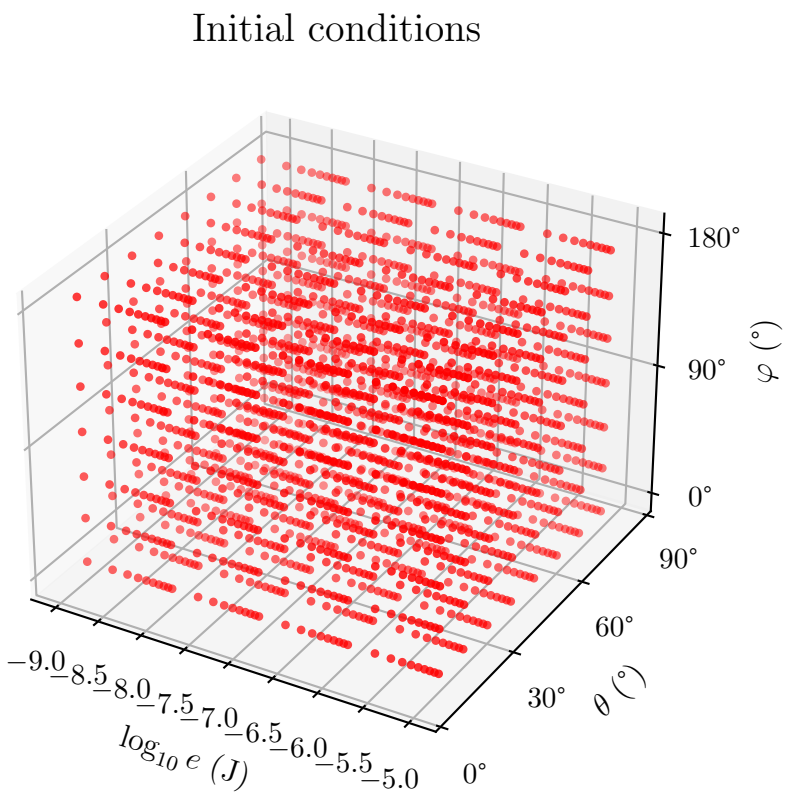

Figure 2.18: Initial conditions of energy e_1 and angles θ_1 and φ_1 used to build the trajectory database.

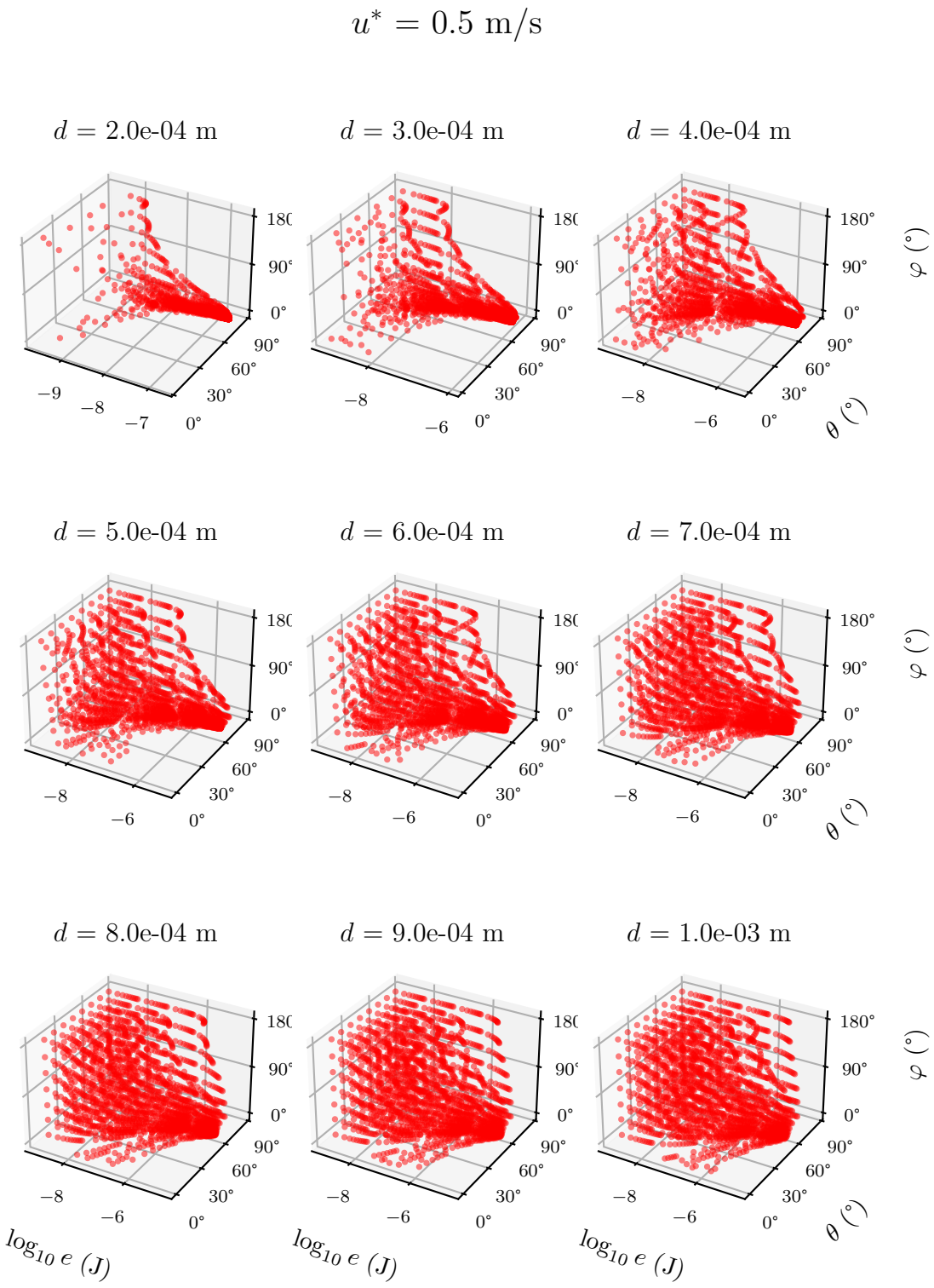

Figure 2.19: Impact conditions of energy e_0 and angles θ_0 and φ_0 for different values of particle diameter and $u^* = 0.5\,m/s$. Initial conditions correspond to Figure 2.18.

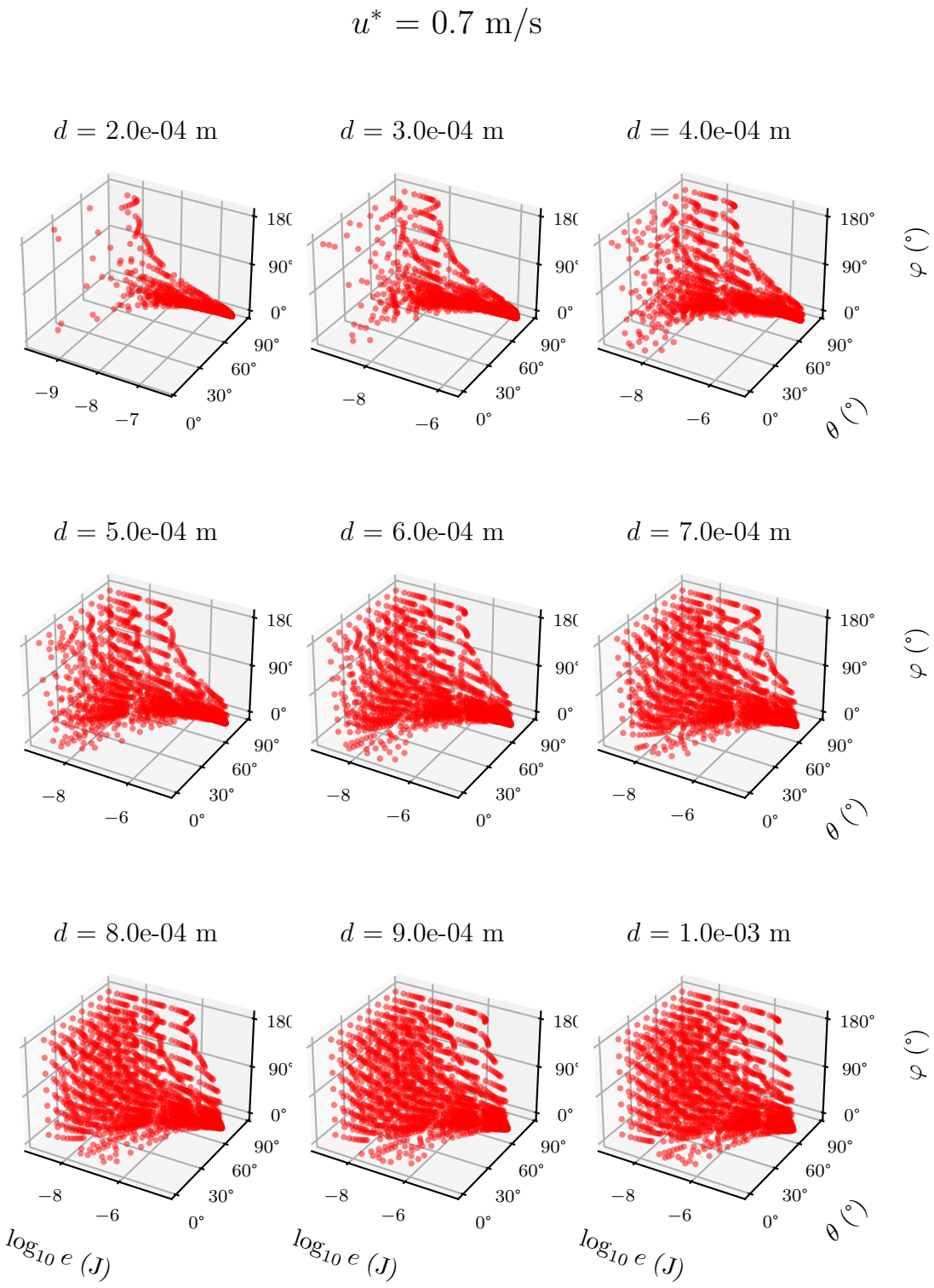

Figure 2.20: Impact conditions of energy e_0 and angles θ_0 and φ_0 for different values of particle diameter and $u^* = 0.7\,m/s$. Initial conditions correspond to Figure 2.18.

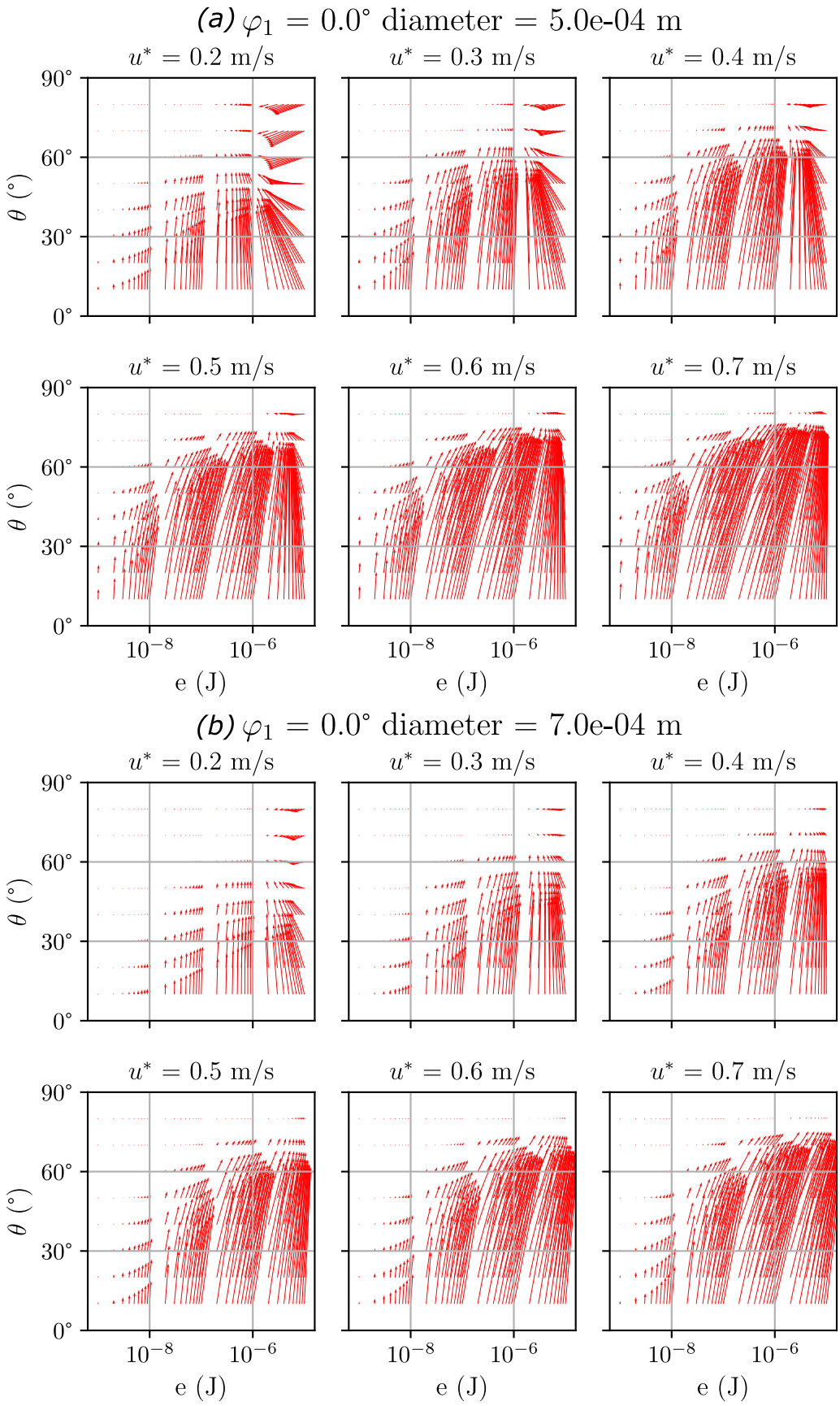

Figure 2.21: Trajectory function in the $e - \theta$ plane for (a) $d = 5 \cdot 10^{-4}\, m$ and (b) $d = 7 \cdot 10^{-4}\, m$, and for $u^* = 0.2$, 0.3, 0.4, 0.5, 0.6, $0.7\, m/s$.

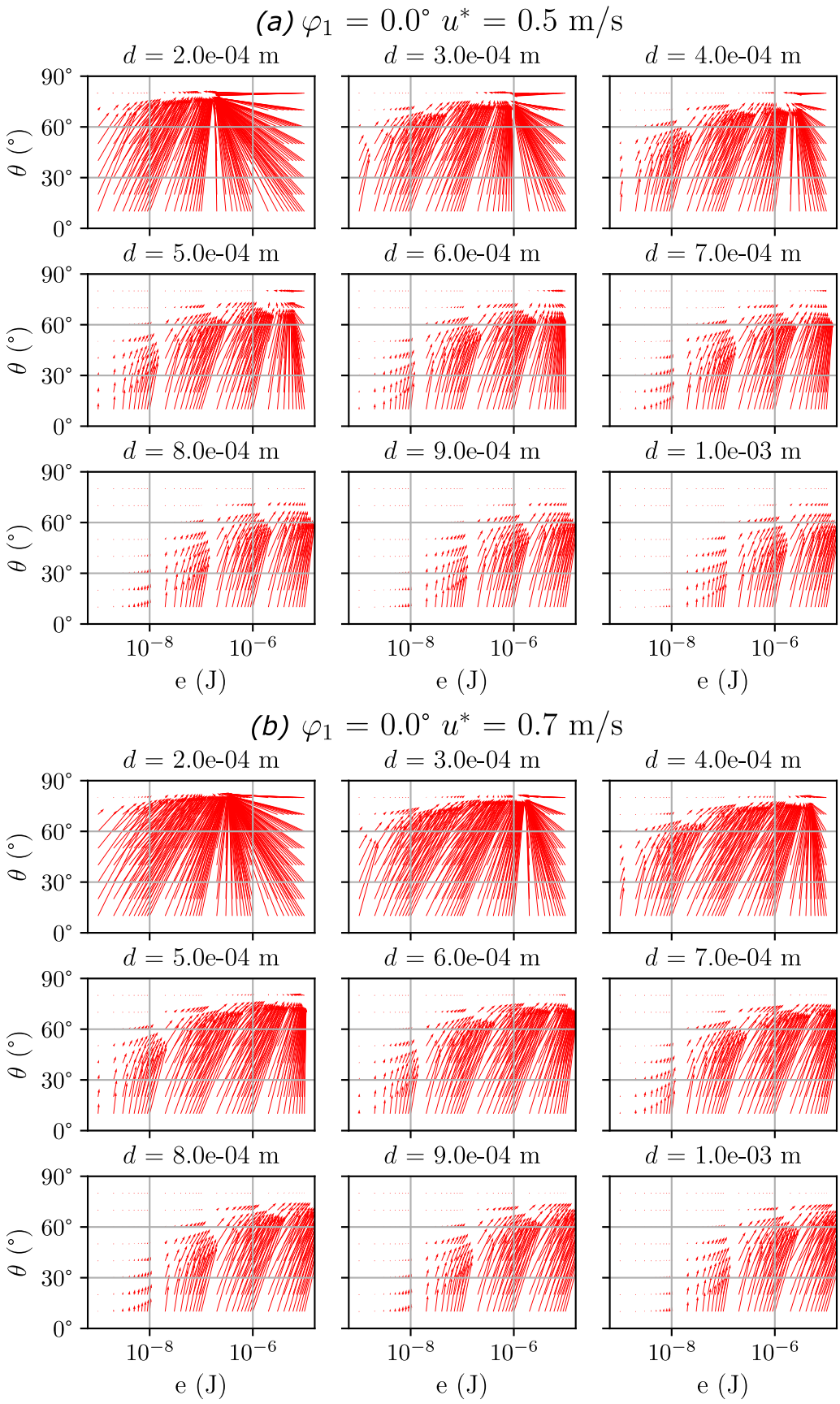

Figure 2.22: Trajectory function in the $e - \theta$ plane for (a) $u^* = 0.5\,m/s$ and (b) $u^* = 0.7\,m/s$, and for $d = 2 \cdot 10^{-4}$, $3 \cdot 10^{-4}$, $4 \cdot 10^{-4}$, $5 \cdot 10^{-4}$, $6 \cdot 10^{-4}$, $7 \cdot 10^{-4}$, $8 \cdot 10^{-4}$, $9 \cdot 10^{-4}$, $1 \cdot 10^{-3}\,m$.

Chapter 3

Simulation Algorithms

In this chapter we propose a Stochastic-Lagrangian framework and the derived models with the aim of simulating the steady state of the saltation process. The original idea was developed by Roberto Nuca - one of my supervisors - in the last part of his PhD research activity. The first version of the main framework already included fundamental details of the algorithm architecture, for example dynamic lists of particles, periodic boundaries and a basic impact model. However, the initial version required a lot of developments to work properly. We collaborated to develop the original model leading to the status presented in this thesis. The model is defined in order to take into account the physical aspects of saltation described in Chapter 1:

- particles are introduced from the ground in order to model the fluid entrainment;
- trajectories of particles are computed taking into account gravity and aerodynamic forces;
- the grain-bed impact dynamics and the ejection of particles is described by means of a stochastic approach in order to consider the random shapes of particles.

Furthermore, during the model development I derived two sub-models. Each of them follows the evolution of the number of particles in the system, which is the most representative quantity of the saltation process. They have been designed to study the effects of the impact and fluid entrainment models in the evolution of the number of particles in the saltation simulations.

3.1 The Saltation Model

The proposed model simulates the saltation process studying the evolution of particle positions and velocities in time. The loss of particles due to impacts or the addition of new particles due to the effect of impacts or wind action are considered. Once the steady state is reached and the simulation is stopped, the velocities and positions of sand particles are used to obtain information on the saltation process such as the concentration profile of particles with respect to the vertical direction or the horizontal mass flux. The output information of simulation will be discussed in Chapter 5.
Essentially, the simulation algorithm proceeds in time steps integrating the equation of motion for each particle, checking at each time step if an impact (on the ground or eventually with other particles) occurs or if new particles are entrained by the wind. The particle states, which are their positions and velocities, are updated at each step. The algorithm can be easily adapted to different impact models or different fluid entrainment models in order to study their effect.
The two fundamental assumptions underlying the algorithm are the following:

i) the fluid flow is described as the sum of a mean flow and turbulence fluctuations;

ii) the grain-bed interaction (i.e. the impact event) is simulated by using an impact model as described in Chapter 1, without directly simulating the impact between particles as in a DEM approach. This allows the stochastic behaviour of grain-bed interaction to be taken into account.

Let us now describe the general simulation algorithm, which is presented in Algorithm 1. Next, it will be discussed how the various aspects involved in saltation process have been dealt with. Due to its importance in saltation, the impact model is discussed separately in Chapter 4.
At the beginning of the algorithm all deterministic and stochastic properties of our physics as well as temporal and domain properties and model parameters are defined. The system starts with a number N_0 of particles that are introduced into the computational domain. The positions of these particles are randomly chosen and they are allowed to fall freely from rest. The algorithm starts its time loop until the final time T_{final}. The time step Δt of the algorithm corresponds to the time step chosen for integrating the particle equation of motion. For each time loop, four sequential steps are executed. The general scheme of simulation is reported in Figure 3.1.

i) **Input step:** A check is made as to whether particles are entrained into the system by the wind action. The way in which the fluid entrainment is simulated will be discussed later.

ii) **Predictor step:** The system state at the previous step is used to integrate for each particle the equation of motion (2.1) presented in Chapter 2. The new positions and velocities of particles are computed without taking into account grain-bed collisions or eventually mid-air collisions with other particles. They represent candidate for the new positions and velocities of particles.

iii) **Impact step:** New positions and velocities of particles are used to evaluate grain-bed collisions. In case of an impact occurs, the impact model is used to evaluate the number of ejected particles and their velocity as well as the condition of the rebounding particle. The position of the new particles is chosen equal to the position of the impact particle before the predictor step. The error made in using this assumption is marginal compared to the random behaviour of the impact dynamics.
In order to reduce computational costs and modelling assumptions, we neglect the mid-air particle collisions. As described in Chapter 1, their role is still debated. However particle-particle impacts can be incorporated during the impact step.

iv) **Corrector step:** The positions and velocities of new particles are used as initial conditions to integrate the equation of motion. The integration is repeated for ejected particles in order to obtain new compatible positions. Since information of the rebounding particle are considered as outputs of our impact model, impact particles are removed from simulation.

3.1.1 Wind Flow

As pointed out in Chapter 1, the way in which the wind flow is solved during the saltation process is an important feature of Lagrangian models. Typically Lagrangian models are coupled with Eulerian solvers for the fluid phase - since the involved flow is turbulent, turbulence models are tipically used, as done by Huang et al. 2020, W. Zhang, Y. Wang, et al. 2007 and B. Li et al. 2012.
In our model the fluid flow is imposed as a known function at each point. It is expressed by the sum of the mean flow (that is not necessarily steady) and a fluctuation term to model turbulence fluctuations. In this approach, that is also used by J. Kok et al. 2009, the fluid velocity $\vec{u}_f$ is written as:

$$\vec{u}_f = \vec{U}_f + \vec{u}'_f$$

where $\vec{U}_f$ is the mean velocity of the flow and $\vec{u}'_f$ is the turbulence fluctuation.
This approach has the advantage of avoiding the need to satisfy the divergence free constraint. In fact, random perturbations are applied pointwise without directly solving the Navier-Stokes equations. This approach reduces computational costs.
Lacking robust information on turbulence fluctuations experienced by saltating particles, we neglect the effect of turbulence, then

$$\vec{u}'_f = 0$$

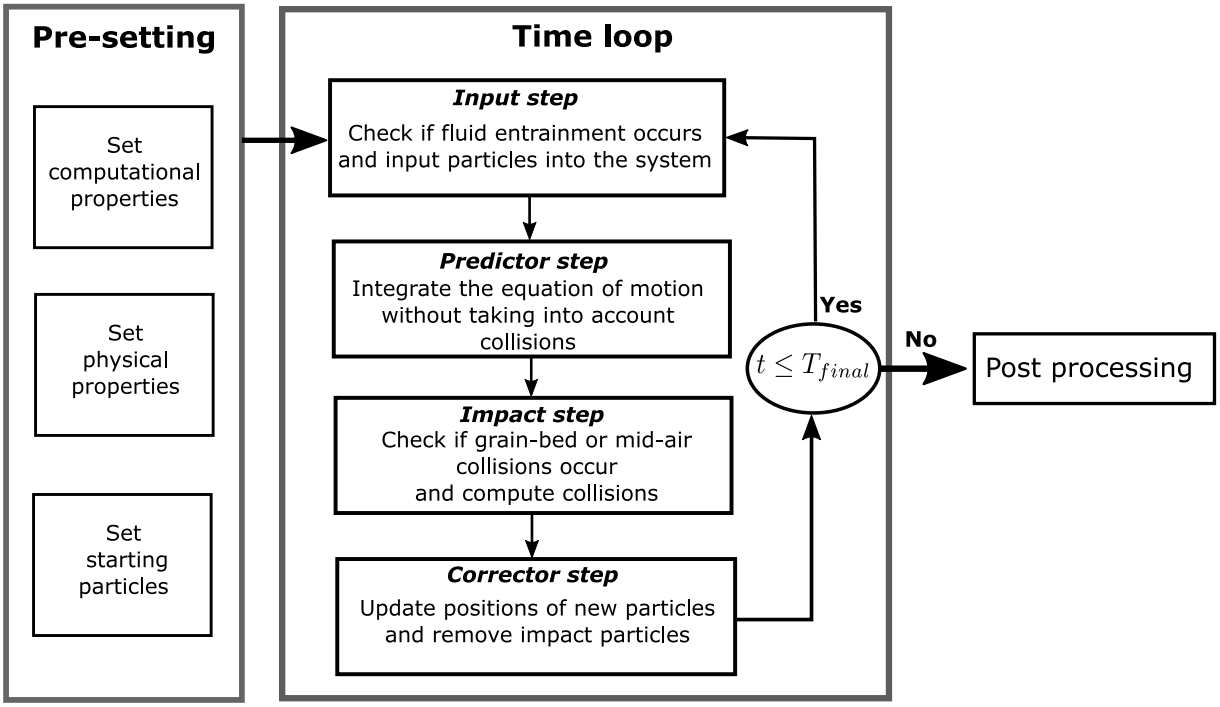

Figure 3.1: General scheme of Algorithm 1.

The wind profile corresponds to the mean wind velocity profile. The mean flow has to be divergence free. In the case of simple domains it can be analytically defined, or it can be extrapolated by pure CFD simulations. We assume horizontal and unidirectional flow and we impose the logarithmic law of the wall (1.13) for the mean wind velocity profile. At the current state of model development we neglect the feedback of saltating particles on the wind flow.

3.1.2 Sand Particles

To describe the saltation process, sand particles are divided into *active particles* in mid-air and *passive particles* at rest on the ground. Each of the passive particles has its own computational degrees of freedom and this fact involves the use of computational resources to keep them in the simulation. Models that use a DEM approach have to keep passive particles into simulation in order to compute the impact between particles.
Since our model does not solve directly the collision, there is no need to keep passive particles in the simulation. Any time the particle remains on the ground after impact it is absorbed by the boundary and it is no longer considered. However, this approach does not allow to observe changes in particle size distribution on the ground during saltation, as well as changes in the shape of the ground, though it could be easily monitored.
The distribution of particle diameters is then set at the beginning and it does not change during simulation. As we shall see, this diameter distribution is used any time a new particle is entrained into the system, by both the impact model and the fluid entrainment model. In our simulations we consider two different diameter distributions (see Figure 3.2):

- the Dirac delta distribution i.e. a single diameter for all particles. It corresponds to the so called *monodisperse case*;
- the truncated normal distribution. It is typically considered in experiments because the sand sample results from sieving (see for example Figure 3.3). The case in which a spectrum of diameters is considered is referred to *polidisperse case*.

For each sand particles the equation of motion (2.1) introduced in Chapter 2 is solved. Since the rotational dynamics is neglected, particles are considered to be point-like and characterised only by their equivalent diameter d.

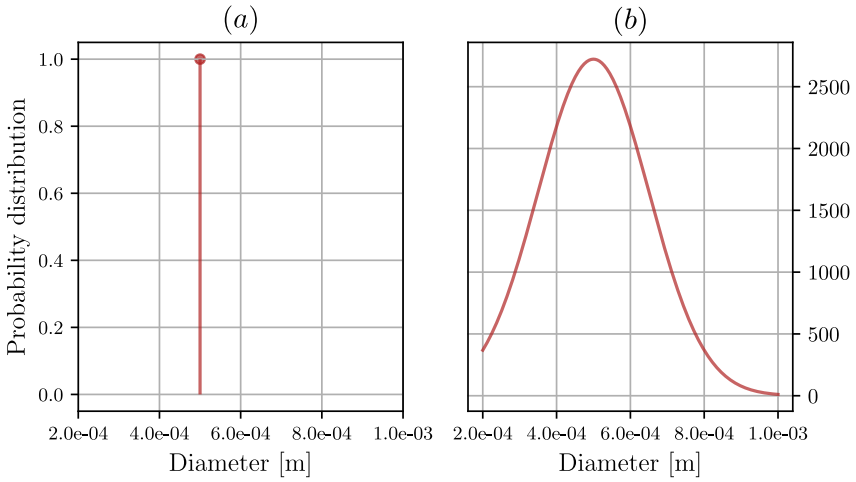

Figure 3.2: Diameter distributions used in simulations: (a) Dirac delta distribution (*monodisperse case*); (b) truncated normal distribution (*polidisperse case*).

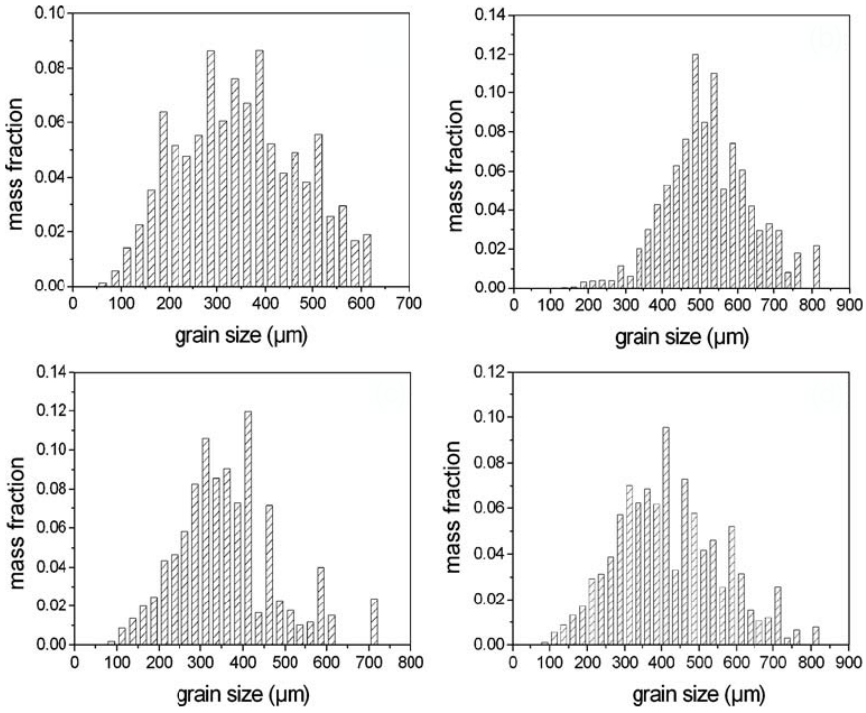

Figure 3.3: Diameter distributions in four different experimental setup in wind tunnel, from Xing 2007.

3.1.3 Computational Domain

The simulation domain is a box of dimension $L_x \times L_y \times L_z$. Periodic boundary conditions are imposed on the vertical walls in order to obtain statistical description of saltation. The box dimension has to be large enough to enclose a large number of particles. Anyway the box must also be little enough to avoid scale problems.
The periodicity of particle trajectories is obtained by the $mod(\cdot)$ function, i.e. the reminder of division, which is applied at the end of each time step to the x and y coordinates of all the

particles:

$$\begin{cases} x_k = mod\left(\dfrac{x_k}{L_x}\right) \\ \\ y_k = mod\left(\dfrac{y_k}{L_y}\right) \end{cases} \quad \text{for} \quad k = 1,2,...,N \tag{3.1}$$

where N is the number of particles into the simulation (see Figure 3.4).

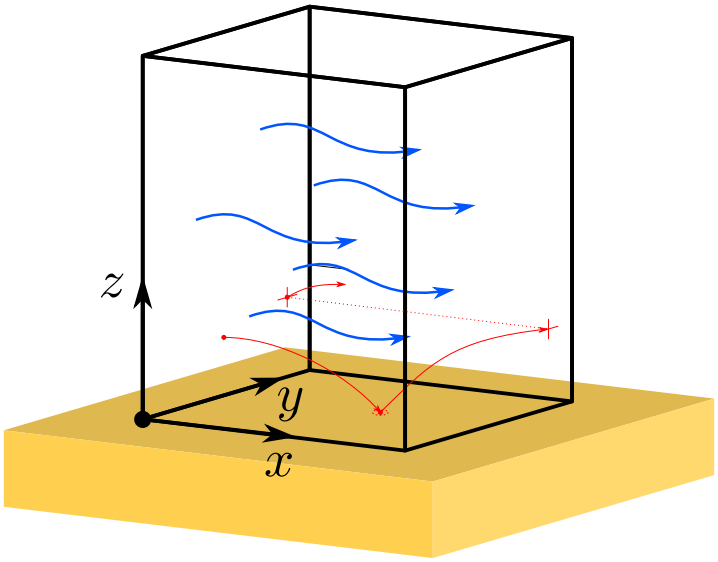

Figure 3.4: The computational domain considered in simulations. The cross shows the application of periodicity conditions on vertical walls of the box.

The sand bed surface can be expressed by the graph of a continuous and periodic function f_{bed} in order to preserve the periodicity of the box:

$$\begin{aligned} f_{bed} : [0, L_x] \times [0, L_y] &\mapsto \mathbb{R} \\ (x, y) &\mapsto \mathbb{R} \end{aligned} \tag{3.2}$$

As already mentioned, the sand bed is composed by sand particles arranged into random geometries. We approximate the sand bed as a smooth function, that can be thought as the mean surface which follows the geometries of particles. The grain-ben collision detection during the *impact step* can then be obtained verifying the following:

$$z_k \leq f_{bed}(x_k, y_k) \quad \text{for} \quad k = 1, ..., N \tag{3.3}$$

At the current state of model development a flat surface for the sand bed is imposed that means $f_{bed} \equiv 0$. The grain-bed collision detection reduces to:

$$z_k \leq 0 \quad \text{for} \quad k = 1, ..., N$$

3.1.4 Impact Model

Different impact models are discussed in detail in Chapter 4. The impact model is used to evaluate the number of ejected particles and their velocities and diameters as well as the condition of the rebounding particle. As previously said, they are based on stochastic approaches to account for the random behaviour observed in grain-bed impact dynamics. The impact models proposed are based on:

i) the impact energy e_0;

ii) the angles θ_0, φ_0 as defined in Chapter 2.

The velocity and the mass of the impact particle are then used to compute inputs of the impact model (see Chapter 2, Eq. (2.4)). Similarly the outputs of the impact model are:

i) the number N_{ej} of ejected particles, in which the rebounding particle is also included;

ii) the ejection energies e_1 of the new ejected particles;

iii) the angles θ_1 and φ_1 of the new ejected particles;

iv) the diameters d of the new ejected particles;

v) the energy e_1^{reb} and angles θ_1^{reb}, φ_1^{reb} of the rebounding particle.

Outputs of the impact model are converted to velocities (see Chapter 2, Eq. (2.3)).

3.1.5 Fluid Entrainment Model

The steady state of saltation can be seen as a balance between an input flux of particles into the system and an output flux of particles due to the loss of particles during impacts. The introduction of particles into the system can have different origins:

i) the entrainment of particles due to impact events i.e. the *impact entrainment* described by the impact model;

ii) the entrainment of particles due to the wind action, i.e. the *fluid entrainment*.

In order to account for the fluid entrainment, we introduce a flux of particles p_{wind} from the ground which is based on experimental observations:

- at the beginning, if $u^* \geq u^*_{th}$ the wind shear stress is strong enough to mobilize ground particles;
- during the steady state of saltation process impact events are more efficient in transferring momentum to the ground particles at rest;
- once the steady state is reached, the high concentration of particles to the ground will lead a great number of particles to settle back to the soil after wind entrainment due to mid-air collisions. This reduces the effect of fluid entrainment.

The flux of particles is expressed as particles per unit time and area that are introduced into the system. Following the previous observations, the flux of particles depends on the concentration of particles on the ground ϕ_{ground} and it decreases as the concentration of particles increases. We have chosen the following formula:

$$p_{wind}(\phi_{ground}) =: P\, e^{-\phi_{ground}/\phi_0} \tag{3.4}$$

where ϕ_{ground} is expressed as the volume concentration of particles close to the ground, ϕ_0 is a nondimensional coefficient and P has dimensions $[m^{-2}s^{-1}]$.
The number of particles is then obtained multiplying p_{wind} by the ground area of the box $A_{ground} =: L_x \times L_y$ and the time step Δt considered:

$$N_{input}(\phi_{ground}) = \lfloor p_{wind}(\phi_{ground})\, A_{ground}\, \Delta t \rfloor$$

In order to reduce computational errors, the time step Δt used to integrate the equation of motion (2.1) can be so small that there are very few or no particles entrained into the system at each step. In order to avoid this effect, a bigger time step $\Delta t_{input} \geq \Delta t$ for input flux is considered. The number of particles N_{input} entrained into the system is then computed as:

$$N_{input}(\phi_{ground}) = \lfloor p_{wind}(\phi_{ground})\, A_{ground}\, \Delta t_{input} \rfloor \tag{3.5}$$

Since the algorithm proceeds in time by Δt, during the *input step* a check is made as to whether the next input time falls within that step (see Figure 3.5). If an immission occurs, N_{input} particles computed from (3.5) are input into the system.

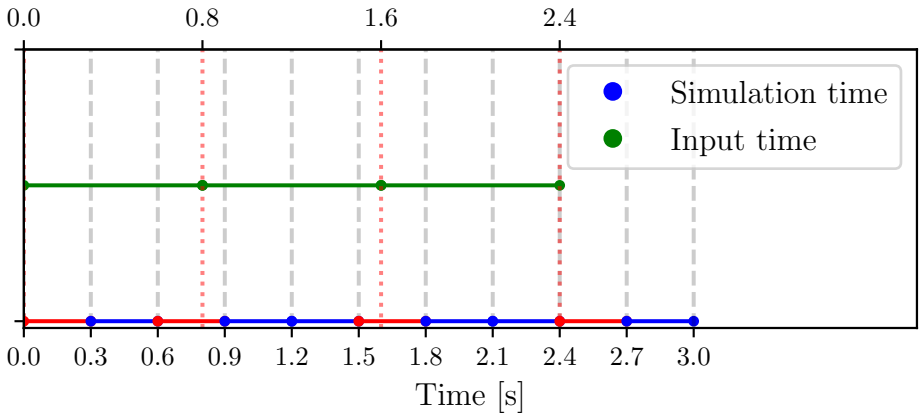

Figure 3.5: Scheme of fluid entrainment times. The final time T_{final} is set to $3\,s$, the integration time (blue line) proceeds with a time step of $\Delta t = 0.3$ and the input time (green line) with a time step of $\Delta t_{input} = 0.8$. In red are highlighted the steps in which a fluid entrainment event occurs.

Once the number N_{input} is chosen, the diameters, positions and ejection conditions of new particles must be specified:

i) the positions is chosen randomly on the sand bed;

ii) the diameter of particles is sampled using the diameter distribution on the ground;

iii) following the idea of the impact model, the initial condition of particles are defined by choosing the ejection energy e_1 and angles θ_1 and φ_1.

The energy and angles of particles entrained by the wind could be eventually defined statistically by experiments. In the lack of these data, we have chosen a uniform distribution for e_1, θ_1 and φ_1 over a fixed interval:

$$\begin{aligned} e_1 &\sim U(5 \cdot 10^{-8}\, J, 5 \cdot 10^{-7}\, J) \\ \theta_1 &\sim U(30°, 80°) \\ \varphi_1 &\sim U(-80°, 80°) \end{aligned} \tag{3.6}$$

These information are then converted into velocities by relations introduced in Chapter 2 (see Eq. (2.3)).

Algorithm 1: Saltation system

```
set temporal and domain properties;
set wind properties;
set sand properties;
set properties of impact model and fluid entrainment model;
set a number of initial particles N_0 and set their positions and
  diameters;
t = 0;
while t ≤ T_final do
    save the state of the system for post-processing routines;
    Input step :if fluid entrainment occurs then
        compute the ground concentration φ_ground of particles;
        compute the number of new particles N_input;
        set energies e_1, angles θ_1, φ_1, diameters and positions of new
          particles;
        convert input information into velocities;
        add the new particles to the system;
    end
    calculate forces on particles;
    Predictor step : compute new positions and new velocities if no
      collisions occur;
    Impact step : for particle p in the system do
        if p is involved in a mid-air collision then
            treatment of binary collision (neglected);
        else if p is involved in a ground collision then
            compute kinetic energy e_0 and angles θ_0, φ_0 of impact particle;
            impact model : compute energies e_1, angles θ_1, φ_1 and diameters of
              ejected particles and rebounding particle;
            convert outputs of impact model into new velocities;
            set particles positions;
    end
    Corrector step : compute corrections for positions of new particles;
    add the new particles to the system;
    remove impact particles;
    update the state of particles;
    t = t + Δt;
end
compute post-processing routines;
```

3.2 Additional Algorithms

In this section two further simulation algorithms are proposed. They was derived during the development of the model described by the Algorithm 1. These algorithms was designed in order to highlight the effect of impact and fluid entrainment models in the growth of particles number N, which is the only state variable considered. Each of them represents a simplyfied description of the saltation process. This leads to a reduction of computational cost. For ease of reading, in next sections the distinction between new ejected particles and the rebounding particles introduced by the impact model is neglected: all particles are referred to as ejected particles.
The following algorithms are based on these assumptions:

i) the logarithmic profile (1.13) for describing the mean flow is imposed, neglecting turbulence fluctuations;

ii) the computational domain corresponds to a flat bed;

iii) the particles trajectories are computed by Eq. (2.1) then only drag and gravitational forces are taken into account and the rotational dynamics is neglected;

iv) the diameter distribution is chosen at the beginning of the algorithms and it does not change;

v) feedback of particles on wind flow is not considered;

vi) the mid-air collisions are not taken into account.

Since the following algorithms focus on the number of particles of the system, and the wind and ground conditions are homogeneous, the spatial variable is not explicitly considered. The equation of motion (2.1) is solved in order to link the ejection information $(e_1, \theta_1, \varphi_1)$ of particles to their impact information $(e_0, \theta_0, \varphi_0)$ used in the impact model. For this reason, the trajectory database introduced in Chapter 2 could be used in future improvements.

3.2.1 Genealogy Tree Algorithm

The following algorithm is designed in order to study the role of the impact model in the growth of particles number during the simulation of saltation. The impact model together with the energy transfer from wind to particles govern the increase of particle number N within the simulation. In Chapter 2 we identified a region of initial conditions $(e_1, \theta_1, \varphi_1)$ for which particles gain energy from the mean wind flow. If the impact model is such that an ejected particle can gain enough energy then it will entrain other particles and N grows. Conversely, if the ejected particles does not gain sufficient energy, then the number of particles rapidly decays. Further, the impact model identifies the number of ejected particles with respect to impact energy. Globally, it controls the *reproductive capacity* of particles, i.e. the number of entrained particles as a result of their impacts.
Following this idea, the process can be described as a *genealogy tree* in which all the particles of a generation will give rise to the particles of the next generation due to their impacts. The number of particles $N(g)$ for each generation g is the state variable of the system. The algorithm was designed to study whether the chosen impact model could lead to uncontrolled growth of particles.
This process of particle generation can be described through the combination of trajectory function and impact model as introduced in Chapter 2. The ejection information $(e_1, \theta_1, \varphi_1)$ and diameter d are converted into inputs of the impact model $(e_0, \theta_0, \varphi_0)$ solving the trajectory equation (2.1):

$$(e_0, \theta_0, \varphi_0) = \mathcal{T}_{(d,u^*,z_0)}(e_1, \theta_1, \varphi_1)$$

The impact information $(e_0, \theta_0, \varphi_0)$ are then converted by the impact model into new N_{ej} particles added to the next generation, each of them with its own ejection information and diameter d (see Figure 3.6). The algorithm proceeds by generation. It ignores that different particles of the same

generation could impact on the ground at different times. Each particle is characterised by an ejection information $(e_1, \theta_1, \varphi_1)$ and a diameter d.

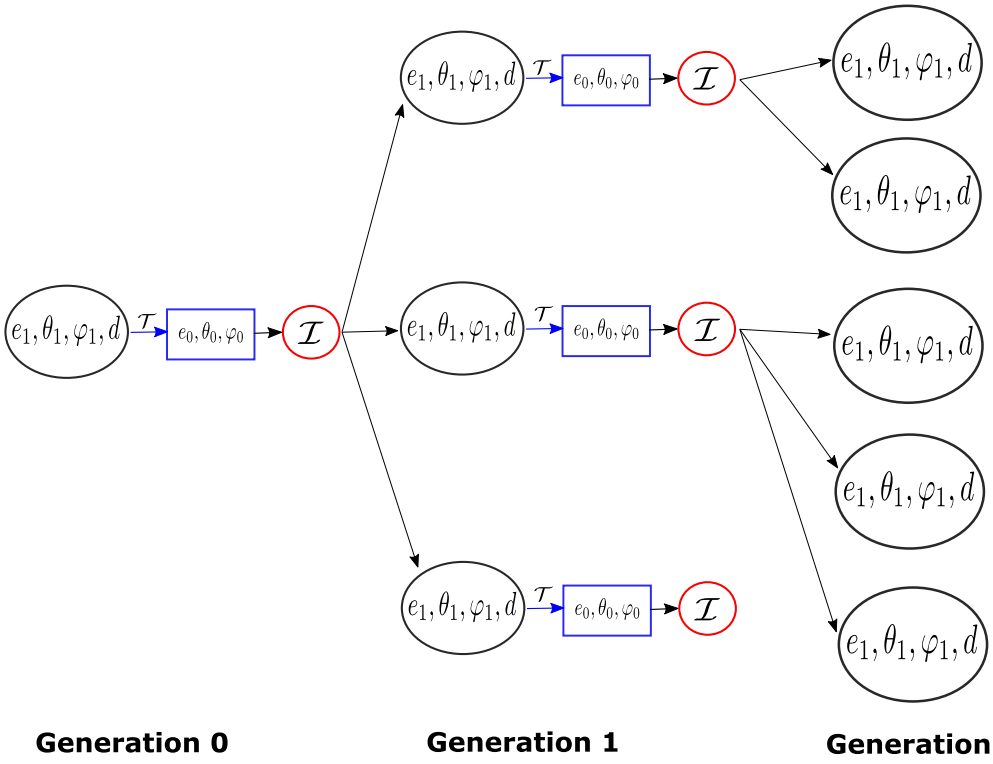

Figure 3.6: Scheme of the *genealogy tree* described by Algorithm 2. The trajectory function is identified by $\mathcal{T}$ while the impact model is identified by $\mathcal{I}$.

The simulation algorithm is presented in Algorithm 2. Simulation starts with a number $N(0)$ of particles, called *ancestors*, whose ejection information $(e_1, \theta_1, \varphi_1)$ and diameters d are chosen at the beginning. The simulation continues until the system is nonempty or the maximum number of generations G_{max} is reached.

Algorithm 2: Genealogy tree

```
set physical quantities;
set properties of impact model;
system initialization: N(0) particles are introduced and then
  {(e_1, θ_1, φ_1)_i}_{i=1}^{N(0)} and {d_i}_{i=1}^{N(0)} are saved;
g = 0;
while g <= G_max and N(g) > 0 do
    for each particle of generation g do
        compute the impact information (e_0, θ_0, φ_0) using the trajectory
         equation;
        compute the impact model: new ejection information (e_1, θ_1, φ_1) and
         diameter d for each ejected particles are saved for the next
         generation;
    end
    update particles of the next generation;
    g = g + 1;
end
compute post-processing routines;
```

3.2.2 Discrete Event Simulation of the Saltation Process

The following algorithm is designed in order to study the temporal evolution of the number of particles during the saltation process. The number of particles N does not change continuously in time but it can change following the occurence of two types of event:

- *impact event*: the particle-bed impact can produce the rebound of the impacting particle, the ejection of new particles or the loss of the impacting particle;
- *fluid entrainment event*: it corresponds to the input of a particle due to the wind action, which trigger new particles that are at rest on the ground.

The state variable N does not change unless one of the previous events occurs. In this section we propose a Discrete Event Simulation (DES) in which simulation time jumps directly to the occurence time of the next event - this approach is also called *next-event time progression*. All the future events are listed in a *pending events list* and they are characterised by a lifetime. It corresponds to the time step between their scheduling and their occurence. They are sorted according to the occurrence order: at each step the event with the shortest lifetime is chosen as the next event and its lifetime becomes the next time step of simulation. The clock goes on, following the occurence of events. After the next time step is chosen as just described, the event is computed and lifetimes of all the pending events are updated. The way in which new events are scheduled follows a specific rule that depends on the event. Let us describe in detail the way in which the events presented before are handled.

Impact Event Both the previous events entrain new particles. Each particle of the system corresponds to an impact event, because all saltating particles will impact on the ground sooner or later. Then, all the ejection information $(e_1, \theta_1, \varphi_1)$ and diameter d that characterise new particles are converted into impact information $(e_0, \theta_0, \varphi_0)$ and impact time $\Delta\tau_0$ solving the trajectory equation. Then, new impact events are added to the pending event list.
When the impact event occurs, impact information are used to set a sequence of new energies, angles of ejection and diameters according to the impact model:

$$\{(e_1, \theta_1, \varphi_1)_i\}_{i=1}^{N_{ej}} \qquad \{d_i\}_{i=1}^{N_{ej}}$$

where N_{ej} is the number of the ejected particles. The number of particles N decreases by one - the impacting particle - and it increases by N_{ej}.

Fluid Entrainment Event Fluid entrainment event simulates the input of a single particle into the system by the wind action. We set equal to zero the probability of the entrainment by wind of two different particles at the same time. In this algorithm input events are characterized by a frequency $f_{wind}(N)$ that depends on the number of particles N. Following the experimental observations introduced for Algorithm 1, this frequency decreases as the number of particles N increases. In fact, decreasing the fluid entrainment frequency corresponds to reducing the number of particles entrained in a fixed time step. This reflects the assumptions done in Algorithm 1. However, in this algorithm the fluid entrainment model is related to the total number of particles N instead of the ground particles concentration. This is because N is the only state variable considered. The frequency chosen for our simulations is:

$$f_{wind}(N) = f_0\, e^{-N/N_\infty} \tag{3.7}$$

where f_0 is the input frequency for the empty system, while N_∞ is the characteristic value describing how the input frequency decreases with the increase in N.
When the fluid entrainment event occurs a single particle is ejected, the number of particles N increases by one and consequently a new ejection information $(e_1, \theta_1, \varphi_1)$ and diameter d is set. The ejection information are chosen according to the following:

$$\begin{aligned} e_1 &\sim U(5 \cdot 10^{-8}\, J, 5 \cdot 10^{-7}\, J) \\ \theta_1 &\sim U(30°, 80°) \\ \varphi_1 &\sim U(-80°, 80°) \end{aligned} \tag{3.8}$$

The particle diameter is sampled from the particle diameter distribution considered. After the fluid entrainment event occurs, a new event is added to the pending events list with a lifetime computed from (3.7):

$$\Delta\tau_{wind} =: \frac{1}{f_{wind}(N)}$$

The simulation algorithm is presented in Algorithm 3. The system starts with N_0 particles, each of them characterized by $(e_1, \theta_1, \varphi_1)$ and diameter d. Their ejection information are set following the fluid entrainment event rule (3.8). The simulation continue until the simulation time t is less than the final time T_{final}. The scheme of Algorithm 3 is reported in Figure 3.7.

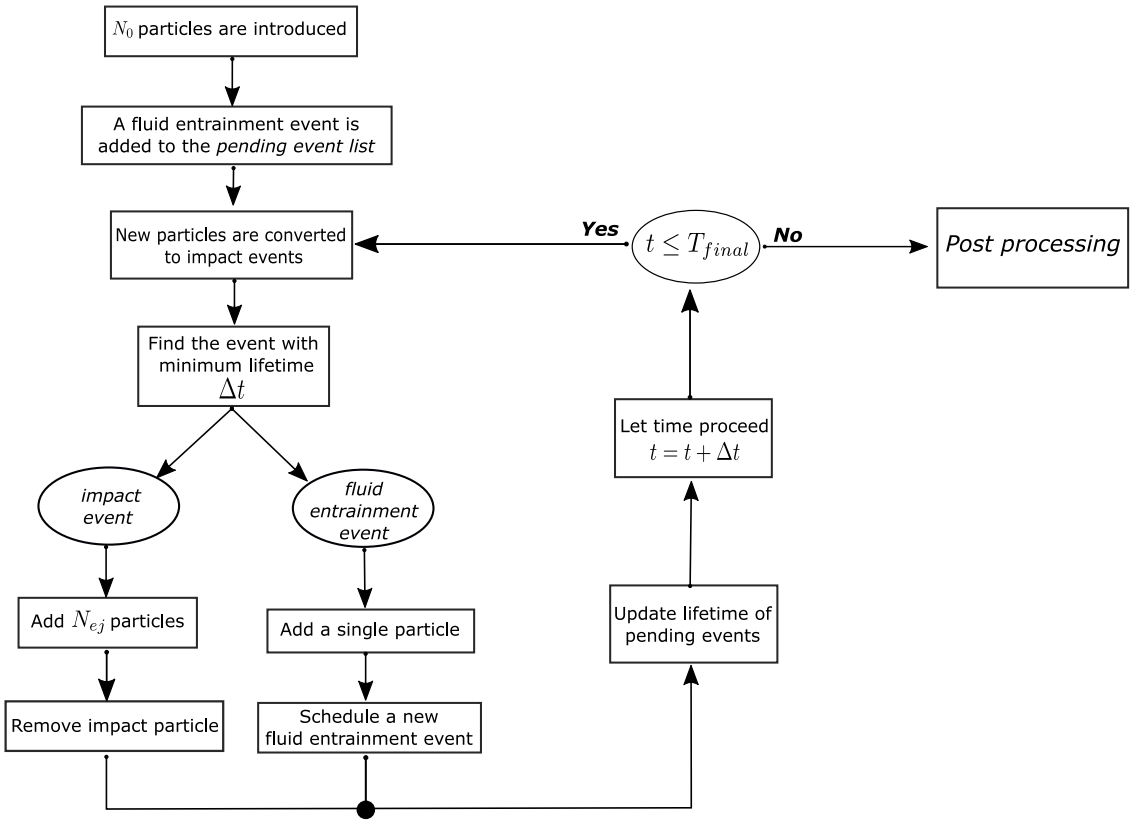

Figure 3.7: General scheme of the Algorithm 3 for the Discrete Event Simulation of saltation.

Algorithm 3: DES

set physical quantities;
set properties of impact model and fluid entrainment model;
system initialization: N_0 particles are introduced;
update state variable: $N = N_0$;
a ***fluid entrainment event*** is added to the pending event list with lifetime $\Delta\tau_{wind}$;
while $t <= T_{final}$ do
    new particles are converted to impact events;
    choose the next event i.e. the one with the shortest lifetime;
    set Δt equal to its lifetime;
    if Impact event occurs then
        compute the impact event with the minimum impact time: new N_{ej} particles are introduced;
        remove the impacting particle information;
        update the state variable: $N = N + N_{ej} - 1$;
        update the lifetime of the pending events: $\Delta\tau_0 = \Delta\tau_0 - \Delta t$ and $\Delta\tau_{wind} = \Delta\tau_{wind} - \Delta t$;
    else if Fluid entrainment event occurs then
        compute the fluid entrainment event: a single particle is introduced;
        update the state variable: $N = N + 1$;
        update the lifetime of the pending impact events: $\Delta\tau_0 = \Delta\tau_0 - \Delta t$;
        add the next fluid entrainment event to the pending events list with lifetime $\Delta\tau_{wind}$;
    $t = t + \Delta t$;
end
compute post-processing routines;

Chapter 4

Impact Models

In this chapter the treatment of grain-ben impact dyamics in the saltation models is discussed. The dissipation and ejection models presented in this chapter are obtained as developments and corrections of the original modelling framework defined by Roberto Nuca - one of my tutor - in his preliminary version of the model. We therefore derived and improved new models in the light of the results of Chapter 2.
As described in Chapter 1, impact dynamics in numerical simulations of saltation process can be obtained by the introduction of the *splash functions*. This method consists in defining the probability distributions of quantities describing the result of the impact. These quantities are typically the rebound velocity and the number and ejection velocities of newly particles entrained by impacts. The splash functions can be obtained from experiments or can be implicitly expressed by the definition of an impact model.
Impact models can be conjectured following some basic principles, for example the balance of energy or momentum during the impact (see J. Kok et al. 2009, Crassous et al. 2007, Valance et al. 2009). These models can therefore be tested by simulating the saltation process and results can be compared with experimental data, in order to assess the plausibility of the model.
In agreement with the random nature of the impact process, a stochastic approach is typically adopted (see for example J. Kok et al. 2009). In this chapter we propose different stochastic impact models.
In view of future energetic arguments the input variables of the impact models are:

i) the impact energy e_0;

ii) the impact direction, expressed by the angles θ_0 and φ_0 with respect to the normal direction to the ground and the wind direction (see Chapter 2, Figure 2.3).

Outputs are:

i) the energy e_1^{reb} and angles θ_1^{reb} and φ_1^{reb} of rebound as defined above (see Chapter 2, Figure 2.2);

ii) the energies e_1 of the new ejected particles;

iii) the angles θ_1 and φ_1 of new ejected particles;

iv) the diameters d of the new particles;

v) the number of ejected particles N_{ej}.

In the proposed impact models the rebounding particle is counted in the number N_{ej}, then the number of new ejected particles correspond to $N_{ej} - 1$.
We impose the following principle for all the impact models we propose:

if at least one particle is ejected, one of the ejected particles corresponds to the impact particle that is bouncing.

In fact, the probability that an impact particle does not rebound but it eject other particles is low (see You-Xing et al. 2019) so we decided to neglect this case.
Since the simulation of the saltation process solves the Newton equation, the impact velocity $\vec{v}_{imp}$ of the impact particle is converted into impact energy and angles by Eq. (2.4). For the same reason, since outputs of the impact model correspond to initial conditions for ejected particles, the outputs are converted back into velocity of ejection $\vec{v}_{ej}$ and rebound $\vec{v}_{reb}$ by Eq. (2.3).

We divide the impact model in two parts:

i) one modelling the dissipation of energy related to frictional events and called *dissipation model*;

ii) the other related to the ejection of newly particles and the rebound of the impact particle, called *ejection model*.

We call e_0^{post} the output of the dissipation model, that is the fraction of impact energy available after dissipation mechanisms. This fraction of energy is used for new ejections or for rebound of the impact particle. The output of the dissipation model is then the input of the ejetion model. This procedure conceptually follows the idea that first friction mechanisms dissipate part of the impact energy, and then the residual energy is divided among the ejected particles. Other assumptions can be adopted and the impact model can be adapted accordingly. The simulation scheme of the impact model is shown in the Figure 4.1. Different kinds of dissipation models and ejection models are proposed. None of the proposed models uses assumptions about particles shape to account for the variability of sand particles.

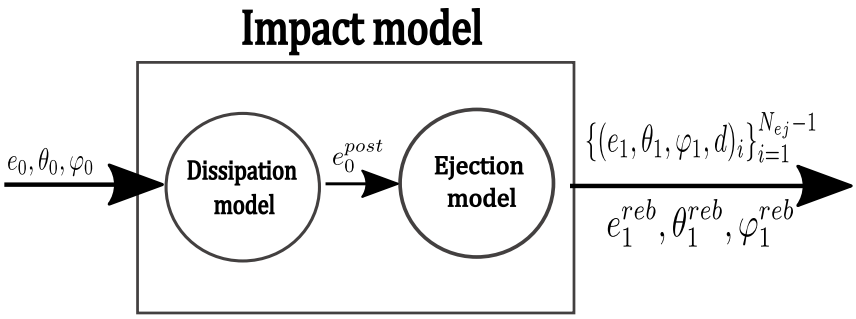

Figure 4.1: Scheme for inputs and outputs of the proposed impact models, in which its elements are highlighted: the dissipation model and the ejection model.

4.1 Dissipation Models

What we have so far called *ground* is a set of particles, each of them with a peculiar shape, possibly composed by different materials, arranged into a stochastic configuration. All these aspects affect the impact and friction mechanisms involved.
We identify the *energetic coefficient of restitution* α which can be defined as the fraction of impact energy that is preserved after impact. This fraction of energy will be then divided among all the particles that are set in motion, including the impacting particle that may eventually bounce off. Specifically if e_0^{post} is the amount of energy that is preserved after dissipation, the energetic coefficient of restituition is:

$$\alpha =: \frac{e_0^{post}}{e_0} \in [0,1) \tag{4.1}$$

because $0 \leq e_0^{post} < e_0$. Since the impact conditions are strongly random, α can be thought as a random variable possibly spanning a subinterval of [0,1) to be characterized on the basis of experiments. They can identify its probability distribution, changing energy and angles of

impact and measuring e_0^{post}. In fact, α could depend on impact conditions. In the lack of these experiments we propose two different dissipation models, which consists in defining a random distribution for α and consequently for e_0^{post}. In general, the higher the value of α is, the less energy is dissipated.

Uniform Distribution over a Fixed Interval The simplest assumption that can be made is the uniform distribution among two different values:

$$\alpha \sim U(\alpha_{inf}, \alpha_{sup}) \tag{4.2}$$

where $0 \leq \alpha_{inf} < \alpha_{sup} < 1$ are constants. This dissipation model will be referred to as Dissipation Model 1.

Dependence on Energy and Angle of Impact From phenomenological observations it can be concluded that:

- vertical impacts ($\theta_0 \simeq 0$) produce more dissipation than quasi-horizontal impacts ($\theta_0 \simeq \frac{\pi}{2}$);
- for high-energy impacts the available energy could be enough to eject other particles even in case of dissipation, so e_0^{post} should be greater for high-energy impacts.

In order to take the previous observations into account we choose α_{inf} and α_{sup} in (4.2) to be dependent on e_0 and θ_0, i.e.

$$\alpha \sim U(\alpha_{inf}(e_0, \theta_0), \alpha_{sup}(e_0, \theta_0))$$

where:

$$\alpha_k(e_0, \theta_0) = \alpha_0^k \left(1 - e^{-(e_0/e_k)}\right) \sin\theta_0 \qquad k = \{inf, sup\} \tag{4.3}$$

Since we must have $\alpha_{inf} < \alpha_{sup} \, \forall e_0, \theta_0$ then parameters must satisfy the following conditions:

$$\alpha_0^{inf} < \alpha_0^{sup}, \qquad e_{inf} \geq e_{sup} \tag{4.4}$$

All these parameters are strictly positive. α_0^{inf} and α_0^{sup} are non dimensional parameters while e_{inf} and e_{sup} have dimension $[J]$. We have that for high-energy impacts

$$\alpha \in \left[\alpha_0^{inf} \sin\theta_0, \alpha_0^{sup} \sin\theta_0\right]$$

while $\alpha \simeq 0$ for low-energy impacts or for vertical impacts. The parameters e_{inf} and e_{sup} control how rapidly α_{inf} and α_{sup} reach their asymptotic values with respect to the energy of impact e_0. If we impose $e_{inf} = e_{sup} =: \bar{e}$ we have that the mean value $\overline{\alpha}$ of the energy restitution coefficient is:

$$\overline{\alpha}(e_0, \theta_0) = \left(\frac{\alpha_0^{sup} - \alpha_0^{inf}}{2}\right) \left[1 - e^{-e_0/\bar{e}}\right] \sin\theta_0 \tag{4.5}$$

Then, $\overline{\alpha}$ is greater for quasi-horizontal impacts while fixing e_0 it increases as $\bar{e}$ decreases. This dissipation model will be referred to as Dissipation Model 2. In Figure 4.2 the behaviour of α_{inf} and α_{sup} is reported with fixed values of α_0^{inf}, α_0^{sup}, e_{inf} and e_{sup}.

4.2 Ejection Models

The dissipation model identifies the fraction of energy e_0 dissipated by friction. Then, e_0^{post} is the energy available for ejection of new particles and/or the rebound of the impact particle. The ejection model has to identify the number of ejected particles and their output dynamic conditions as well as their diameter, and the rebound energy and angle of the impact particle.
The principle underlying the proposed ejection models is the conservation of energy. So the sum

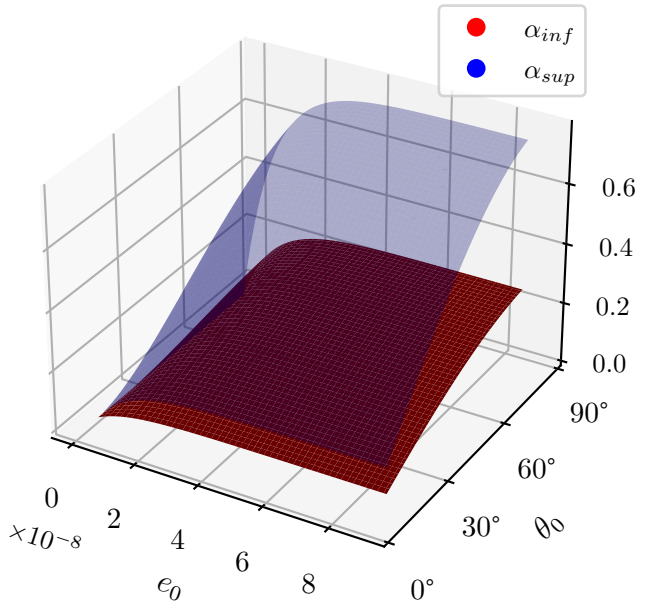

Figure 4.2: Values of α_{inf} and α_{sup} for the Dissipation Model 2, changing energy of impact e_0 and angle of impact θ_0. We set $\alpha_0^{inf} = 0.3$, $\alpha_0^{sup} = 0.8$ and $e_{inf} = e_{sup} = 1 \cdot 10^{-8}\, J$.

of energies of the ejected particles has to be less than or equal to the energy left by dissipation model, which is distributed among the ejected particles:

$$\sum_{i=1}^{N_{ej}-1} e_{1,i} + e_1^{reb} \leq e_0^{post} \tag{4.6}$$

The choice of particle diameters and angles is the same for both the ejection models we propose. They thus differ only in the choice of the number of ejected particles and their energies. We point out that the number N_{ej} of ejected particles and their energies are related. In fact, the energy e_0^{post} is divided among the ejected particles. Then, in general we have that the more particles are ejected, the lower their ejection energies e_1 are.

Particle Diameters Since the algorithms we propose does not take account of ground particles involved during impact, diameters of the newly ejected particles have to be extracted from the distribution of ground particle diameters that characterises the sand bed (see Figure 3.2 and Figure 3.3).

Ejection Angles We assume that the choice of θ_1^{reb} and φ_1^{reb} and of the ejection angles θ_1 and φ_1 of the new particles is the same.
Due to the random shape of natural sand particles, angles of ejection are strongly random. It is reasonable to assume an upper limit θ_1^{max} of θ_1 due to geometrical constraints (see Figure 4.3). Then θ_1 belongs to a subinterval of $[0°, \theta_1^{max}]$. Since transverse motion with respect to wind direction is observed in consequence of impact events (see W. Zhang, Kang, et al. 2007) non vanishing angles φ_1 are allowed. However, we decide to neglect the backward motion, because it represents a little fraction of the motion of sand particles (see LiQiang Kang et al. 2008). In order to avoid backward motion we take φ_1 in a subinterval of $[-90°, 90°]$.
Xiao et al. 2017 suggest that there is a correlation between the velocity and angle of ejection, but to the best of our knowledge this aspect is still debated. Since there is not a strong experimental

evidence, we consider ejection angles independent from each other and from the ejection velocity. In order to reduce the assumptions we take angles θ_1 and φ_1 as uniformly distributed over a fixed interval, as described in (4.7), for all the ejection models proposed. Further improvements can be made in case of accurate measurements.

$$\begin{aligned} \theta_1 &\sim U(10°, 80°) \\ \varphi_1 &\sim U(-30°, 30°) \end{aligned} \tag{4.7}$$

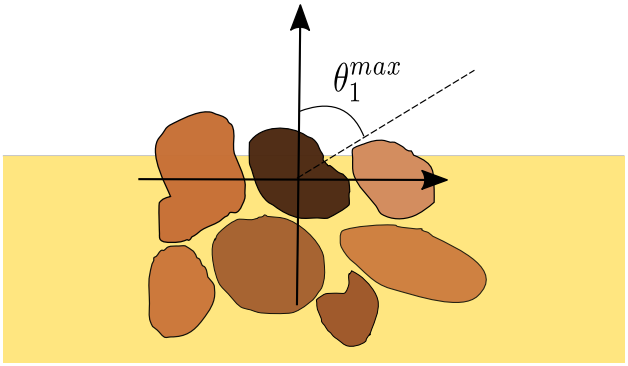

Figure 4.3: Scheme of the ejection event. Due to geometrical constraints, the ejection angle θ_1 with respect to vertical direction has to be taken lower than a maximum value θ_1^{max}.

Minimum Value of Energy All the ejection models we propose introduce an energetic threshold e_{min}, which corresponds to the minimum value of ejection energy e_1 or rebound energy e_1^{reb} that a particle has to overcome in order to be entrained into the fluid flow:

$$e_1 \geq e_{min} \qquad e_1^{reb} \geq e_{min}$$

As described in Chapter 1, windblown sand transport is a complex system in which particles are involved in different trasport modes (as *reptation*, *creep* or *saltation*). Each of them has different characteristics that could be considered separately. The mean goal of e_{min} is to select which mode of particle motion is considered (creep, reptation, saltation or all of them). In fact, particles involved in creep or reptation are characterized by low values of energy with respect to saltating particles. An increase in e_{min} corresponds to consider only high energy particles, i.e. saltating particles. Since there is no consensus in definition of each mode of motion, the parameter e_{min} can be considered as a *fitting parameter* of the ejection model, that can be identified to replicate the experimental results. The effect of parameter e_{min} in simulations will be discussed in Chapter 5.
The ejection models than could eject particles that are discarded and not entrained into the system. For this reason, the sum of energies e_1 could be less that e_0^{post} (see (4.6)). We point out that, since the energy e_0^{post} is distributed among the ejected particles, if $e_0^{post} < e_{min}$ no particles are ejected. However, even if $e_0^{post} \geq e_{min}$ no particles could be ejected by the ejection models proposed. It corresponds to the case in which all the ejected particles are involved in creep or reptation.

4.2.1 Energy Equi-Ripartition

The first model we propose is the simplest model that satisfies the energy requirements: the energy e_0^{post} left by dissipation model is divided equally among all ejected particles. Since the energy is equally divided, there is no difference in defining the energies of particles between the impact particle that rebounds and the other ejected particles. This ejection model will be referred to as Ejection Model 1.

The main aspect of this model is then to identify the number N_{ej} of ejected particles. As already mentioned the energy of each ejected particles has to overcome e_{min}. This enforces a constraint on the maximum number of particles N_{ej}^{max} that can be ejected, that is how many times the minimum value of energy e_{min} can be contained in the energy available after dissipation. We have that:

$$N_{ej}^{max} = \left\lfloor \frac{e_0^{post}}{e_{min}} \right\rfloor \tag{4.8}$$

The relation (4.8) implicitly states that if $e_0^{post} < e_{min}$ then there is no ejections. The number of ejected particles N_{ej} is chosen randomly between 0 and N_{ej}^{max}:

$$N_{ej} \in \{0,1,...,N_{ej}^{max}\}$$

For simplicity we have chosen the uniform distribution. The mean number of ejected particles is:

$$\overline{N_{ej}} = \frac{1}{2} \left\lfloor \frac{e_0^{post}}{e_{min}} \right\rfloor$$

then it is an increasing function of the ratio between the energy e_0^{post} left after dissipation and e_{min}. Let us define

$$S =: \frac{e_{min}}{e_0^{post}} \tag{4.9}$$

We point out that S is a random variable because it depends on e_0^{post}, i.e. on the dissipation model. We have that

$$N_{ej}^{max} = \left\lfloor \frac{1}{S} \right\rfloor, \qquad \overline{N_{ej}} = \frac{1}{2} \left\lfloor \frac{1}{S} \right\rfloor$$

The lower S is, the more particles are ejected on average, while if $S > 1$ no particles are ejected. We recall that the rebounding particle is counted in the number N_{ej}. If $N_{ej} = 1$ then only the rebounding particle is considered, while if $N_{ej} > 1$ other particles are ejected. For $N_{ej} \geq 1$ we have:

$$\begin{cases} e_{1,i} = \dfrac{e_0^{post}}{N_{ej}} \quad \text{for} \quad i = 1,...,N_{ej} - 1 \\ \\ e_1^{reb} = \dfrac{e_0^{post}}{N_{ej}} \end{cases} \tag{4.10}$$

4.2.2 Consecutive Extractions of Energy

Let us now focus on a single impact event. Following the idea proposed in Crassous et al. 2007 and Valance et al. 2009 we can consider the impact event as a sequence of binary collisions. The 3D structure in which ground particles are arranged could bring to ternary or high-order collisions but the simplification of binary collisions can be made.
Let us reproduce an impact dynamics. Particle A that is approaching the ground impacts on another particle B that is resting (see Figure 4.4). Once friction mechanisms dissipate part of the impact energy, the energy left will be divided between the two particles. The particle B that was at rest will receive a push downwards because of the direction of impact (see Figure 4.4), then it will collide with another particle C that is at rest. This will lead to an energy transfer and a push upwards for particle B, while C will receive a push downward with part of the energy of B. The particle C will follow the same behaviour of B, leading to a chain of binary collisional events which stops as soon as the energy is exhausted.
We can then heuristically imagine the impact event as a sequence of binary impacts, each of which transfers part of the impact energy to one of the surrounding particles.
We point out that each collision dissipates part of the impact energy due to friction mechanisms. We have encapsulated all these energy losses in the dissipation model, then in the ejection model each collision corresponds to an energy transfer of the impact energy left by the dissipation model

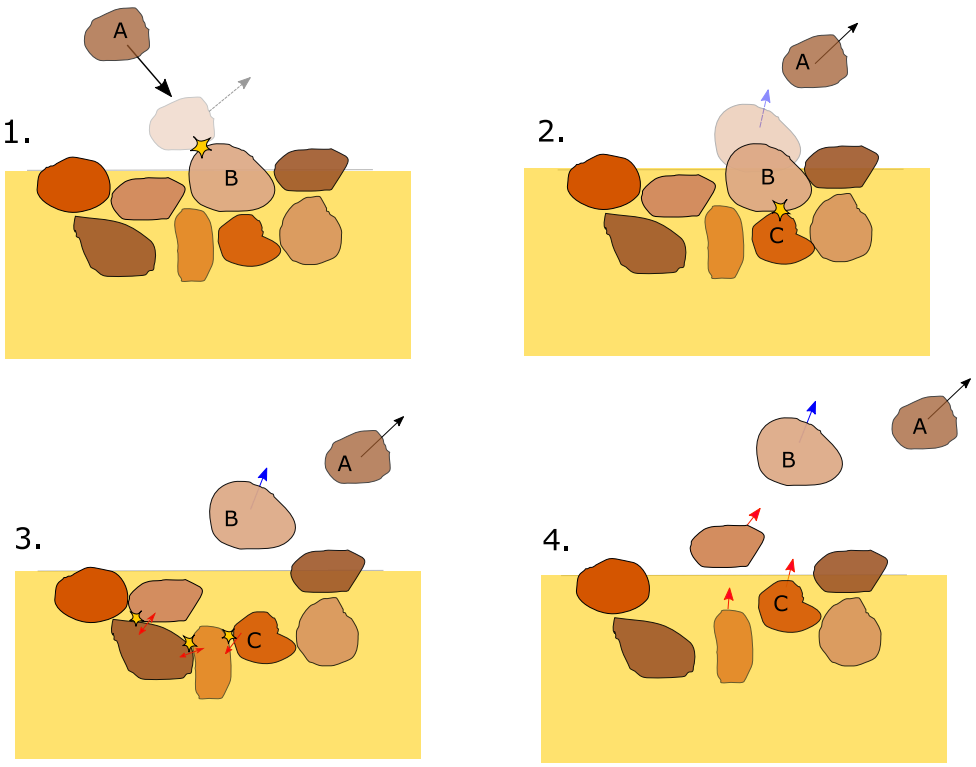

Figure 4.4: Scheme of an impact event and the sequence of binary impacts among particles. In (1.) the particle A impacts on the particle B, which impacts with particle C (2.) and the process goes on (3.) until the available energy ends and a group of particles is ejected (4.). Each of them has a different fraction of the available energy e_0^{post}.

e_0^{post}. The stochastic approach proposed to define the energies of the new ejected particles and the rebounding particle follows the idea presented above. It consists in a sequence of extractions to define the energies of particles involved into the impact process.
At each step of the sequence, a fraction of the available energy is extracted. After that, the available energy decreases according to the energy extracted. The sequence stops as soon as the available energy is less than the minimum energy e_{min}. In fact, other extractions would lead to energies smaller than e_{min} so these extractions will not corresponds to particles entrained into the system.
Let $e_{k=0}^{res} := e_0^{post}$ the energy with which the sequence starts, let E_k^{ex} be the random variable of the k-th extraction of energy and e_k^{ex} its realization. Let e_k^{res} be the residual energy after the k-th extraction. The sequence of extractions is summarized by the rule from step k to $k+1$ and by the stop condition:

i) sampling e_{k+1}^{ex} for the energy E_{k+1}^{ex} in the interval $I_k := [0, e_k^{res}]$ according to the probability distribution that characterises E_{k+1}^{ex};

ii) computing the residual energy after the $k+1$ extraction:

$$e_{k+1}^{res} := e_k^{res} - e_{k+1}^{ex} \tag{4.11}$$

Then the next interval of extraction becomes $I_{k+1} := [0, e_{k+1}^{res}]$;

iii) stopping the sequence of extraction when the residual energy is less than threshold e_{min}. So the *stop condition* is:

$$e_{k=N}^{res} < e_{min} \tag{4.12}$$

where N is the number of extractions.

We point out that if $e_0^{post} < e_{min}$ no extractions are made and then no particles are ejected, while if $e_0^{post} \geq e_{min}$ at least an extraction is made.
For the sake of simplicity we suppose that each extraction is made according to a uniform distribution over the residual energy. This will allow us to obtain theoretical results we presented below. However other probability distributions can be treated in future studies. This ejection model will be referred to as Ejection Model 2.
The $k+1$ extraction is made in the interval $[0, e_k^{res}]$ then the extracted energy e_{k+1}^{ex} could be less than e_{min}. Not all the extracted energies then correspond to ejected particles. In order to obtain the ejection energies actually considered and the number N_{ej} of ejected particles, it is necessary to check which extracted energies are greater than e_{min}. In general we will have

$$N_{ej} \leq N$$

We call $\{e_i^{ex}\}_{i=1}^{N}$ the sequence of extracted energies and $\{e_i^{ej}\}_{i=1}^{N_{ej}}$ the sequence of energies that corresponds to ejected particles. In Figure 4.5 an example of the process of extractions is shown.

Most of laboratory experiments identify the impact particle that rebounds with the particle with the maximum value of energy (see for example Beladjine et al. 2007). In order to maintain consistency with experimental observations, the maximum value of energy is associated to the rebounding particle:

$$e_1^{reb} = \max_{i=1,\dots,N_{ej}} \{e_i^{ej}\} \tag{4.13}$$

while the other energies e_i^{ej} will be associated to the other ejected particles. We point out that $e_{k=N}^{res}$ is the residual energy when sequence stops, then this fraction of energy is dispersed. The sequence of extractions is such that

$$\sum_{i=1}^{N} e_i^{ex} + e_N^{res} = e_0^{post}$$

The number of extractions N and the number of ejected particles N_{ej} are random variables. In fact, the sequence does not have a fixed length and it ends as soon as the stop condition is satisfied. Furthermore, it is not known a priori how many of these extractions are greater than e_{min}, which corresponds to N_{ej}. We can make some considerations on the range of N_{ej}.
Since the model is based on distributing energy until it is exhausted, it imposes that the lower the extracted energies are, the more extractions are made. Is it also true that an extraction which is less than the energetic threshold e_{min} will decrease the energy available without any ejection of particle. It decreases the number of ejected particles N_{ej}.
The maximum value for N_{ej} is obtained by the extractions of the minimum value of energy which corresponds to an ejected particle. The maximum number of ejected particles is then the number of times that e_{min} is contained in e_0^{post}:

$$N_{ej}^{max} = \left\lfloor \frac{e_0^{post}}{e_{min}} \right\rfloor \tag{4.14}$$

which is exactly the result obtained in the previous ejection model.
Instead, the minimum number of ejected particles is zero because each extraction could be less than e_{min}. Then we have that:

$$N_{ej} \in \{0,1,\dots,N_{ej}^{max}\}$$

4.2.3 The Sequence of Energy Extractions as a Markov Process

It is possible to describe the sequence of extractions proposed in the Ejection Model 2 as a stochastic process which responds to the Markov property as presented below. By making an appropriate reformulation, the sequence can be expressed considering the residual energy at each extraction. This will allow us to obtain the probability distribution over the number of draws performed.

We recall Eq. (4.11):

$$e_{k+1}^{res} := e_k^{res} - e_{k+1}^{ex}$$

where e_{k+1}^{ex} is the extracted energy obtained at the $k+1$ step by the uniform distribution on the interval $I_k =: [0, e_k^{res}]$. Then e_{k+1}^{res} is itself a random variable which belongs to I_k. Since we have chosen a uniform distribution for energy extractions, then also the residual energies will be characterized by the same distribution.
Let E_k^{res} be the random variable and e_k^{res} its realization. By construction of the model it is possible to define the conditional probability distribution for E_{k+1}^{res} with respect to the previous residual energy E_k^{res}:

$$f_{E_{k+1}^{res}|E_k^{res}=e_k^{res}}(e_{k+1}^{res}) = \frac{1}{e_k^{res}} \mathbf{1}_{(0,e_k^{res})}(e_{k+1}^{res}) \qquad \text{for} \quad k = 0,1,2,...,N \tag{4.15}$$

We have considered the open interval instead of the closed one in order to avoid some problems during actual computing. Since extremes of the interval are null measure sets with respect to the Lebesgue measure, the probability distribution does not change.
The sequence of energy extractions is then described by the sequence of random variables that correspond to the residual energies $\{E_k^{res}\}_{k=1}^N$ where N is the number of extractions and $E_{k=0}^{res} := e_0^{post}$ is the *starting energy* obtained by the dissipation model. We point out that it is itself a random variable. Anyway for next computing we consider e_0^{post} as a parameter. By construction each of them depends only on the previous residual energy that is:

$$f_{E_{k+1}^{res}|E_k^{res},E_{k-1}^{res},...,E_1^{res},E_0^{res}}(e_{k+1}^{res}) = f_{E_{k+1}^{res}|E_k^{res}}(e_{k+1}^{res}) \tag{4.16}$$

then the sequence of random variables can be considered as a Markov process.
By construction the sequence of realizations $\{e_k^{res}\}_{k=1}^N$ is decreasing:

$$e_{k+1}^{res} \leq e_k^{res}$$

and the sequence of extractions stops as soon as $e_N^{res} < e_{min}$.
We recall that if e_0^{post} is less than e_{min} then the extraction sequence does not start, so from now on we will suppose that $e_0^{post} \geq e_{min}$.
Numerical tests of the process is shown in Figure 4.5. The sequence of residual energies is reported in the first column of the figure. The extracted energies e_i^{ex} are then computed from (4.11) and reported in the second column of the figure, where red dots correspond to energies that do not overcome e_{min} (the green horizontal line in figure) and blue dots correspond to energies of ejected particles e_i^{ej}.

Normalization of the Extraction Process

The extraction process of the residual energies can be normalized dividing by the amount of energy available after dissipation e_0^{post}. Each extraction is then performed in (0,1) and it represents the fraction of e_0^{post} that is taken as residual energy. Let X_k be the random variable that corresponds to the k-th residual energy E_k^{res} normalized by e_0^{post}, and let x_k be its realization.
The sequence of extraction stops as soon as:

$$x_k < S =: \frac{e_{min}}{e_0^{post}}$$

where S is the *normalized* energy threshold, which correspond to the parameter defined in (4.9) for the Ejection Model 1. We will see in the following that the number of extractions depends on S. Since we have supposed before that $e_0^{post} \geq e_{min}$, from now on we take:

$$S \leq 1$$

Otherwise, no particles are ejected. The process can then be described by a sequence of random variables $\{X_k\}_{k=1}^N$ in (0,1) for which we can write the probability density f_{X_1} for X_1 and the

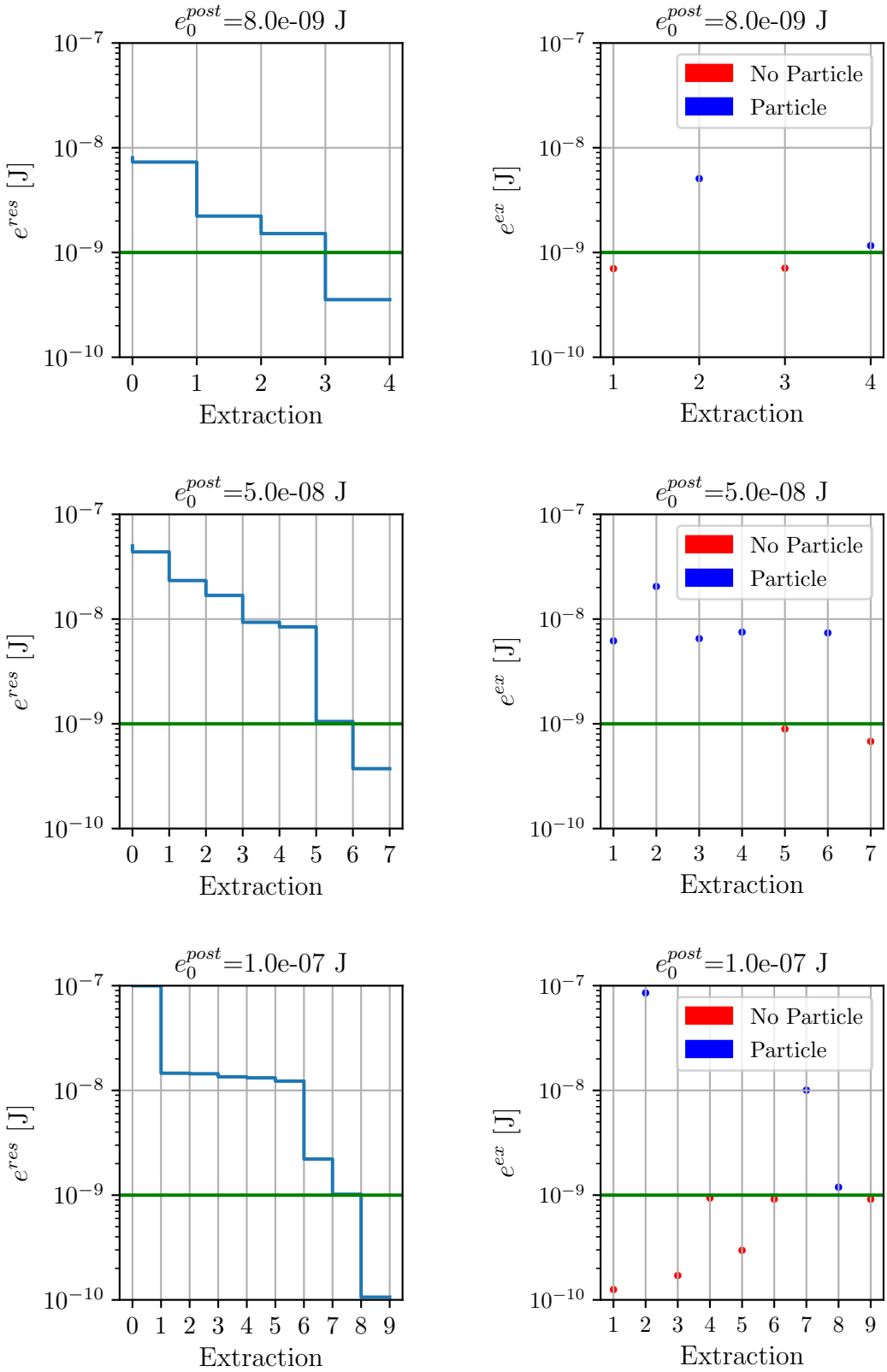

Figure 4.5: Numerical tests of the extraction process. On the left: sequence of residual energies e_k^{res}; on the right: extracted energies e_i^{ex}. (blue dots) Energies larger than the minimum energy e_{min} (the green horizontal line) which correspond to ejection energies e_i^{ej}; (red dots) energies that are less than e_{min}. The value e_{min} is set to $1 \cdot 10^{-9}\, J$ while different values of e_0^{post} are chosen.

conditional probability density $f_{X_k|X_{k-1}=x_{k-1}}$ of the generic X_k respect to X_{k-1} (it follows from Eq. (4.15)):

$$f_{X_1}(x_1) = \mathbf{1}_{(0,1)}(x_1) \tag{4.17}$$
$$f_{X_k|X_{k-1}=x_{k-1}}(x_k) = \frac{1}{x_{k-1}}\mathbf{1}_{(0,x_{k-1})}(x_k) \quad \text{for} \quad k = 2,3,...,N$$

Theoretical results have been obtained for the probability distribution of each extraction X_k and for the number N of extractions that can be made. The number of ejected particles N_{ej} will be shown by numerical tests.

Probability Density for X_k

The construction of the model imposes that only the conditional probability density function of each variable X_k with respect to X_{k-1} is known (see Eq. (4.17)). Let us now compute the probability density function f_{X_k} for the generic random variable X_k.
Let us recall that the joint probability distribution $f_{X,Y}$ of two random variables X and Y can be obtained by the conditional probability distribution of one of them with respect to the other by the formula:

$$f_{X,Y}(x,y) = f_{X|Y}(x)f_Y(y) \tag{4.18}$$

We can then write the joint probability distribution of $X_1,...,X_i$ using recursively the formula (4.18):

$$f_{X_1,X_2,...,X_i}(x_1,x_2,...,x_i) = f_{X_i|X_{i-1},X_{i-2},...,X_1}(x_i)f_{X_{i-1},X_{i-2},...,X_1}(x_{i-1},x_{i-2},...,x_1) =$$

$$= f_{X_i|X_{i-1},X_{i-2},...,X_1}(x_i)f_{X_{i-1}|X_{i-2},X_{i-3},...,X_1}(x_{i-1})f_{X_{i-2},X_{i-3},...,X_1}(x_{i-2},x_{i-3},...,x_1)$$

and so on, making a factorization of the joint probability density function for $X_1,...,X_i$.
By using Eq. (4.16) we have that each random variable only depends on the previous one, then the joint probability density can be easily obtained for the first i extractions. In fact, the previous factorization becomes:

$$f_{X_1,X_2,...,X_i}(x_1,x_2,...,x_i) = f_{X_1}(x_1)f_{X_2|X_1}(x_2)f_{X_3|X_2}(x_3)...f_{X_i|X_{i-1}}(x_i)$$

and then by Eq. (4.17) we have

$$f_{X_1,X_2,...,X_i}(x_1,x_2,...,x_i) = \mathbf{1}_{(0,1)}(x_1)\frac{1}{x_1}\mathbf{1}_{(0,x_1)}(x_2)\frac{1}{x_2}\mathbf{1}_{(0,x_2)}(x_3)...\frac{1}{x_{i-1}}\mathbf{1}_{(0,x_{i-1})}(x_i)$$

that can be written in the compact form as:

$$f_{X_1,X_2,...,X_i}(x_1,x_2,...,x_i) = \frac{1}{\prod_{h=1}^{i-1}x_h}\mathbf{1}_{(0,1)\times(0,x_1)\times...\times(0,x_{i-1})}(x_1,x_2,...,x_i) \tag{4.19}$$

The probability density function for X_i can be computed by integrating the joint probability density (4.19) for $x_1,...,x_{i-1}$. By construction the probability density of X_i will depend only on X_{i-1} then it is possible to compute sequentially the probability density functions of X_i for $i = 2,3,...$ using (4.18) as described below.
For X_2 we have that:

$$f_{X_2}(x_2) = \int_0^1 f_{X_1,X_2}(x_1,x_2)\,dx_1 = \int_0^1 \frac{1}{x_1}\mathbf{1}_{(0,1)\times(0,x_1)}(x_1,x_2)\,dx_1 \tag{4.20}$$

The integration domain is identified by:

$$\begin{cases} 0 < x_1 < 1 \\ 0 < x_2 < x_1 \end{cases}$$

Since we integrate with respect to x_1 the integration domain can be expressed by

$$\begin{cases} 0 < x_2 < 1 \\ x_2 < x_1 < 1 \end{cases}$$

Thus we can write (4.20) as:

$$f_{X_2}(x_2) = \int_{x_2}^{1} \frac{1}{x_1} \mathbf{1}_{(0,1)}(x_2)\, dx_1 = -\ln x_2 \mathbf{1}_{(0,1)}(x_2)$$

For X_3 we have that:

$$f_{X_3}(x_3) = \int_0^1 f_{X_2,X_3}(x_2, x_3)\, dx_2 = \int_0^1 f_{X_2}(x_2) f_{X_3|X_2}(x_3)\, dx_2 =$$
$$= \int_0^1 -\frac{\ln x_2}{x_2} \mathbf{1}_{(0,1)\times(0,x_2)}(x_2, x_3)\, dx_2$$

Again the integration domain can be expressed with respect to x_3:

$$\begin{cases} 0 < x_2 < 1 \\ 0 < x_3 < x_2 \end{cases} \longrightarrow \begin{cases} 0 < x_3 < 1 \\ x_3 < x_2 < 1 \end{cases}$$

Thus we have:

$$f_{X_3}(x_3) = \int_0^1 -\frac{\ln x_2}{x_2} \mathbf{1}_{(0,1)\times(0,x_2)}(x_2, x_3)\, dx_2 =$$
$$= \int_{x_3}^1 -\frac{\ln x_2}{x_2} \mathbf{1}_{(0,1)}(x_3)\, dx_2 = \frac{\ln^2 x_3}{2} \mathbf{1}_{(0,1)}(x_3)$$

Let us now suppose that the probability density function of the random variable X_i is the following:

$$f_{X_i}(x_i) = (-1)^{i-1} \frac{\ln^{i-1} x_i}{(i-1)!} \mathbf{1}_{(0,1)}(x_i) \tag{4.21}$$

We know that the random variable X_{i+1} depends on X_i according to Eq. (4.17). Following the procedure introduced above for X_2 and X_3 we can compute the probability density function for X_{i+1}:

$$f_{X_{i+1}}(x_{i+1}) = \int_0^1 \frac{1}{x_i} (-1)^{i-1} \frac{\ln^{i-1} x_i}{(i-1)!} \mathbf{1}_{(0,1)\times(0,x_i)}(x_i, x_{i+1})\, dx_i =$$

$$= \frac{(-1)^{i-1}}{(i-1)!} \int_{x_{i+1}}^1 \frac{\ln^{i-1} x_i}{x_i} \mathbf{1}_{(0,1)}(x_{i+1})\, dx_i =$$

$$= \frac{(-1)^{i-1}}{(i-1)!} \frac{(-1)}{i} \ln^i x_{i+1} \mathbf{1}_{(0,1)}(x_{i+1}) =$$

$$= \frac{(-1)^i}{i!} \ln^i x_{i+1} \mathbf{1}_{(0,1)}(x_{i+1})$$

then by using the mathematical induction principle we obtain the probability density function for the random variable X_i of the sequence, which is defined by Eq. (4.21).
We can see from the probability density function of X_i that the probability to sample small value of x_i increases as i increases, because the available normalized energy decreases as the number of extractions increases. In Figure 4.6 the numerical test is compared with theoretical results. The value of threshold S is set to a small value in order to obtain a sufficient number of sampling (as we will see in the next section, the number of extractions depends on S), and the number of tests is set to 10000. We compare results for X_1, X_2, X_3 because for the other variables the number of sampling decrease and numerical tests do not provide good results.

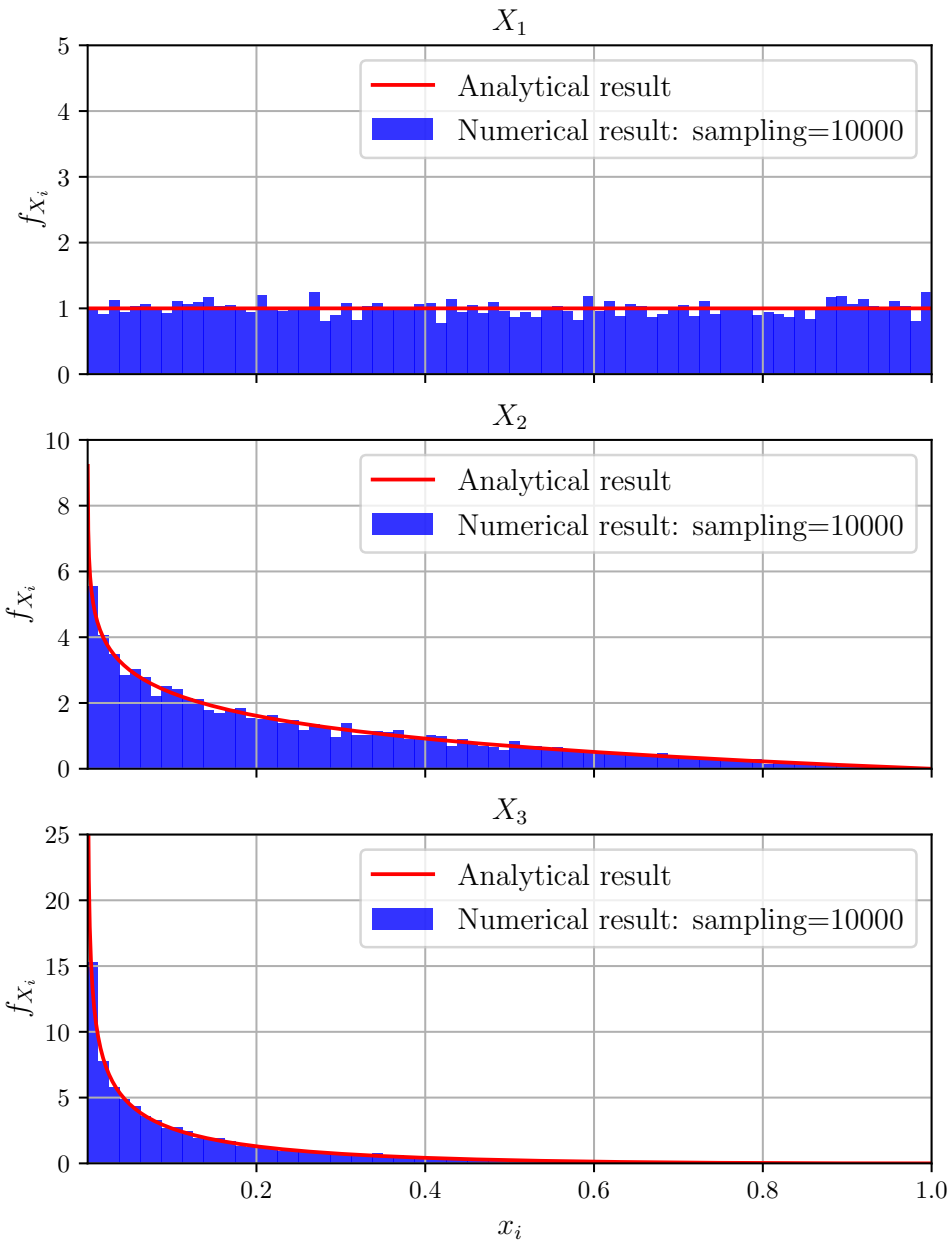

Figure 4.6: Comparison between numerical and theoretical results for the probability density function of the k-th normalized residual energy X_k, k = 1,2,3. The histogram plots of the numerical results over 10000 tests are reported.

Number of Extractions

It is possible to obtain the probability distribution of the number of extractions using the joint probability distribution (4.19). We know that the sequence of extractions stops as soon as the stop condition is satisfied. Let us call N the stochastic variable that corresponds to the number of extractions and let n be its realization. The probability that $N = n$ corresponds to the probability that $X_i \geq S$ for all $i = 1, ..., n-1$ and that $X_n < S$ so:

$$\mathbb{P}(N = n) = \mathbb{P}(X_1 \geq S, X_2 \geq S, ..., X_n < S) \tag{4.22}$$

For $n = 1$ we have that

$$\mathbb{P}(N = 1) = \mathbb{P}(X_1 < S) = \int_0^S \mathbf{1}_{(0,1)}(x_1)\, dx_1 = S$$

thus we have that if $S = 1$ a single extraction is made.
For $n = 2$ defining $\Omega_2 =: \{x_1 \geq S, x_2 < S\}$, we have that:

$$\mathbb{P}(N = 2) = \mathbb{P}(X_1 \geq S, X_2 < S) = \iint_{\Omega_2} f_{X_1,X_2}(x_1, x_2)\, dx_1\, dx_2 =$$

$$= \iint_{\Omega_2} \frac{1}{x_1} \mathbf{1}_{(0,1)\times(0,x_1)}(x_1, x_2)\, dx_1\, dx_2$$

The integration domain becomes:

$$\begin{cases} 0 < x_1 < 1 \\ 0 < x_2 < x_1 \\ S \leq x_1 < 1 \\ 0 \leq x_2 < S \end{cases} \longrightarrow \begin{cases} S \leq x_1 < 1 \\ 0 < x_2 \leq S \end{cases}$$

Then we have:

$$\mathbb{P}(N = 2) = \iint_{\Omega_2} \frac{1}{x_1} \mathbf{1}_{(0,1)\times(0,x_1)}(x_1, x_2)\, dx_1\, dx_2 = \int_S^1 \int_0^S \frac{1}{x_1}\, dx_1\, dx_2 = -S \ln S$$

For $n = 3$ defining $\Omega_3 =: \{x_1 \geq S, x_2 \geq S, x_3 < S\}$, we have that:

$$\mathbb{P}(N = 3) = \mathbb{P}(X_1 \geq S, X_2 \geq S, X_3 < S) = \iiint_{\Omega_3} f_{X_1,X_2,X_3}(x_1, x_2, x_3)\, dx_1\, dx_2\, dx_3 =$$

$$= \iiint_{\Omega_3} \frac{1}{x_1 x_2} \mathbf{1}_{(0,1)\times(0,x_1)\times(0,x_2)}(x_1, x_2, x_3)\, dx_1\, dx_2\, dx_3$$

The integration domain becomes:

$$\begin{cases} 0 < x_1 < 1 \\ 0 < x_2 < x_1 \\ 0 < x_3 < x_2 \\ S \leq x_1 < 1 \\ S \leq x_2 < 1 \\ 0 < x_3 < S \end{cases} \longrightarrow \begin{cases} S \leq x_1 < 1 \\ S \leq x_2 < x_1 \\ 0 < x_3 < S \end{cases}$$

Thus we have that:

$$\mathbb{P}(N = 3) = \iiint_{\Omega_3} \frac{1}{x_1 x_2} \mathbf{1}_{(0,1)\times(0,x_1)\times(0,x_2)}(x_1, x_2, x_3)\, dx_1\, dx_2\, dx_3 =$$

$$= \int_S^1 \int_S^{x_1} \int_0^S \frac{1}{x_1 x_2}\, dx_1\, dx_2\, dx_3 = S\frac{\ln^2 S}{2}$$

Following this procedure for a generic n we obtain the probability of the number of extractions N:

$$\mathbb{P}(N = n) = (-1)^{n-1} S \frac{\ln^{n-1} S}{(n-1)!} \quad \text{for} \quad n = 1,2,... \tag{4.23}$$

In Figure 4.7 the numerical test is compared with theoretical results for different values of S. We compute 10000 tests of extraction. Results of 10000 tests changing S are shown in Figure 4.8.

The smaller the value of the parameter S is, which is the ratio between e_{min} and e_0^{post}, the greater is the number of extractions N on average. This corresponds to say that the greater the energy e_0^{post} left after dissipation or the smaller e_{min} is, the greater the number of extractions is on average.

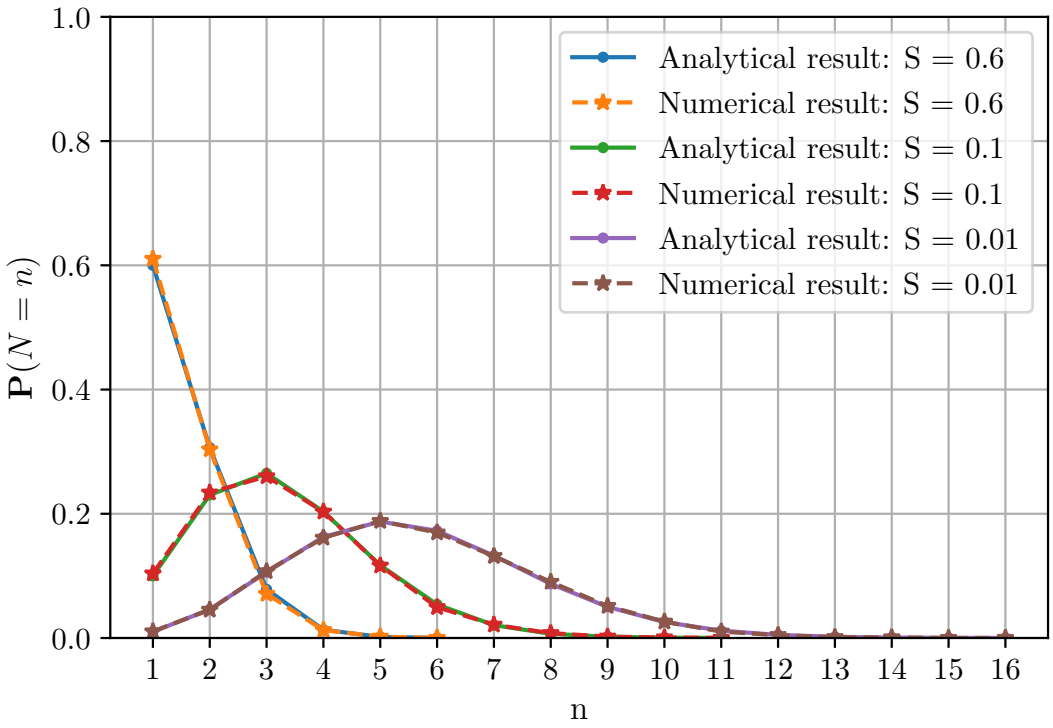

Figure 4.7: Comparison between numerical (dotted lines) and theoretical (full lines) results on the number of extractions for 10000 tests. Numerical results correspond to the ratio between the number of tests in which n extractions are computed and the total number of tests. Results for different values of S are shown.

Number of Ejections

As we already said the number of extractions N does not correspond to the number of ejected particles N_{ej}. From the sequence of realization $\{x_k\}_{k=1}^{N}$ for normalized residual energies it is possible to obtain the *normalized* energies extracted for particles from Eq. (4.11). The number of particles that are input into the system N_{ej} and their energies can be obtained checking which of these energies exceed the normalized value of threshold S.
Numerical tests are made in order to obtain the probability density of N_{ej} changing the value of S. Results of 10000 test are shown in Figure 4.9. As we have already mentioned the number of ejections N_{ej} belongs to $\{0,1,...,N_{ej}^{max}\}$ where

$$N_{ej}^{max} = \left\lfloor \frac{1}{S} \right\rfloor$$

As we can see the numerical tests respect this result. In fact, for values of S between 0.6 and 0.9 we have that $N_{ej}^{max} = 1$ and this is shown in Figure 4.9-(a). We can also see that for small values of S the maximum number of ejected particles obtained by numerical tests is less than the theoretical one. Results for N_{ej}^{max}, the most likely value of N_{ej} and the mean value $\overline{N_{ej}}$ obtained by tests are reported in Table 4.1. In Figure 4.10 the mean number of ejections obtained from numerical tests is reported as plot with respect to S.
As for the number of extractions, the smaller the value of the parameter S is, the greater the number of ejections N_{ej} is on average. This corresponds to say that the greater the energy e_0^{post} left after dissipation or the smaller e_{min} is, the greater the number of ejected particles is on average. Further, we recall that the rebounding particle is counted in N_{ej} then for $0.5 \leq S \leq 1$ we have only the rebound particle (see Figure 4.9) while for $S < 0.5$ the impact could eject other particles.

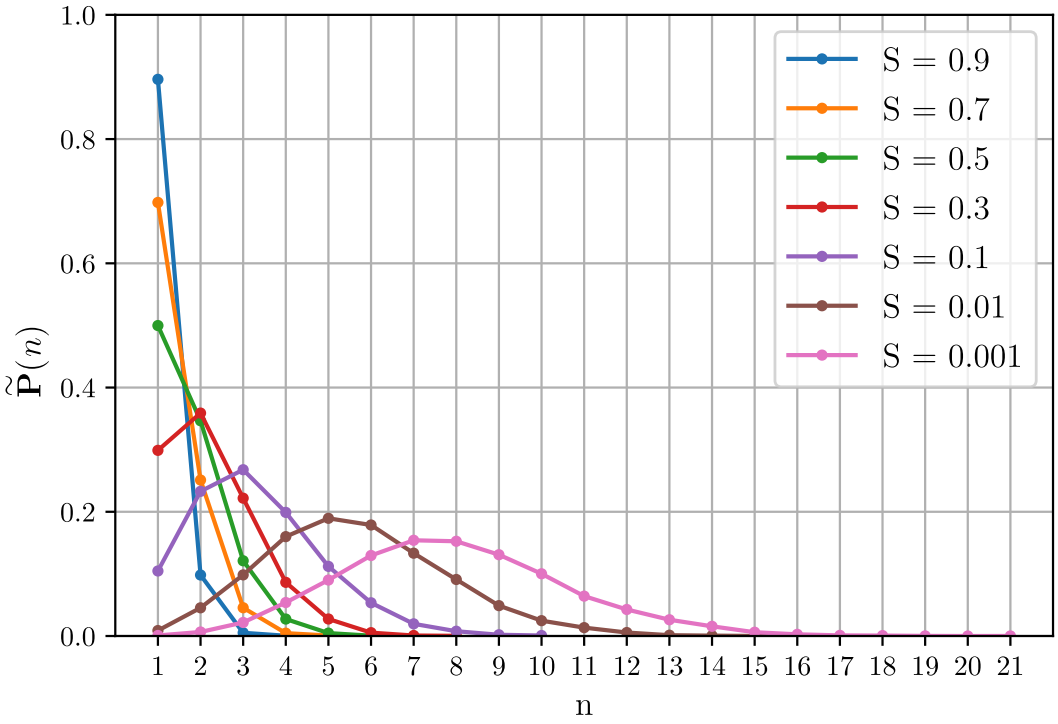

Figure 4.8: Numerical results of the number of extractions for 10000 tests. The figure shows the ratio between the number of tests in which n extractions are performed and the total number of tests, referred to as $\tilde{\mathbf{P}}(n)$. Results for different values of S are shown.

S	Theoretical N_{ej}^{max}	Numerical N_{ej}^{max}	Most likely value	Mean value $\overline{N_{ej}}$
0.9	1	1	0	0.11
0.8	1	1	0	0.22
0.7	1	1	0	0.36
0.6	1	1	1	0.51
0.5	2	1	1	0.69
0.4	2	2	1	0.91
0.3	3	3	1	1.20
0.2	4	4	1	1.61
0.1	10	6	2	2.31
0.01	100	12	4	4.61
0.001	1000	19	7	6.89

Table 4.1: Comparison between the theoretical maximum number of ejected particles N_{ej}^{max} and the one obtained by numerical tests. The most likely value and mean value $\overline{N_{ej}}$ obtained by numerical tests are also reported.

4.2.4 The Parameters of the Ejection Models

The common parameters of both the ejection models are S and e_{min}.

- In both the ejection models the number of ejected particles N_{ej} depends on

$$S =: \frac{e_{min}}{e_0^{post}} = \frac{e_{min}}{\alpha e_0}$$

  i) The maximum number of ejected particles N_{ej}^{max} increases as S decreases. We have

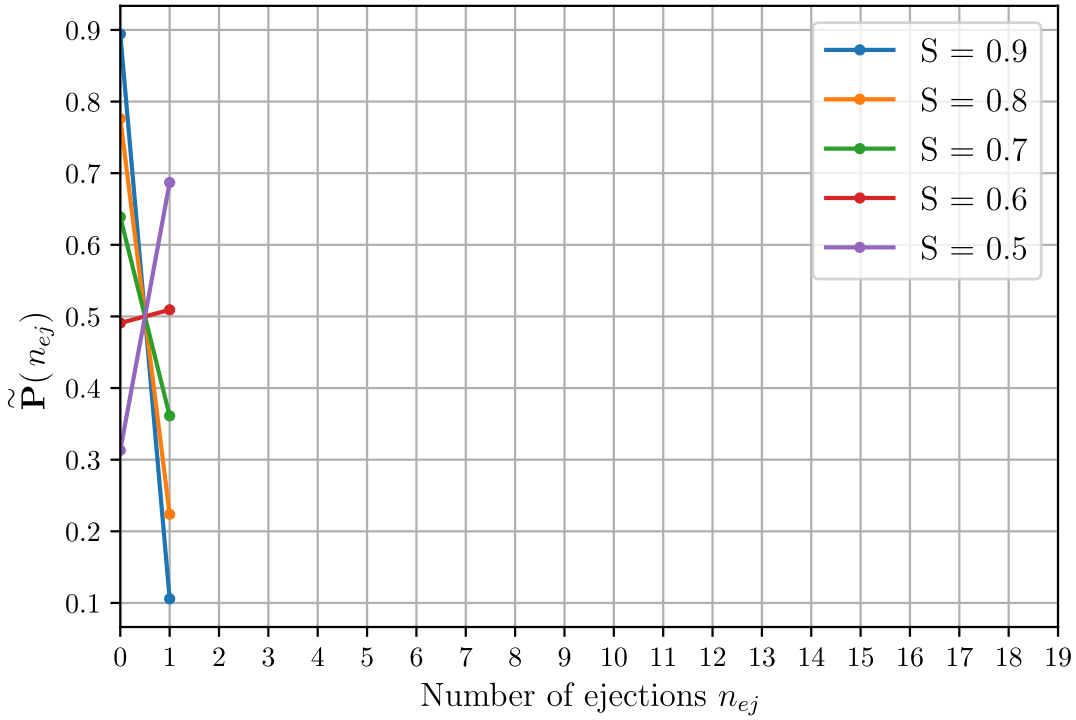

(a)

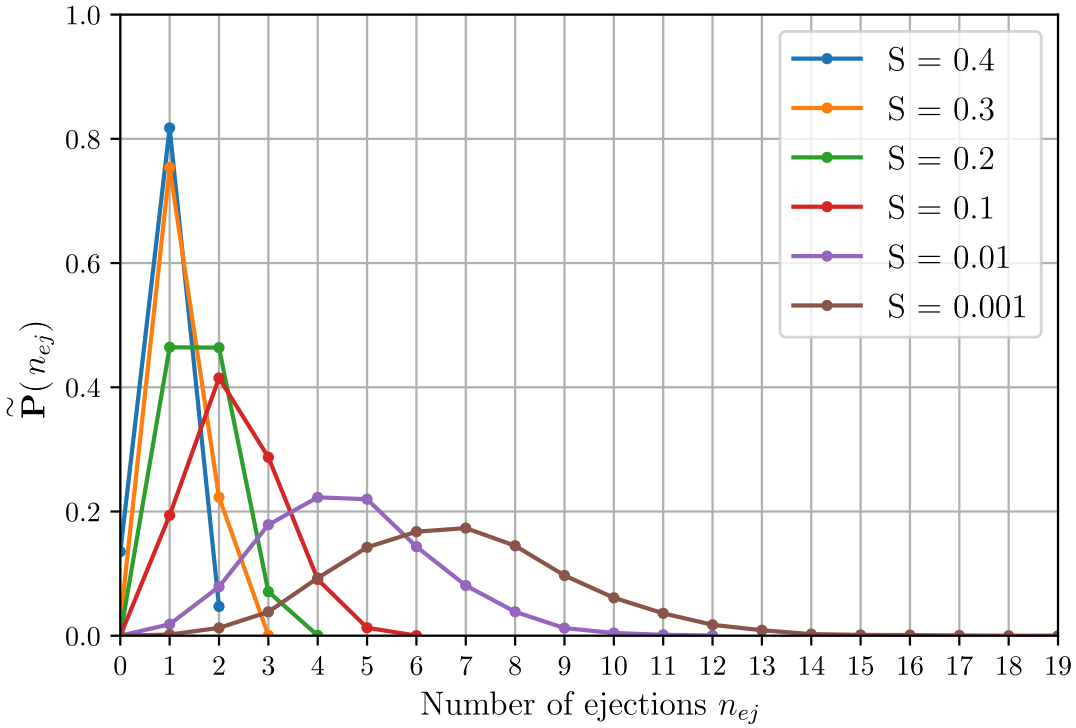

(b)

Figure 4.9: Numerical results of the number of ejected particles for 10000 tests. The figure shows the ratio between the number of test in which n_{ej} ejections are computed and the total number of tests, referred to as $\tilde{\mathbf{P}}(n_{ej})$. Results for different values of S are shown: (a) $S \in [0.5,0.9]$; (b) $S \in [0,0.4]$.

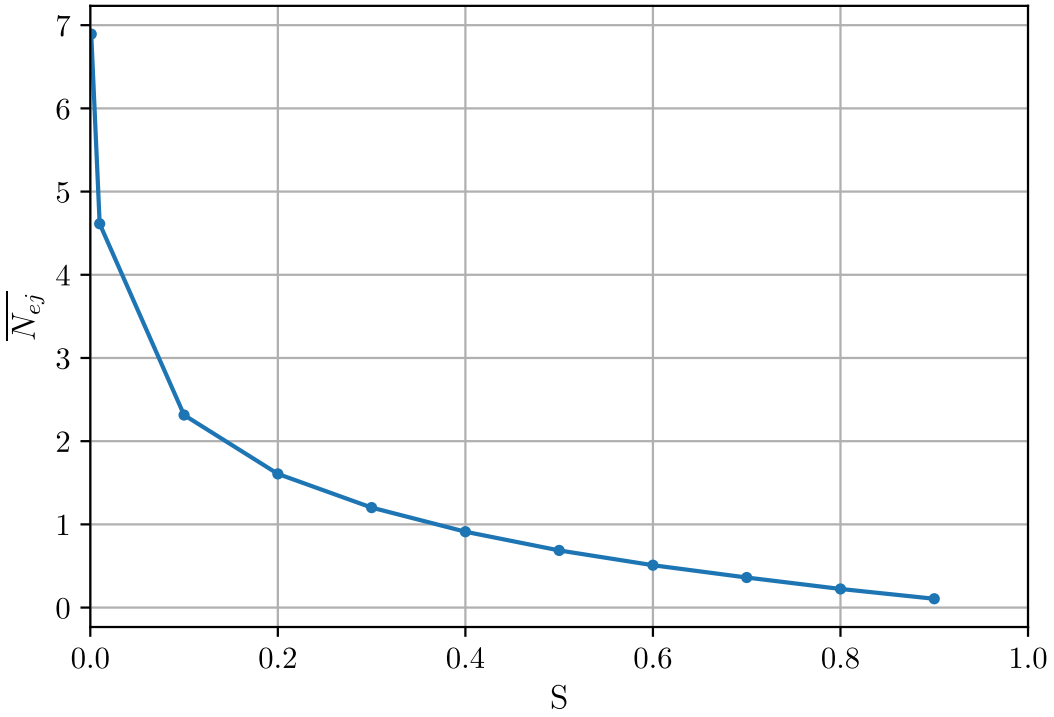

Figure 4.10: Numerical results for the mean number $\overline{N_{ej}}$ of ejected particles for 10000 tests. Results for different values of S are shown.

that:

$$N_{ej}^{max} = \left\lfloor \frac{1}{S} \right\rfloor$$

ii) For $S > 1$ no particles are ejected.

iii) The mean value $\overline{N_{ej}}$ increases as S decreases.

In general, the higher the impact energy e_0 is, the lower S is. For a fix value of impact energy, the value of S depends both on dissipation model and e_{min}:

- the greater α is, i.e. the lower the energy dissipation is, the lower S is and the more particles are ejected;
- the greater e_{min} is, the higher S is and the fewer particles are ejected.

The parameter S then controls the *impact entrainment* of particles, which is greater for small values of S. It is itself a random variable which depends on the dissipation model, i.e. on α.

- the parameter e_{min} controls the energy of ejected particles: the greater e_{min} is, the greater the energy of ejected particles is. The ejection energy of particles is related to geometric characteristics of trajectories (see Chapter 2) then an increase of e_{min} allow to avoid *creep* or *reptation* of particles, that are characterized by low ejection energies.

The effect of changes in impact models parameters will be shown by numerical tests of Algorithms 1, 2 and 3 in Chapter 5.

Chapter 5

Simulation of the Saltation Process

This chapter is devoted to the presentation of results of numerical tests. They are carried out by changing the parameters of the impact or fluid entrainment models as well as the particle size and wind flow parameters, in order to study their effects on the system.
To observe the evolution of the system, the following data are collected during the simulation time on the basis of Algorithm 1 explained in Chapter 3:

i) the number of active particles;

ii) the kinetic and potential energy of the system, i.e. the sum of kinetic and potential energies of all the active particles;

iii) the number of particles entering the flow by the fluid entrainment model;

iv) the number of entrained particles due to impacts;

v) the total number of particles entering the flow, due both to impacts or wind action;

vi) the total number of particles that stop on the ground and exit from the system.

In steady state conditions the number of particles as well as the kinetic and potential energies reach a steady mean value. The number of new particles entrained due to impacts and wind action show the role of impact and fluid entrainment models in sustaining the process, while the total number of newly and escaping particles show whether the system balances.

As soon as the system reaches the steady state, different sampling of particles position and velocities are collected in order to obtain information on the saltation process. We compute 100 sampling starting from $t = 1\,s$. Positions and velocities of particles up to a distance of $20\,cm$ from the ground are collected, and then divided into 20 groups according to the height, i.e. we divide the computational box into 20 slices. For each slice we compute:

i) the particles concentration $\phi(z)$ (see Figure 5.2);

ii) the mean and standard deviation of particles velocities components $v_x(z)$, $v_y(z)$ and $v_z(z)$ (see Figure 5.4);

iii) the mean and standard deviation of velocity magnitude of particles (see Figure 5.3);

iv) the mean and standard deviation of particle diameters in case of polidisperse case (see Figure 5.15);

v) the horizontal mass flux $q(z)$ (see Figure 5.2), computed as:

$$q(z) =: \rho_s \phi(z) \overline{v_x}(z)$$

5.1 Simulations in the Monodisperse Case

Different numerical tests have been performed in order to understand the behaviour of the system when parameters change. Table 5.1 refers to the *standard setup* considered in the following numerical tests. Individual changes were then made to parameters in order to observe their effects. All the simulations are performed in a box of dimension $0.05 \times 0.05 \times 1\, m$ with $T_{final} = 3\, s$, $\Delta t = 1 \cdot 10^{-3}\, s$, $\Delta t_{input} = 5 \cdot 10^{-3}\, s$ and $N_0 = 100$. The equation of motion is solved with the use of the Newmark method (see Newmark 1959). The particles concentration near of the ground ϕ_{ground} used in the fluid entrainment model is computed within $1\, cm$ from the ground. Numerical tests performed with Algorithm 2 and 3 suggest that the Ejection Model 1 causes too many particles to be emitted at each impact, creating an excessive fluctuation in the number of particles in the system (see Figure 5.22). For this reason the Ejection Model 2 is used in the following numerical tests.

$\rho_a\, [kg/m^3]$	1.225
$\rho_s\, [kg/m^3]$	2700
$u^*\, [m/s]$	0.5
$z_0\, [m]$	0.001
Number of initial particles	100
Particles diameter $[m]$	$5 \cdot 10^{-4}$
Diameter distribution	Dirac delta
Dissipation model	Model 1
Interval of α	[0.2,0.7]
Ejection model	Model 2
$e_{min}\, [J]$	$5 \cdot 10^{-8}$
$P\, [m^{-2}s^{-1}]$	$1 \cdot 10^{6}$
ϕ_0	10^{-3}

Table 5.1: Standard setup used in numerical tests with the Algorithm 1.

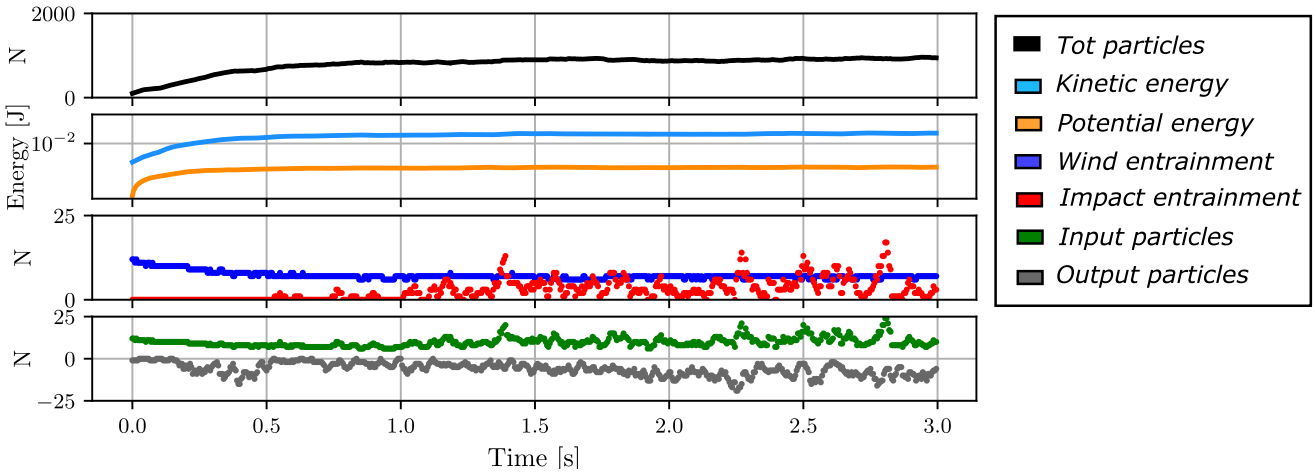

Figure 5.1: (first row) Total number of particles; (second row) Kinetic and potential energy of the system; (third row) Number of particles entrained by wind action and impacts; (forth row) Number of particles that are introduced into and escape from the system. Setup of Table 5.1.

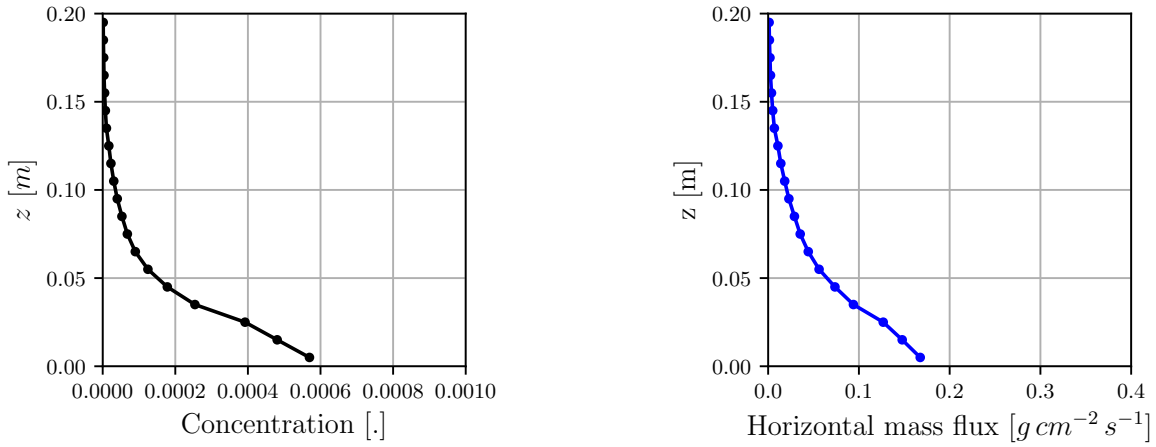

Figure 5.2: (left) Particles concentration and (right) horizontal mass flux at different heights. Setup of Table 5.1.

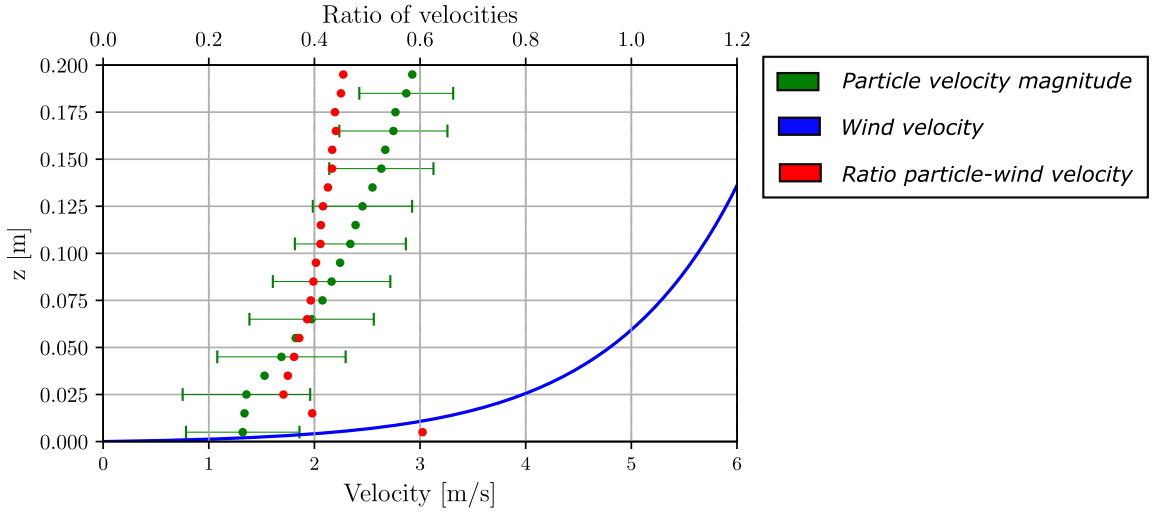

Figure 5.3: Mean and standard deviation of magnitude of particles velocities (green dots), wind flow velocity (blue full line) and the ratio of particles versus wind velocity (red dots) as function of the distance from the ground. Setup of Table 5.1.

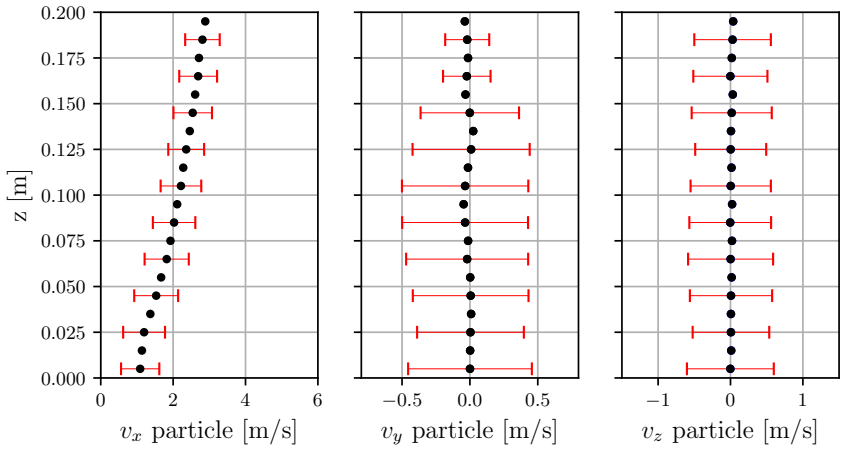

Figure 5.4: Mean and standard deviation of the components of particles velocities: (left) horizontal along wind v_x; (center) horizontal transversal v_y; (right) vertical v_z. Setup of Table 5.1.

Change of Dissipation Figure 5.6 focuses on the effect of change in parameters of Dissipation Model 1 (see Eq. (4.2)). In particular, the width of interval to which α belongs is fixed while its midpoint $\overline{\alpha}$ changes. The number of particles increases as $\overline{\alpha}$ increases, i.e. the dissipation decreases. For too low dissipation the number of particles grows and does not reach a steady value. The role of impact entrainment increases as dissipation decreases (see Figure 5.6-(a),(b),(c)). In fact, an increase in α corresponds to a decrease of parameter S introduced in Chapter 4, which controls impact entrainment. The effect on particles concentration with respect to ground distance is shown in Figure 5.6-(d). The particles concentration increases as $\overline{\alpha}$ increases due to the increase in particle number and impact entrainment. Also the height of the saltation layer increases due to the decrease of energy dissipation of the system. It can be observed also from the increase in potential energy.
Figure 5.5 focuses on the effect of change parameter $e_{inf} = e_{sup} =: \overline{e}$ of Dissipation Model 2 (see Eq. (4.3)) while $\alpha_0^{inf} = 0.2$ and $\alpha_0^{sup} = 0.7$. The system does not show a strong dependence on the parameter $\overline{e}$. Further, in Figure 5.5-(a) the result for Dissipation Model 1 and $\alpha \in \left[\alpha_0^{inf}, \alpha_0^{sup}\right]$ is reported. As we can see, the results do not show a strong dependency on dissipation model change, provided that α_k of Dissipation Model 1 is equal to α_0^k of Dissipation Model 2, for $k = \{inf, sup\}$.

Change of e_{min} Figure 5.7 focuses on the effect of changing e_{min} is shown. Since e_{min} is the minimum energy of ejected particles, the lower e_{min} is, the more low-energy particles are considered, which perform low trajectories. In fact, decreasing e_{min} the ground concentration increases. Conversely, the higher e_{min} is, the lower the number of particles emitted during impacts is: an increase of e_{min} corresponds to an increase of S (see Chapter 4). It can be observed in Figure 5.7-(a),(b),(c) where the role of impact entrainment decreases.

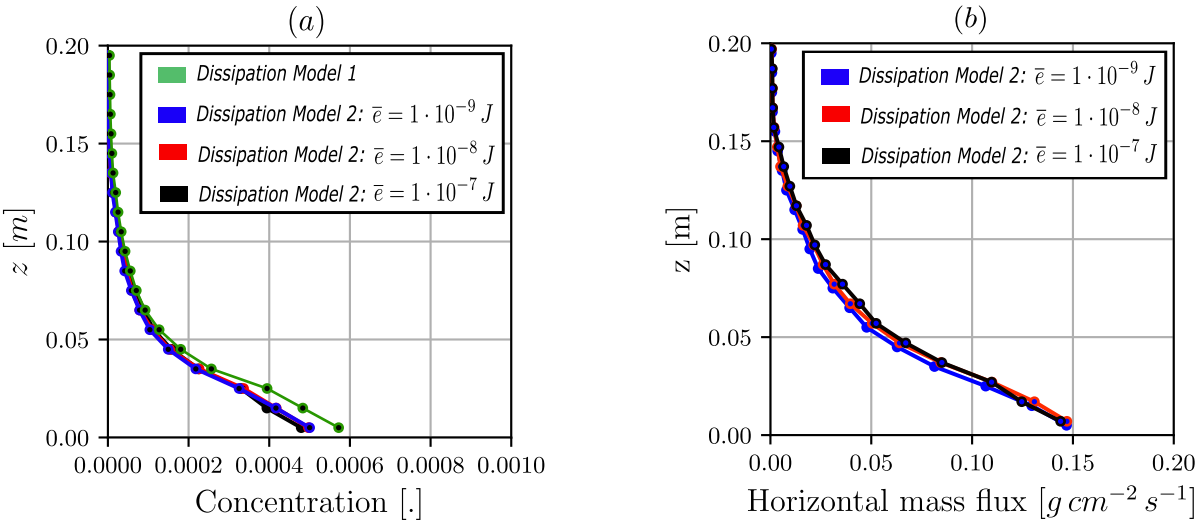

Figure 5.5: Dependence of Dissipation Model 2 from $e_{inf} = e_{sup} =: \overline{e}$ (refer to Eq. (4.3)): (a) particles concentrations and (b) horizontal mass fluxes as functions of the height from the ground. In (a) the particles concentration for Dissipation Model 1 and $\alpha \in \left[\alpha_0^{inf}, \alpha_0^{sup}\right]$ is also represented.

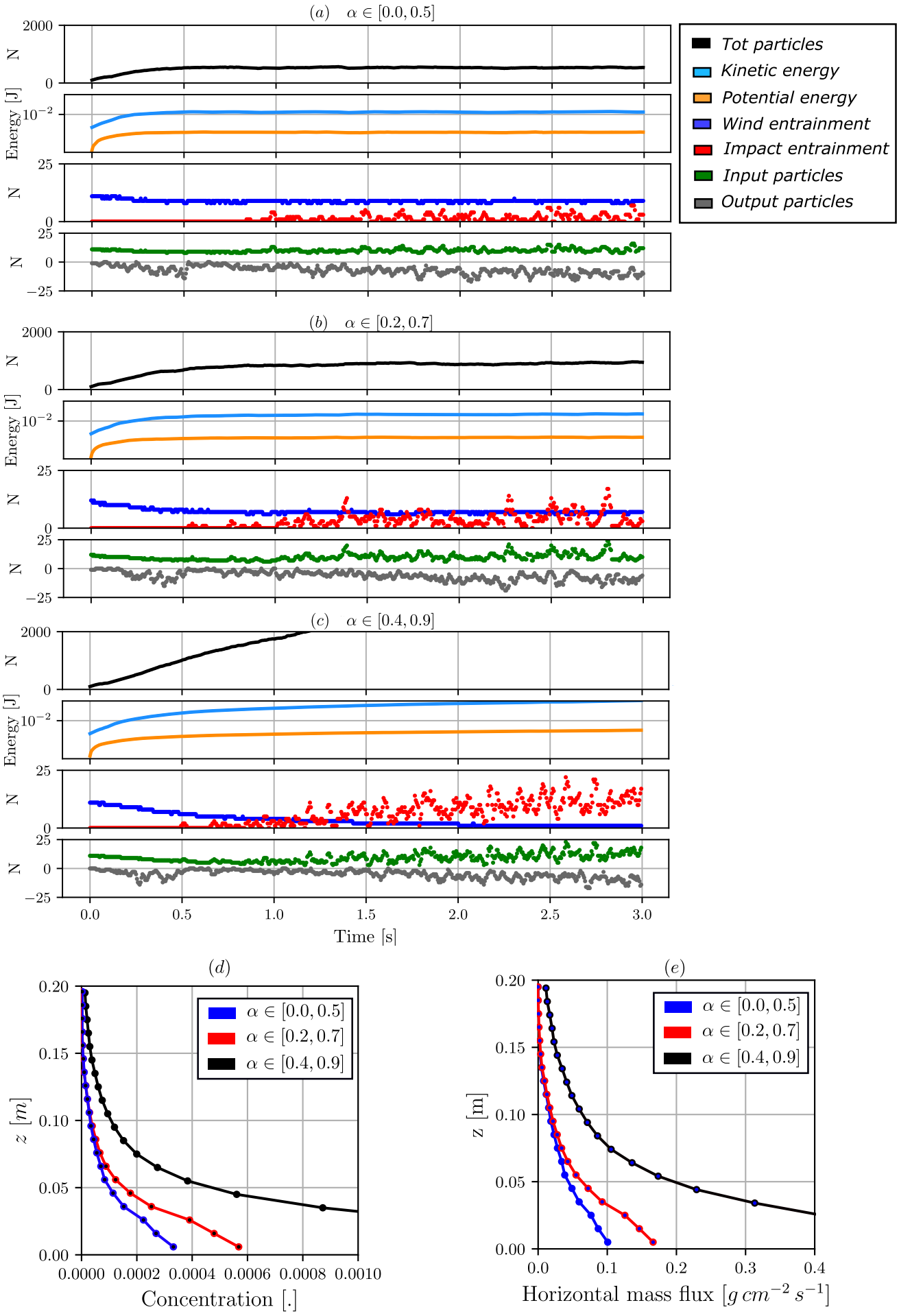

Figure 5.6: Change of parameters of Dissipation Model 1: (a) $\alpha \in [0.0,0.5]$; (b) $\alpha \in [0.2,0.7]$; (c) $\alpha \in [0.4,0.9]$. In each subfigure the following quantities are shown: (first row) Total number of particles; (second row) Kinetic and potential energy of the system; (third row) Number of particles entrained by wind action and impacts; (forth row) Number of particles that are introduced into and escape from the system. (d) Particles concentrations and (e) horizontal mass fluxes as functions of the height from the ground.

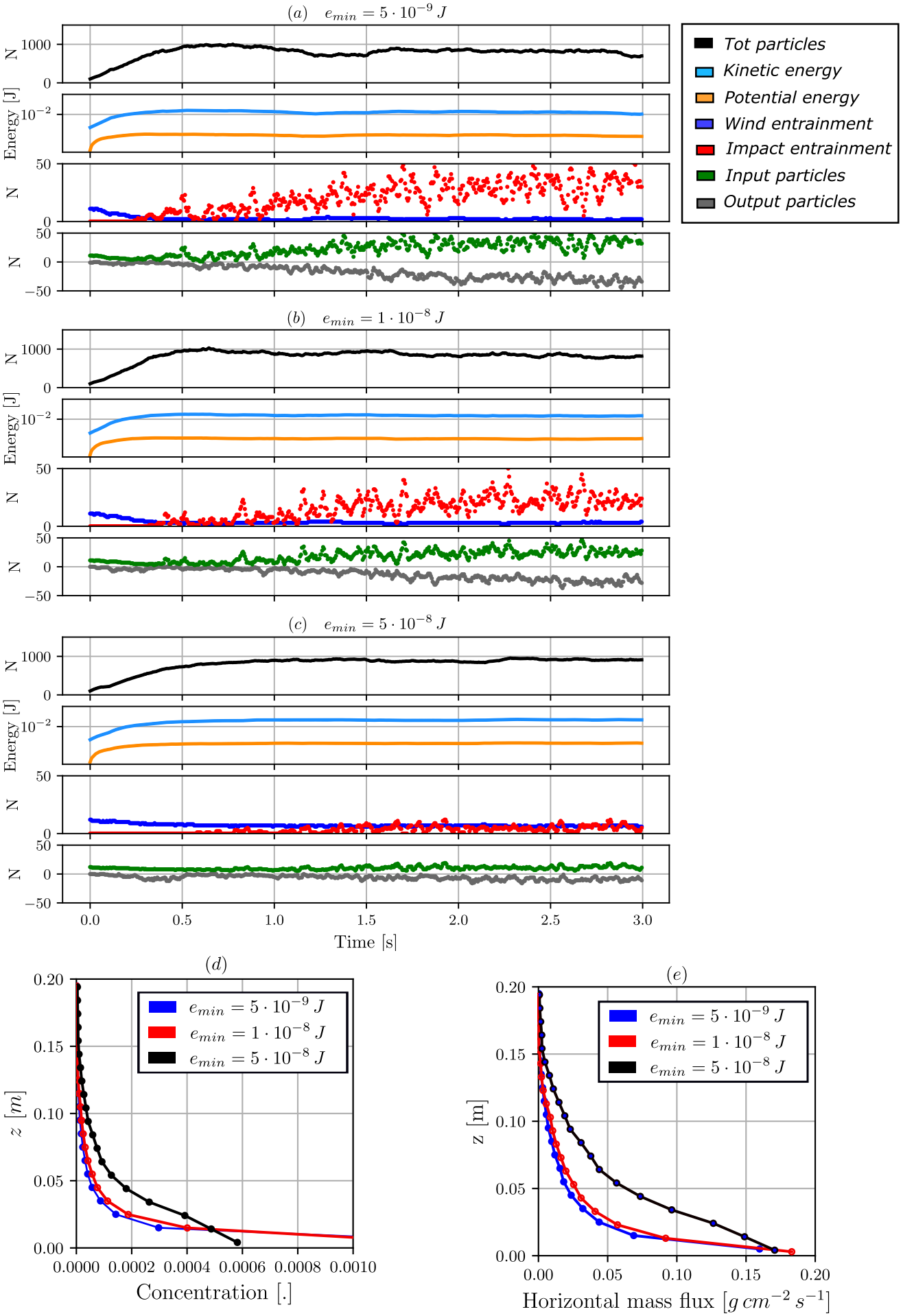

Figure 5.7: Effect of e_{min}: (a) $e_{min} = 5 \cdot 10^{-9}\ J$; (b) $e_{min} = 1 \cdot 10^{-8}\ J$; (c) $e_{min} = 5 \cdot 10^{-8}\ J$. In each subfigure the following quantities are shown: (first row) Total number of particles; (second row) Kinetic and potential energy of the system; (third row) Number of particles entrained by wind action and impacts; (forth row) Number of particles that are introduced into and escape from the system. In (d) particles concentrations and (e) horizontal mass fluxes as functions of the height from the ground.

Change of Fluid Entrainment Figures 5.8 and 5.9 focus on the effect of changing parameters P and ϕ_0 of fluid entrainment model (see Eq. (3.4)). The higher P or ϕ_0 are, the larger is the number of particles entrained by wind as well as the particles concentration.

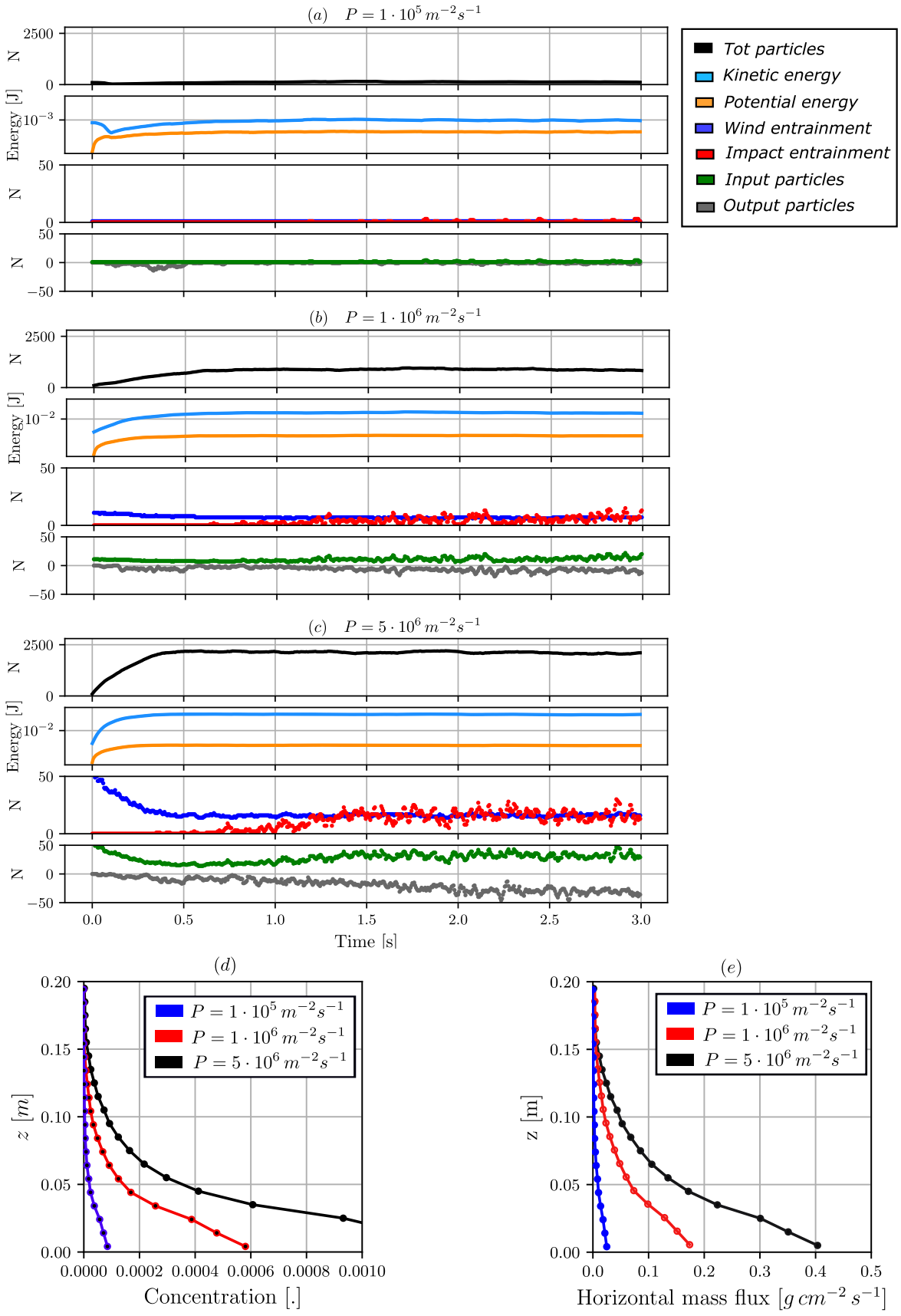

Figure 5.8: Effect of P in fluid entrainment model (refer to Eq. (3.4)): (a) $P = 1 \cdot 10^5\, m^{-2}s^{-1}$; (b) $P = 1 \cdot 10^6\, m^{-2}s^{-1}$; (c) $P = 5 \cdot 10^6\, m^{-2}s^{-1}$. In each subfigure the following quantities are shown: (first row) Total number of particles; (second row) Kinetic and potential energy of the system; (third row) Number of particles entrained by wind action and impacts; (forth row) Number of particles that are introduced into and escape from the system. In (d) particles concentrations and (e) horizontal mass fluxes as functions of the height from the ground.

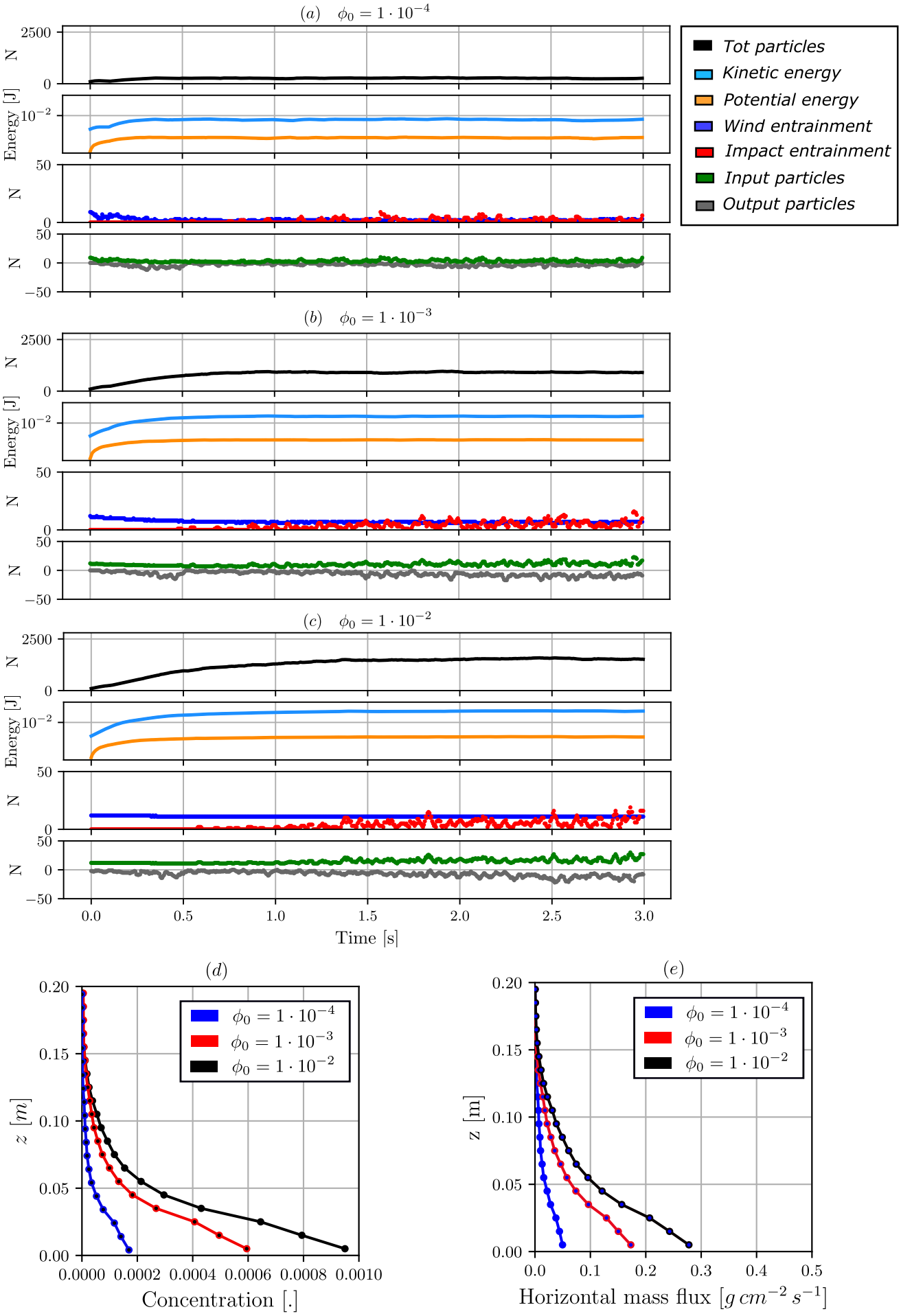

Figure 5.9: Effect of ϕ_0 in fluid entrainment model (refer to Eq. (3.4)): (a) $\phi_0 = 1{\cdot}10^{-4}$; (b) $\phi_0 = 1{\cdot}10^{-3}$; (c) $\phi_0 = 1 \cdot 10^{-2}$. In each subfigure the following quantities are shown: (first row) Total number of particles; (second row) Kinetic and potential energy of the system; (third row) Number of particles entrained by wind action and impacts; (forth row) Number of particles that are introduced into and escape from the system. In (d) particles concentrations and (e) horizontal mass fluxes as functions of the height from the ground.

Change of u^* The effect of increasing the wind strenght is shown in Figures 5.10 and 5.11. As expected, the number of particles, the particles concentration and velocities increase as the wind strenght increases.

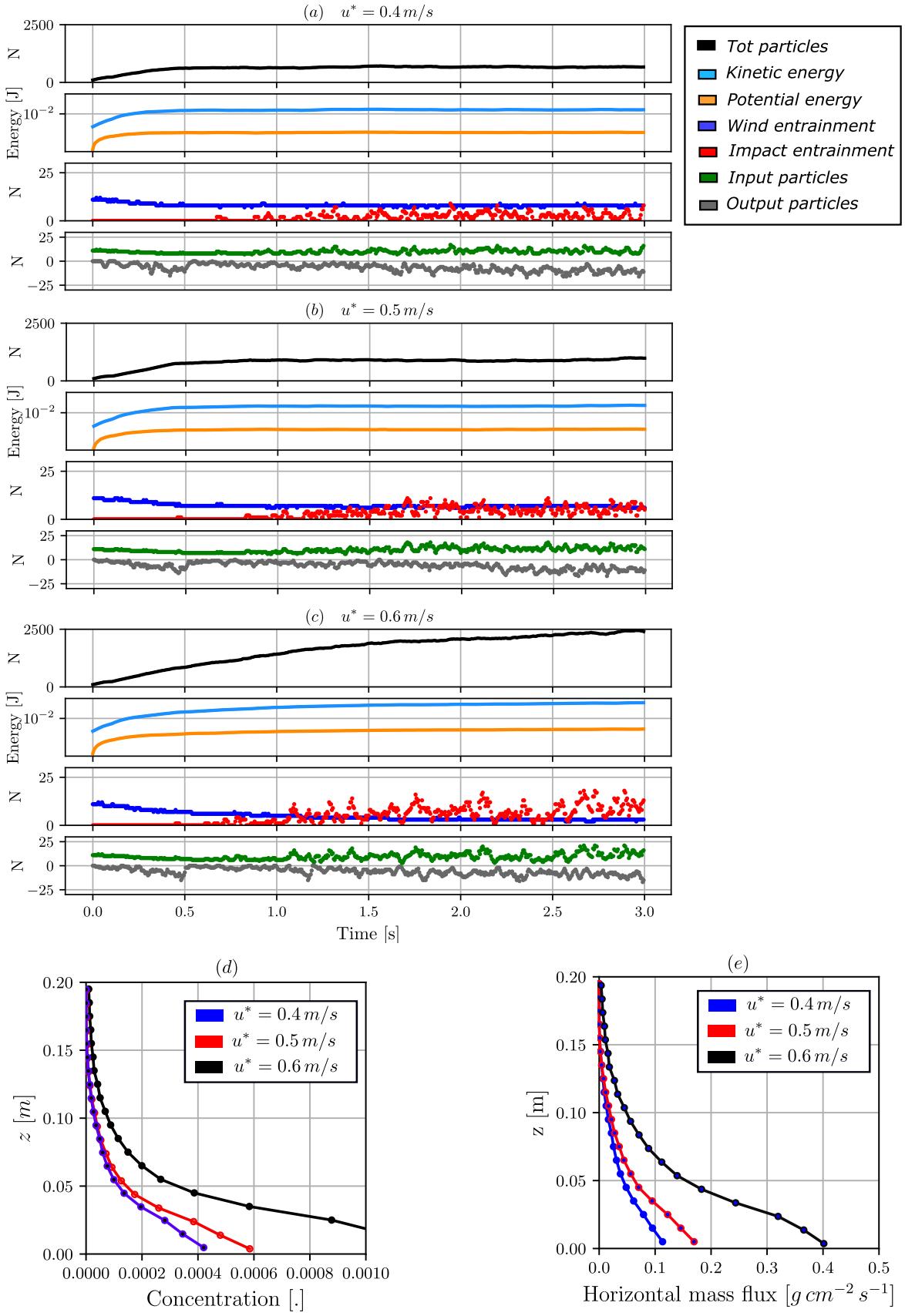

Figure 5.10: Effect of u^*: (a) $u^* = 0.4\,m/s$; (b) $u^* = 0.5\,m/s$; (c) $u^* = 0.6\,m/s$. In each subfigure the following quantities are shown: (first row) Total number of particles; (second row) Kinetic and potential energy of the system; (third row) Number of particles entrained by wind action and impacts; (forth row) Number of particles that are introduced into and escape from the system. In (d) particles concentrations and (e) horizontal mass fluxes as functions of the height from the ground.

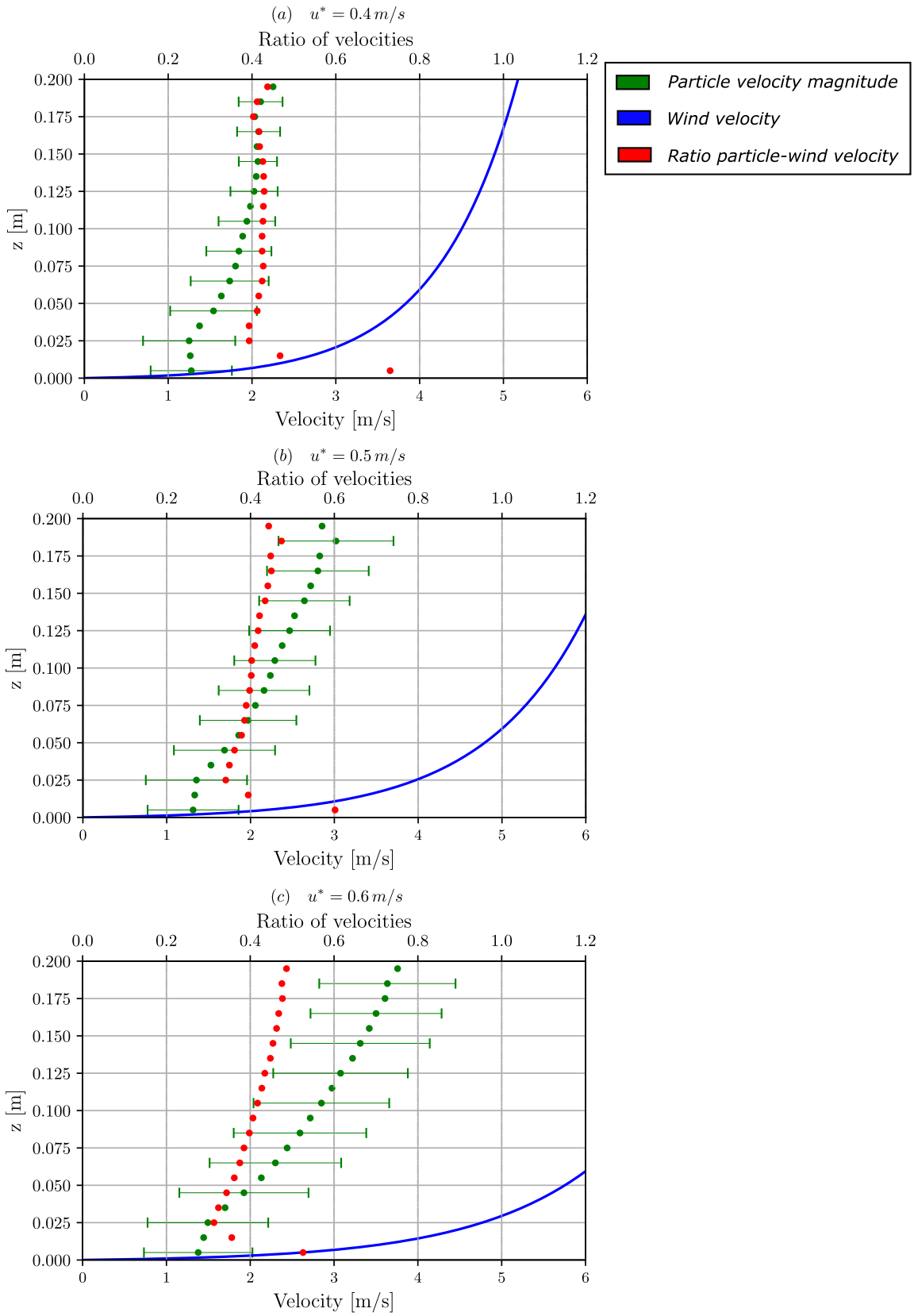

Figure 5.11: Effect of u^*: (a) $u^* = 0.4\,m/s$; (b) $u^* = 0.5\,m/s$; (c) $u^* = 0.6\,m/s$. Mean a standard deviation of magnitude of particle velocities (green dots); Wind flow velocity (blue solid line); Ratio of particles and wind velocity (red dots) as functions of height from the ground.

Change of Particle Diameter The effect of change particle diameter is shown in Figures 5.12 and 5.13. The particles concentration on the ground increases as particle diameter increases, while the height of saltation layer decreases. This is due to lower trajectories of bigger particles. The particle velocity decreases as particle diameter and therefore mass increases, and consequently the ratio between particles and wind velocities. It can be observed in Figure 5.13 that bigger particles are less affected by wind flow.

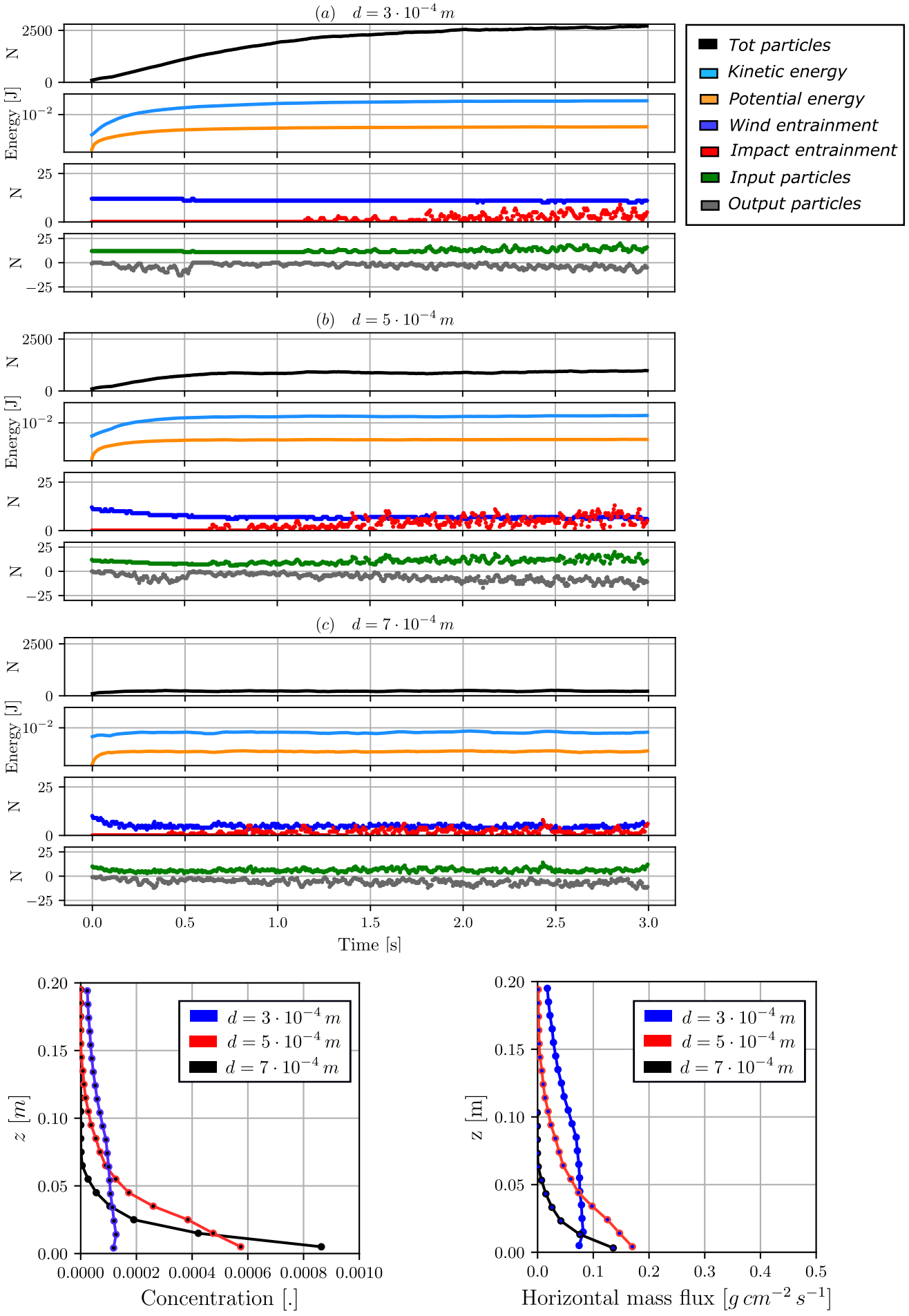

Figure 5.12: Effect of particle diameter: (a) $d = 3 \cdot 10^{-4}\, m$; (b) $d = 5 \cdot 10^{-4}\, m$; (c) $d = 7 \cdot 10^{-4}\, m$. In each subfigure the following quantities are shown: (first row) Total number of particles; (second row) Kinetic and potential energy of the system; (third row) Number of particles entrained by wind action and impacts; (forth row) Number of particles that are introduced into and escape from the system. In (d) particles concentrations and (e) horizontal mass fluxes as functions of the height from the ground.

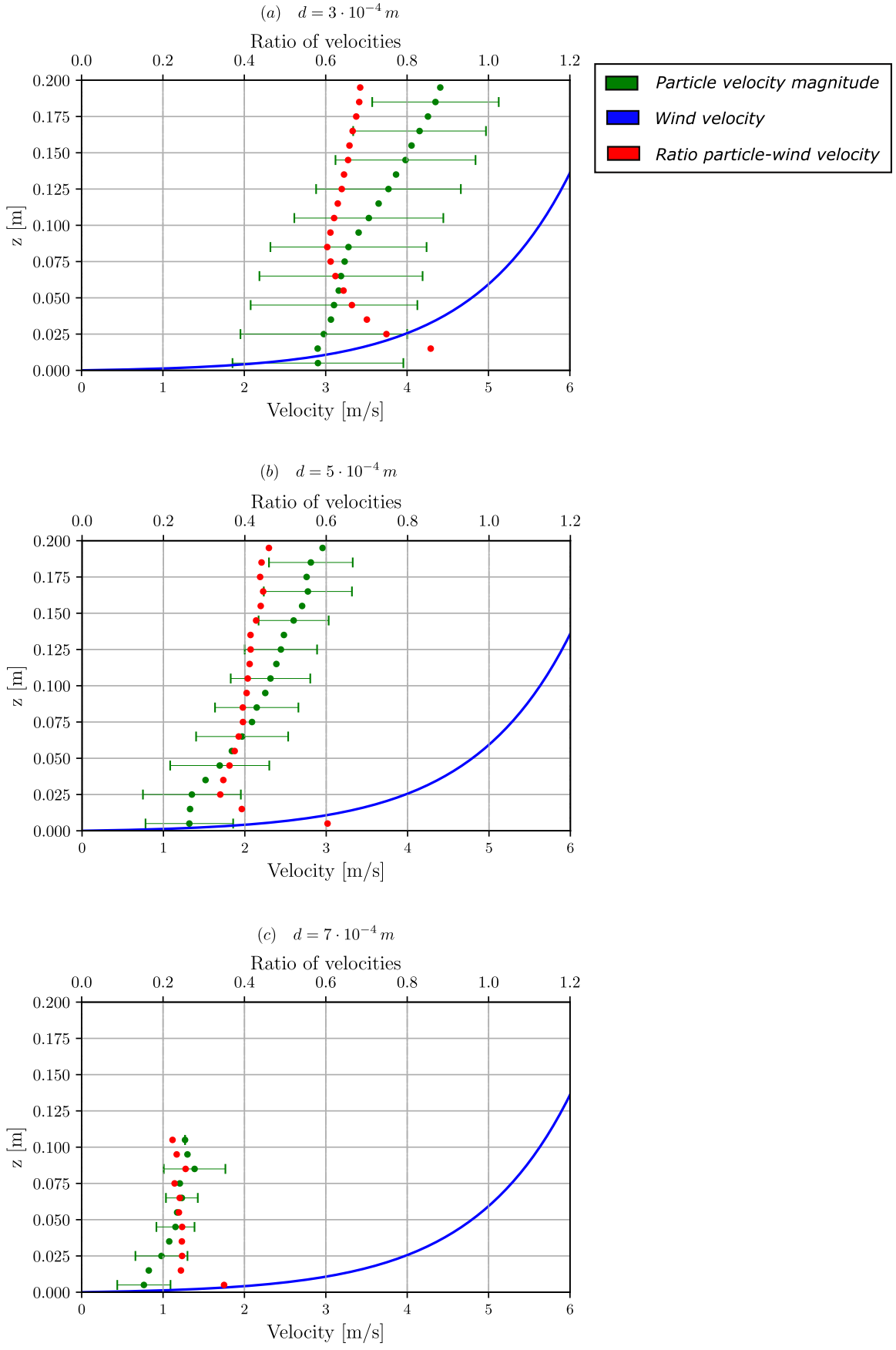

Figure 5.13: Effect of particle diameter: (a) $d = 3 \cdot 10^{-4}\, m$; (b) $d = 5 \cdot 10^{-4}\, m$; (c) $d = 7 \cdot 10^{-4}\, m$. Mean a standard deviation of magnitude of particle velocities (green dots); Wind flow velocity (blue solid line); Ratio of particles and wind velocity (red dots) as functions of height from the ground.

5.2 Simulations in the Polidisperse Case

The effect of consider a spectrum of diameters in the same simulation is shown in Figure 5.16, 5.15 and 5.17. The Figure 5.16 also reports the comparison with the results obtained in the case of a monodisperse distribution discussed in the previous section. The distribution used in the polidisperse case is shown in Figure 5.14. We can see that larger particles tend to stay closer to the ground (see Figure 5.15) in agreement with experimental observations. In Figure 5.16-(b) the range of diameters is divided into nine intervals in order to compute the particles concentration for each of them and highlight the role of each interval in the total particles concentration. The effect of the polidisperse case is also shown in Figure 5.17 where the magnitude of particles velocities increases due to the presence of smaller particles. Further, the standard deviation increases due to the presence of particles with different diameters.

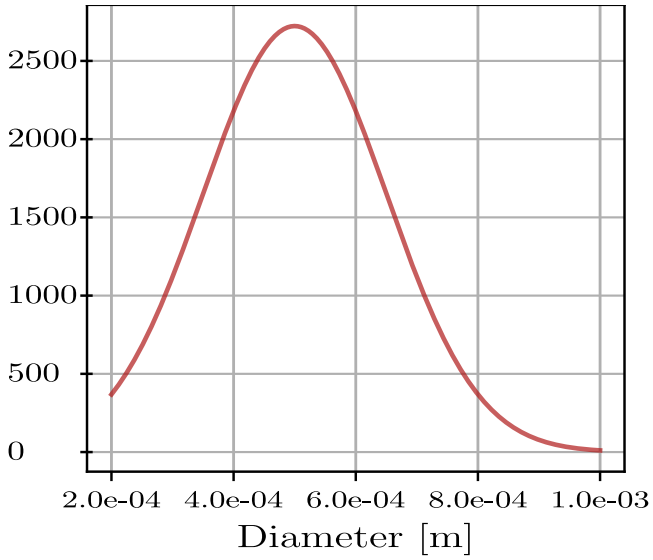

Figure 5.14: Diameter distribution considered in the polidisperse case: a truncated normal distribution in $[2 \cdot 10^{-4}\, m,\, 1 \cdot 10^{-3}\, m]$ and mean $\overline{d} = 5 \cdot 10^{-4}$.

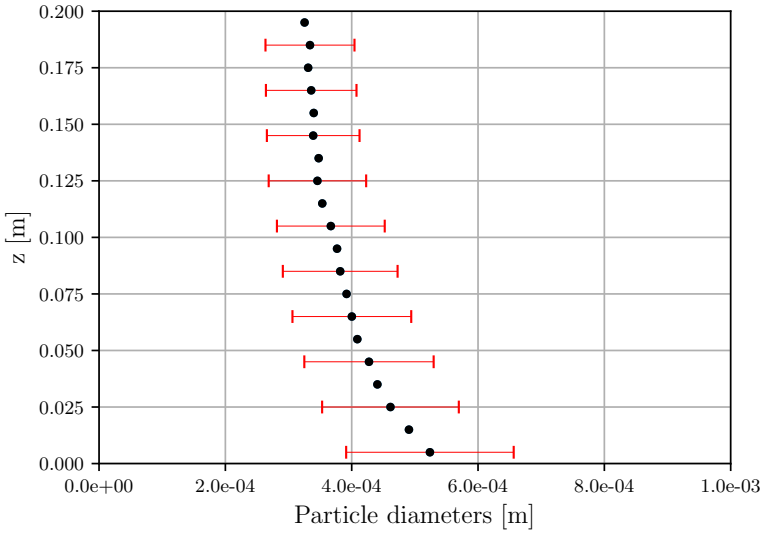

Figure 5.15: The mean and standard deviation of particles diameter distribution as a function of height from the ground.

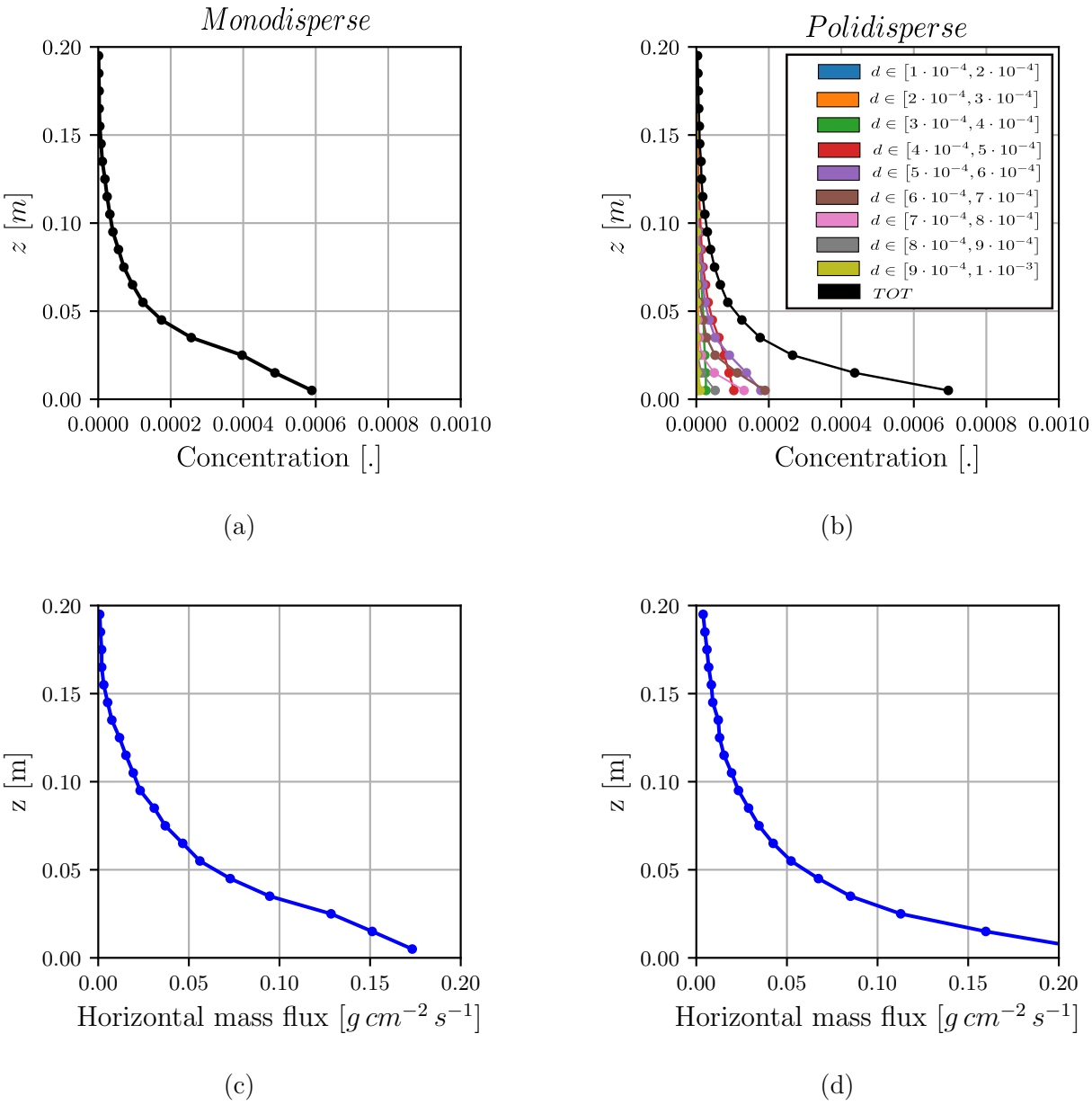

Figure 5.16: Particles concentrations (top row) and horizontal mass flux (bottom row) as a function of the height from the ground. On the left, monodisperse case with $d = 5 \cdot 10^{-4}\,m$; on the right, polidisperse case with diameter distribution as in Figure 5.14. In (b) the range of diameters is divided into nine intervals in order to compute the particles concentration for each range of diameter, while the black line identify the total particles concentration.

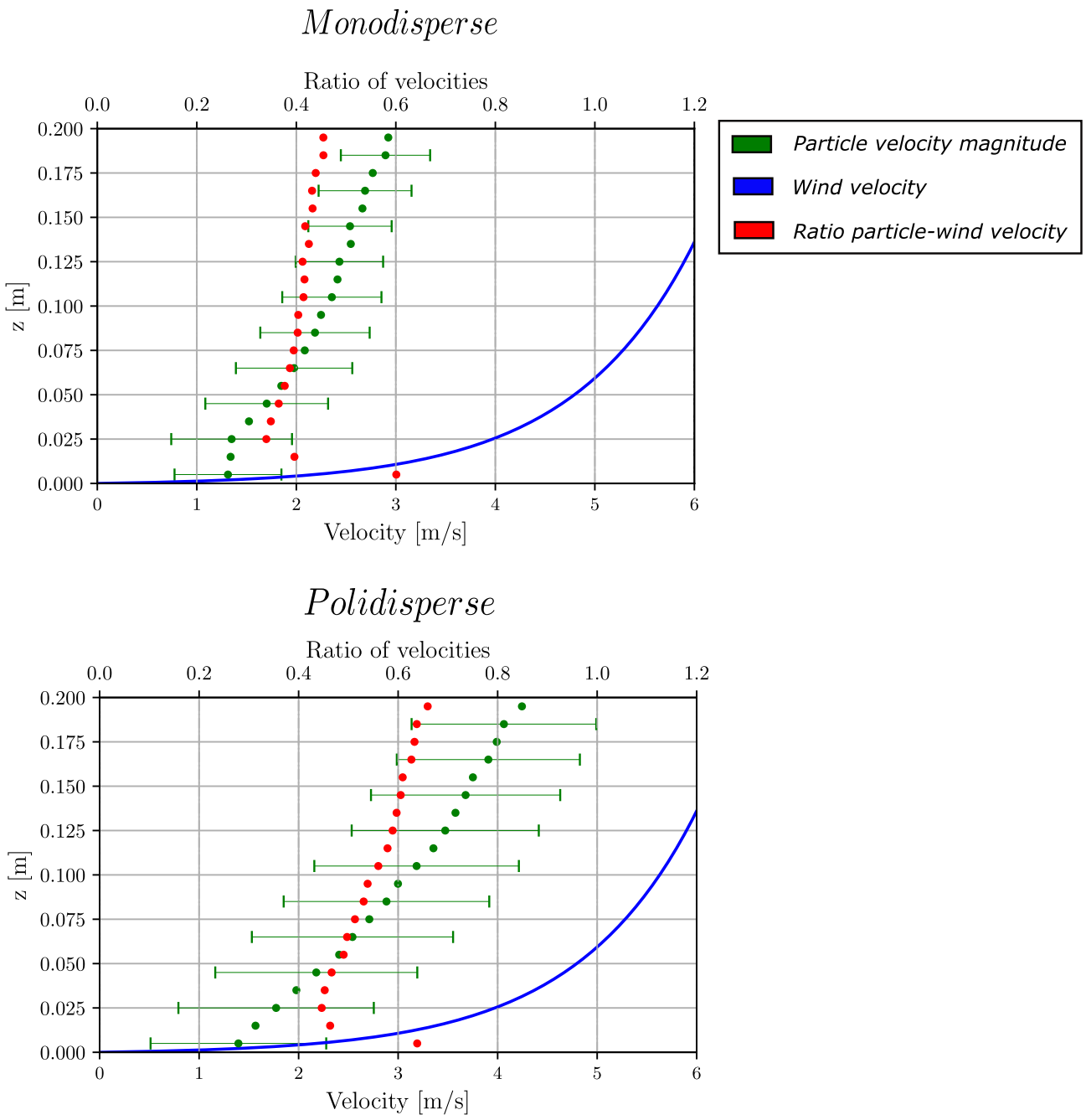

Figure 5.17: Comparison between monodisperse and polidisperse case. (green dots) Mean and standard deviation of magnitude of particles velocities; (blue solid line) Wind velocity; (red dots) Ratio of particles and wind velocity as a function of height from the ground.

5.3 Genealogy Tree Simulations

This section presents the results of numerical tests performed with Algorithm 2 relative to the impact dynamics described in Chapter 3. In the following we start from a *ancestor* in order to understand the behaviour of the *genealogy* of a single particle entrained into the system. Table 5.2 identifies the *standard setup* considered in the monodisperse case. Individual changes were then made to parameters and the impact model used in order to observe their effect. The maximum number G_{max} of generations is set to 15. The integration of the trajectory equation is performed with the Newmark method (see Newmark 1959) and $\Delta t = 5 \cdot 10^{-4}\, s$.

Ancestor information	$e_1 = 1 \cdot 10^{-7}\, J$, $\theta_1 = 45°$, $\varphi_1 = 0°$
$u^*\, [m/s]$	0.5
$z_0\, [m]$	0.001
Diameter $[m]$	$5 \cdot 10^{-4}$
Diameter distribution	Dirac delta
Dissipation model	Model 1
Interval of α	[0.4,0.6]
Ejection model	Model 2
$e_{min}\, [J]$	$5 \cdot 10^{-9}$

Table 5.2: Standard setup used in numerical tests with the Algorithm 2.

Change of Energy Dissipation Figure 5.18 focuses on the change of energy dissipation introduced by the dissipation models. In Figure 5.18-(a),(b),(c) the effect of changes in parameters of Dissipation Model 1 is shown. In particular, the width of the interval to which α belongs is fixed while its midpoint has changed. This corresponds to change the parameter S introduced in Chapter 4: an increase in $\overline{\alpha}$ corresponds to decrease S. The less energy is dissipated, the longer the genealogy of the starting particle is. In fact, the ejected particles at each impact have greater energy, can gain more energy by the wind and eject more particles. Further, increasing dissipation leads to decreasing the number of *successfull impact*, i.e. impacts in which at least one particle is ejected (see Chapter 4). The successful impacts correspond to the *father particles* shown in the figures (yellow dots), while failure impacts correspond to *childless particles* (grey dots).
In Figure 5.18-(d),(e),(f) the Dissipation Model 2 is imposed, that is $\alpha \in [\alpha_{inf}(e_0, \theta_0), \alpha_{sup}(e_0, \theta_0)]$ where:

$$\alpha_k(e_0, \theta_0) = \alpha_0^k \left(1 - e^{-(e_0/e_k)}\right) \sin\theta_0 \qquad k = \{inf, sup\}$$

We set $e_{inf} = e_{sup} =: \overline{e}$. The figure shows the effect of changing $\overline{e}$, while we set $\alpha_0^{inf} = 0.4$ and $\alpha_0^{sup} = 0.9$. We observe that an increase in $\overline{e}$ leads to a decrease in the length of the genealogy. In fact, since $e_{inf} = e_{sup}$ we have that:

$$\overline{\alpha}(e_0, \theta_0) = \left(\frac{\alpha_0^{sup} - \alpha_0^{inf}}{2}\right)\left[1 - e^{-e_0/\overline{e}}\right] \sin\theta_0$$

Then, an increase of $\overline{e}$ corresponds to decrease the mean value of α.

Change of Ejection Model and e_{min} The effect of changing e_{min} is shown in Figure 5.19 for both the ejection models. The effect of increasing e_{min} is similar to increase dissipation. In fact, we recall that increasing e_{min} corresponds to increase S (see Chapter 4) than the effect on the impact model is the same of increase dissipation. It reduces both the number of particles ejected at each impact and the number of successfull impact. Then, the lenght of the genealogy decreases as e_{min} increases. Numerical tests suggest that the equi-division of energy proposed in Ejection Model 1 leads to the ejection of too many particles at each impacts, each of them with too little energy to continue the process. In fact, the Ejection Model 1 leads to a great number of particles in first generations and shorter genealogy with respect to the second model proposed (see Figure 5.19-(a),(b),(c)). For this reason, the second model is mainly used in subsequent tests.

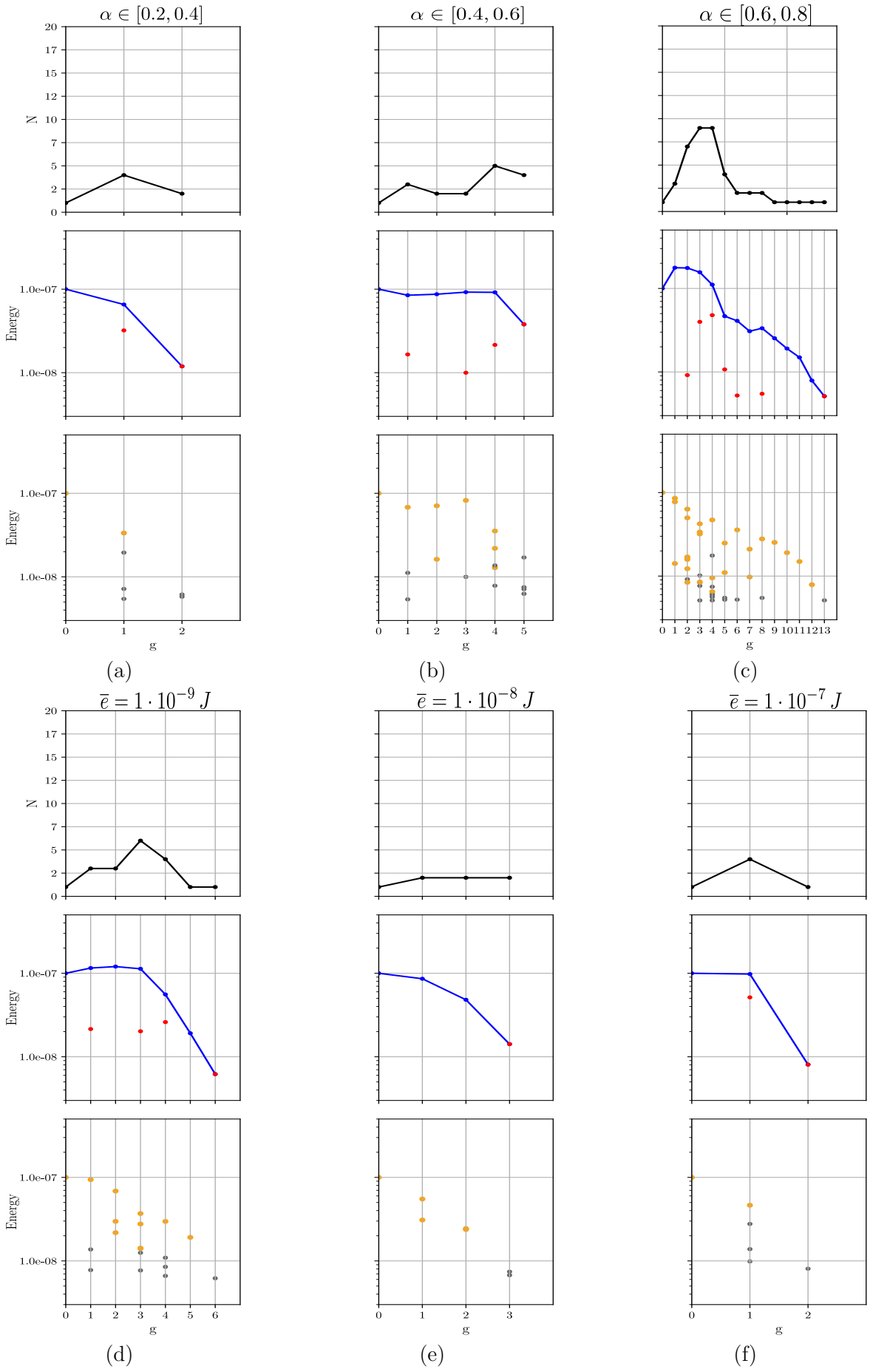

Figure 5.18: Effect of changing the midpoint $\bar{\alpha}$ of the restitution coefficient in *Dissipation Model* 1: (a) $\alpha \in [0.2,0.4]$; (b) $\alpha \in [0.4,0.6]$; (c) $\alpha \in [0.6,0.8]$. Effect of changing the parameter $\overline{e}$ of Dissipation Model 2: (d) $\overline{e} = 1 \cdot 10^{-9}\, J$; (e) $\overline{e} = 1 \cdot 10^{-8}\, J$; (f) $\overline{e} = 1 \cdot 10^{-7}\, J$. The number of particles (top row) and the energy (middle row) per generation is shown, with the fraction of energy associated to particles that do no have children (red dots); (bottom row) energy of each particle per generation with the distinction between *father* (yellow dots) and *childless particles* (gray dots).

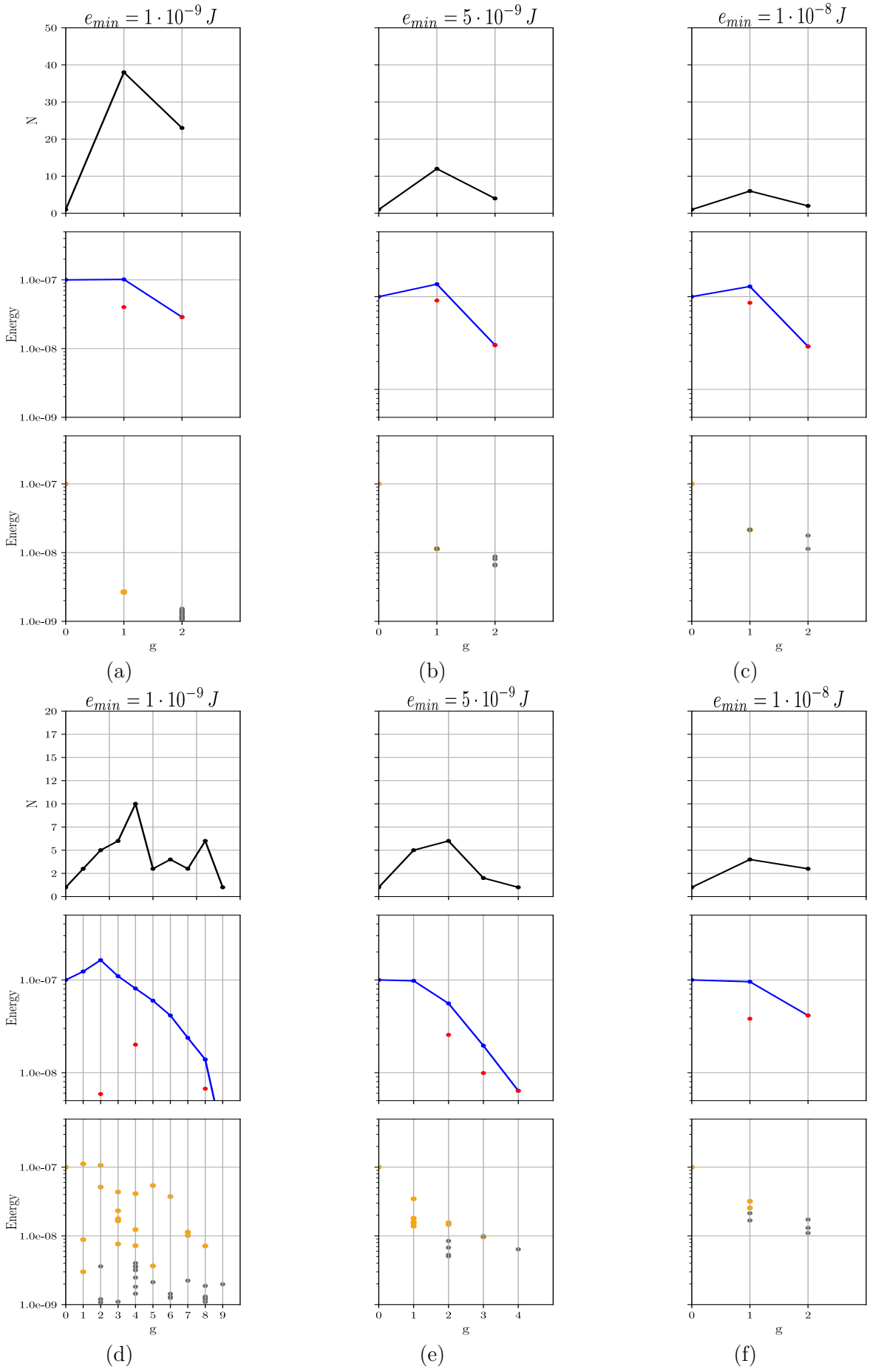

Figure 5.19: Effect of changing e_{min}: (a),(d) $e_{min} = 1 \cdot 10^{-9}\,J$; (b),(e) $e_{min} = 5 \cdot 10^{-9}\,J$; (c),(f) $e_{min} = 1 \cdot 10^{-8}\,J$. (a),(b),(c) *Ejection Model* 1; (d),(e),(f) *Ejection Model* 2. The number of particles (top row) and the energy (middle row) per generation is shown, with the fraction of energy associated to particles that do no have children (red dots); (bottom row) energy of each particle per generation with the distinction between *father* (yellow dots) and *childless particles* (gray dots).

Change of Particle Diameter and Wind Strength The effect of changing u^* and particle diameter is shown respectively in Figures 5.20 and 5.21. The effect of decreasing particle diameter is similar to increasing wind strength: the number of generations increases and the number of particles rapidly increases. In both cases a single particle gains more energy by the wind (see Chapter 2). So, its *fertility* increases, which means that it can eject more particles during impacts. Then, in order to avoid this effect, dependence of dissipation model or e_{min} on u^* and particle diameter should be considered in future improvements.

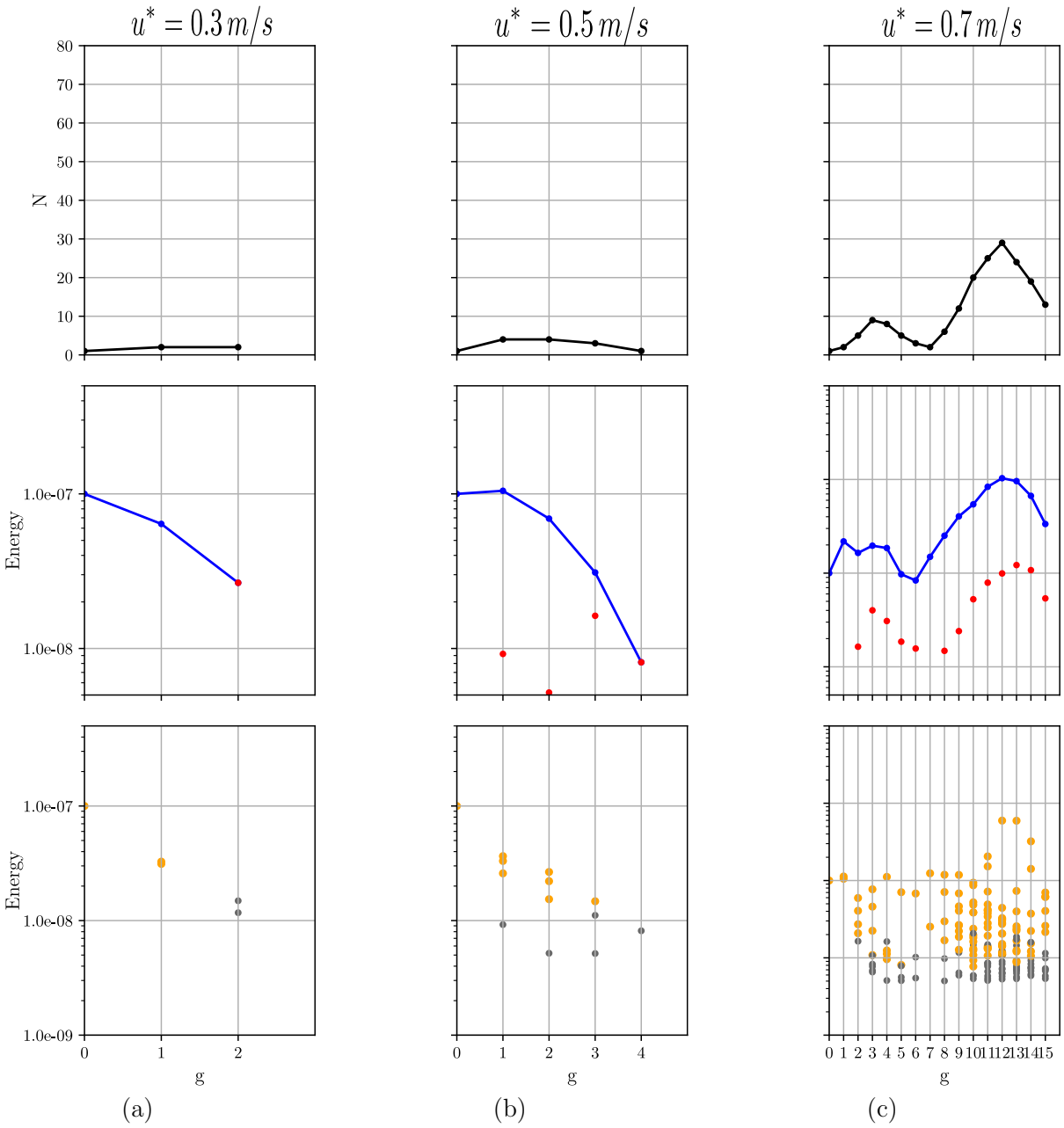

Figure 5.20: Effect of changing u^*: (a) $u^* = 0.3\,m/s$; (b) $u^* = 0.5\,m/s$; (c) $u^* = 0.7\,m/s$. The number of particles (top row) and the energy (middle row) per generation is shown, with the fraction of energy associated to particles that do no have children (red dots); (bottom row) energy of each particle per generation with the distinction between *father* (yellow dots) and *childless particles* (gray dots).

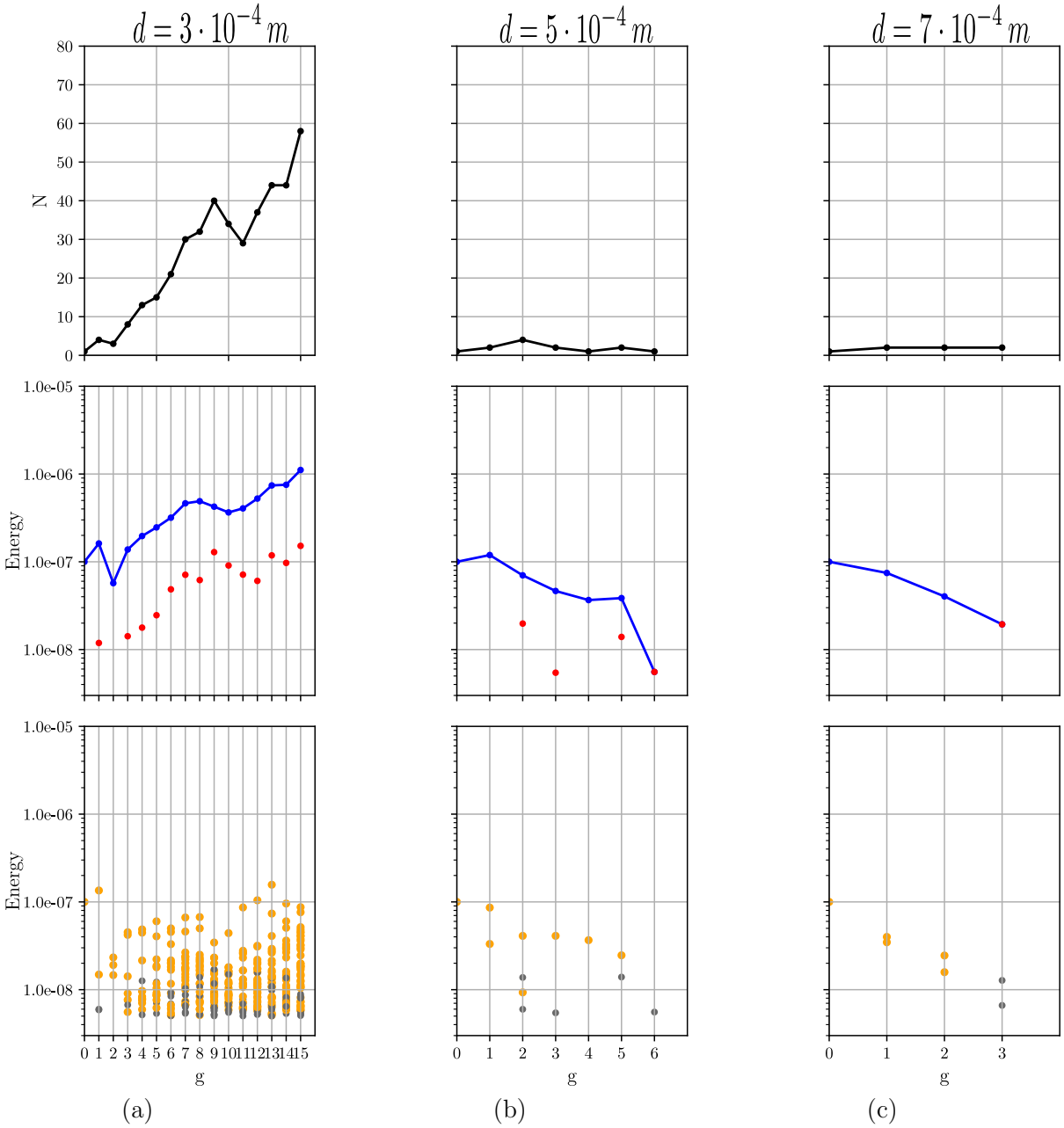

Figure 5.21: Effect of changing the particle diameter: (a) $d = 3 \cdot 10^{-4}\,m$; (b) $d = 5 \cdot 10^{-4}\,m$; (c) $d = 7 \cdot 10^{-4}\,m$. The number of particles (top row) and the energy (middle row) per generation is shown, with the fraction of energy associated to particles that do no have children (red dots); (bottom row) energy of each particle per generation with the distinction between *father* (yellow dots) and *childless particles* (gray dots).

5.4 Discrete Event Simulations of Saltation

This section presents the results of the numerical tests performed using Algorithm 3 relative to the number of particle N described in Chapter 3. Table 5.3 identifies the *standard setup* considered in the following numerical tests for the monodisperse case. Individual changes were then made to parameters in order to observe their effects. All the tests are performed with $N_0 = 1$ and $T_{final} = 3\,s$. The integration of the trajectory equation is performed using the Newmark method (see Newmark 1959) with $\Delta t = 5 \cdot 10^{-4}\,s$.

$u^*\,[m/s]$	0.5
$z_0\,[m]$	0.001
Number of initial particles	1
Diameter $[m]$	$5 \cdot 10^{-4}$
Diameter distribution	Dirac delta
Dissipation model	Model 1
Interval of α	[0.2,0.6]
Ejection model	Model 2
$e_{min}\,[J]$	$5 \cdot 10^{-9}$
$f_0\,[Hz]$	$1 \cdot 10^3$
N_∞	100

Table 5.3: Standard setup used in numerical tests with the Algorithm 3.

Change of Ejection Model In Figure 5.22-(a) the effect of changing the ejection model is shown. As introduced in the previous section, Ejection Model 1 causes too many particles to be emitted during impacts, each of them with too low energy to continue the process and then they rapidly stops. This effect leads the number of particles to fluctuate significantly. For this reason, the Ejection Model 2 is used in the following numerical tests.

The Steady State of Saltation The process reaches the steady state when the number of particles N fluctuates around an average value $\overline{N}$. We can identify three important quantities that characterise the steady state of the system:

- The *mean input frequency* $\overline{f^{in}}$ identified as the mean frequency at which *at least* a new particle is entrained into the system due to both fluid or impact entrainment. It can be identified as an *input event*. This frequency then depends on two different components:
  - the input of particles due to the fluid entrainment model, which is decreasing with $\overline{N}$ due to the model enforced;
  - the impact entrainment, which is increasing with $\overline{N}$. In fact, the more particles there are in the system, the more frequently impacts will occur and then particles will be entrained. Further, it will depend on the impact model, because it controls if new particles are entrained during impacts.
- The mean number of particles $\overline{N^{in}}$ entrained during an input event. It is composed of the number of particles introduced during a fluid entrainment event, that is fixed to one, and the mean number of new particles $\overline{N^{in}_{impact}}$ entrained during an impact, which will depend on the impact model.
- The *mean output frequency* $\overline{f^{out}}$ that is the frequency at which a single particle exits from the system, i.e. a single particle impacts on the ground and stops without emission of newly particles. We can call it an *output event* and depends on the impact model. It will be increasing with $\overline{N}$ because it will depend on the impact frequency.

Both the mean frequencies of input and output are functions of the number of particles $\overline{N}$. However they are difficult to identify analytically. Since the Algorithm 3 proceeds by the occurence of events, these frequencies can be computed from numerical tests. In steady state conditions these quantities should be in equilibrium, following the relation:

$$\overline{N^{in}}\,\overline{f^{in}}(\overline{N}) = \overline{f^{out}}(\overline{N}) \tag{5.1}$$

as suggested by numerical tests (see Table 5.4). In fact, in a fixed time step the mean number of particles introduced should be balanced by the mean number of particles that escapes. The mean number of particles in steady state than is solution of Eq. (5.1).
We observe that changes in parameters of the fluid entrainment frequency and of the impact model lead to change the number of particles of the steady state achieved. This is due to the consequent modification of $\overline{N^{in}}$, $\overline{f^{in}}$ and $\overline{f^{out}}$, that leads to a different value of $\overline{N}$ satisfying Eq. (5.1). In particular, numerical tests suggest that:

- a decrease of the frequency f_{wind} of fluid entrainment causes the number of particles in steady state to decrease (see Figure 5.22-(d));
- both a decrease of energy dissipation, i.e. an increase of the midpoint of α (see Figure 5.22-(b)) of the Dissipation Model 1, or a decrease of e_{min} (see Figure 5.22-(c)) causes the number of particles in steady state to increase. In fact, these changes causes a decrease of the parameter S introduced in Chapter 4. It controls the mean output frequency, the impact entrainment and the mean number of particles entrained by impacts. In particular, the system suffers greatly from the effect of the change in energy dissipation. If the energy dissipation is too low then the output frequency could not balance the input frequency, the number of particles grows and the steady state could not be reached (see Figure 5.22-(b) and Table 5.4).

The effect of changes in particle diameter and u^* is shown respectively in Figures 5.22-(e) and 5.22-(f). In according to numerical tests of Algorithm 2, a decrease of particle diameters or an increase of u^* causes the particles to gain more energy by the wind. This leads to an increase of $\overline{N}$ or eventually to not reach the steady state. In order to avoid this effect, a dependence of dissipation model or e_{min} on u^* and particle diameter should be considered in future improvements.

Test	$\overline{N^{in}}$	$\overline{f^{in}}$	$\overline{N^{in}f^{in}}$	$\overline{f^{out}}$	Steady state
(b)	1.569	598.256	938.663	918.783	yes
	1.838	775.221	1424.856	1424.247	yes
	1.917	1505.992	2886.987	2884.071	yes
	1.899	14764.265	28037.339	24852.875	no
(c)	2.232	1398.524	3121.506	3156.056	yes
	1.818	754.874	1372.361	1350.615	yes
	1.622	624.621	1013.135	1006.777	yes
	1.155	383.744	443.224	452.707	yes
(d)	1.861	782.084	1455.458	1445.733	yes
	1.792	2718.153	4870.930	4936.403	yes
	1.794	1476.361	2648.591	2634.753	yes
	1.832	7767.526	14230.107	14259.809	yes
(f)	1.815	779.869	1415.462	1377.537	yes
	2.007	1158.129	2324.365	2346.230	yes
	2.101	11320.849	23785.104	21183	no

Table 5.4: Results of numerical tests of Algorithm 3 reported in Figure 5.22. The quantities are computed from $t = 1.5\,s$ in order to avoid the effect of transient state.

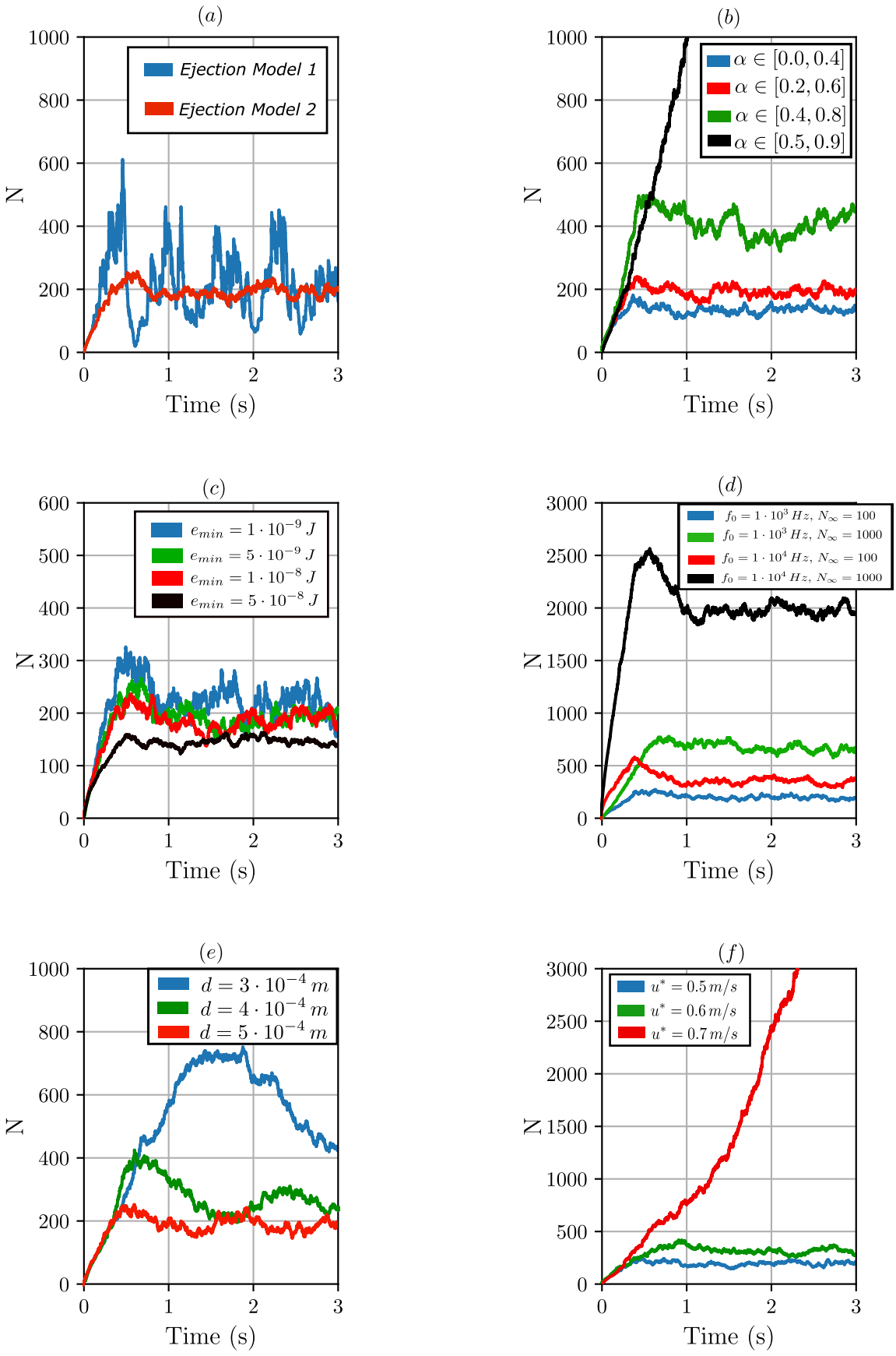

Figure 5.22: Effect of changes in: (a) ejection model; (b) parameters of Dissipation Model 1; (c) e_{min}; (d) parameters of fluid entrainment model; (e) particle diameter; (f) u^*.

Chapter 6

Conclusions and Future Improvements

In this thesis we have presented a particle-based analysis of the saltation process, which is the main mode of windblown sand transport under normal wind conditions. At first the physics of saltation has been presented with a focus on the main features and the most critical aspects in the process description. The saltation is characterized by a random behaviour. Wind flow involved in saltation process is turbulent. This fact makes the description and measurements of specific quantities of the process complex to define. Futher, random shape of sand particles leads to a random behaviour of the grain-bed impact dynamics, which plays a crucial role in the process. Many aspects of saltation are still unclear and debated and the development of numerical models can help shed light on some of these issues.

A detailed study of particle trajectories under a steady and unperturbed wind flow has been conducted. These latter have been computed changing the starting conditions and the main parameters that influence them. This allowed to understand how the individual trajectory is influenced by the particle, wind and ejection properties. Furthermore, it has also led to the identification of a set of particle ejection conditions for which sand particles can gain energy by the wind flow. These are dependent on wind strength and particle diameter. The wind flow can be intended as a source of energy for the saltation process, but it depends on the particles ejection conditions. These latter are defined by the impact and fluid entrainment models, which then play a crucial role in the saltation model.

Starting from the preliminary version of the semi-stochastic Lagrangian model developed by Roberto Nuca in his PhD research activity, we have evolved several modelling and algorithmic aspects. The purpose of the model is to provide quantitative information of saltation and to understand statistical properties of aeolian sand transport mechanism.
The model numerically computes each particles trajectories by solving the Newton law taking into account drag and gravitational forces, and also taking into account the ground collisional dynamics. The wind flow is imposed as known function, avoiding to solve explicitly the Navier-Stokes equations with a consequent reduction of the computational cost. For sake of simplicity, the mean wind velocity profile has been considered, neglecting turbulence fluctuations. The model takes into account the particle entrainment by the wind action on the sand bed. The fluid entrainment is modeled introducing particles from the ground and it is based on experimental observations.
The model does not deterministically simulate the impact between the impacting particle and those on the ground as in a DEM approach. The grain-bed collision is solved by means of stochastic approaches, i.e. by the introduction of an *impact model*. This allows to account for the random shape of particles. Different impact models have been proposed and tested, all of them are based on the principle of conservation of energy. The mid-air collisions among travelling particles have been neglected in order to reduce the modelling complexity and the computational cost.

In conjunction with the complete model other two simplified models have been proposed. Each of them follows the evolution of the number of particles in the system, which is the most representative quantity of the sand transport process. They have been designed in order to highlight the effect of impact and fluid entrainment models in the growth of particles number. These models are based on a simplified description of the saltation process. It allows to reduce the computational cost. In fact, in future improvements the trajectory database introduced in Chapter 2 could be used to obtain impact information of each particle, avoiding the numerical integration of trajectories. This models can be seen as auxiliary tools of the complete saltation model proposed.

In order to understand their effect on the system, numerical tests have been performed changing parameters of the impact and fluid entrainment models as well as physical constants. Results are coherent with the physics. However, a proper dataset from experiments would allow the model to be validated, by properly setting the parameters.
The complete model presented in this thesis show a great flexibility in embedding new modelling aspects. Therefore we can consider several improvements for the future.

Turbulence Fluctuations As pointed out in Chapter 1, the characterization of turbulence in the saltation layer and turbuence fluctuations experienced by sand particles is poorly understood. In our model, pointwise turbulence fluctuations can be introduced with custom temporal spectrum in order to understand their effect on the saltation process. Experiments could clarify the statistical description of turbulence fluctuations experienced by particles.

The Feedback of Saltating Particles on the Fluid Flow In Chapter 1 we pointed out that the feedback of saltating particles is one of the features of the saltation process. Saltating particles affect both mean flow and turbulence. J. Kok et al. 2009 neglected the effect of saltating particles on turbulence and introduced an equation for the evolution of mean wind velocity profile obtained computing the momentum flux subtracted by particles to the wind flow. The effect of particles on turbulence fluctuations is still poorly understood. In our model, the momentum flux subtracted by particles can be computed at each time step. Then it can be used to modify the mean wind velocity profile. The effect of particles on turbulence fluctuations could be eventually introduced on the basis of experimental results.

Impact and Fluid Entrainment Models Both the impact and fluid entrainment models introduced in this thesis are based on experimental observations and on energy principles. The results obtained from impact experiments (see Chapter 1) with natural sand could help in identifying the splash functions that describe the grain-bed impacts. Further, experimental results could help characterize the particles entrained by the wind action.

Mid-Air Collisions The effect of mid-air collisions is still debated. To the best of our knowledge in the numerical models (see J. Kok et al. 2009, Huang et al. 2020) impacts among saltating particles are always neglected in order to reduce computational costs. In our model, during the *impact step* both particle-bed and particle-particle collisions could be checked. In order to account of random shape of particles, the collisional dynamics between particles can be described by means of stochastic approaches.

Rotational Dynamics The rotational dynamics equation of sand particles can be introduced. It means also to simulate random moments of inertia for describing particles in order to account of random shape of particles. Both the impact model and the mid-air collision model should take into account of particle rotation, establishing the spin of the particles after impacts and/or eventually taking into account the rotation of the impacting particles. Further, the fluid dynamic Magnus force can be considered in the equation of motion.

The Tracking of Ground Particles The implementation of particle tracking on the ground would allow to address the evolution of the particle diameter distribution on the sand bed. In fact, this can be modified during the saltation process according to particles that are entrained into the wind flow and particles deposited on the ground.

Bibliography

Andreotti, B. (2004). "A two-species model of aeolian sand transport". In: *Journal of Fluid Mechanics* 510, pp. 47–70.

Bagheri, G. et al. (2016). "On the drag of freely falling non-spherical particles". In: *Powder Technology* 301, pp. 526–544.

Bagnold, R.A. (1941). *The physics of blown sand and desert dunes*. New York: Methuen.

Beladjine, D. et al. (2007). "Collision process between an incident bead and a three-dimensional granular packing". In: *Physical review. E, Statistical, nonlinear, and soft matter physics* 75 6 Pt 1, p. 061305.

Crassous, J. et al. (2007). "Impact of a projectile on a granular medium described by a collision model". In: *Physical review letters* 99 24, p. 248001.

Giudice, A.L., R. Nuca, et al. (2019). "Wind-blown particulate transport: A review of computational fluid dynamics models". In:

Giudice, A.L. and L. Preziosi (2020). "A fully Eulerian multiphase model of windblown sand coupled with morphodynamic evolution: Erosion, transport, deposition, and avalanching". In: *Applied Mathematical Modelling* 79, pp. 68–84.

Huang, N. et al. (2020). "Large-eddy simulation of sand transport under unsteady wind". In: *Geomorphology* 358, p. 107105.

ISO 14688 (2017). *ISO 14688-1:2017. Geotechnical investigation and testing - Identification and classification of soil*.

Kingdom Of Sand: Photographer Captures Apocalyptic Aerial Photos Of Sand-Covered Roads In The United Arab Emirates (n.d.). URL: https://designyoutrust.com/2018/12/kingdom-of-sand-photographer-captures-apocalyptic-aerial-photos-of-sand-covered-roads-in-the-united-arab-emirates/#.YEpSBuEi048.link.

Kok, J. et al. (2008). "Electrostatics in wind-blown sand". In: *Physical review letters* 100 1, p. 014501.

— (2009). "A comprehensive numerical model of steady state saltation (COMSALT)". In: *Journal of Geophysical Research* 114.

Kok, J.F. et al. (2012). "The physics of wind-blown sand and dust". In: *Reports on progress in physics. Physical Society* 75 10, p. 106901.

Li, B. et al. (2012). "Boundary-layer turbulence characteristics during aeolian saltation". In: *Geophysical Research Letters* 39.

Li, Z. et al. (2014). "A Random Pairing Collision Model (RPCM) for Improving the DEM Simulation of Particle-Bed Collisions in Aeolian Sand Transport". In: *Particulate Science and Technology* 32, pp. 86–93.

LiQiang Kang et al. (2008). "Experimental investigation of particle velocity distributions in wind-blown sand movement". In: *Science in China Series G: Physics, Mechanics and Astronomy* 51, pp. 986–1000.

Liu, X. et al. (2004). "Experimental investigation of the concentration profile of a blowing sand cloud". In: *Geomorphology* 60, pp. 371–381.

National Oceanic and Atmospheric Administration (n.d.). URL: https://www.nesdis.noaa.gov/content/saharan-air-layer-what-it-why-does-noaa-track-it.

Newmark, N. (1959). "A Method of Computation for Structural Dynamics". In:

Pahtz, T., A.H. Clark, et al. (2020). "The Physics of Sediment Transport Initiation, Cessation, and Entrainment Across Aeolian and Fluvial Environments". In: *Reviews of Geophysics* 58.

Pahtz, T. and O. Durán (2016). "Fluid forces or impacts: What governs the entrainment of soil particles in sediment transport mediated by a Newtonian fluid?" In: *arXiv: Geophysics*.

Preziosi, L. et al. (2015). "A multiphase first order model for non-equilibrium sand erosion, transport and sedimentation". In: *Appl. Math. Lett.* 45, pp. 69–75.

Raffaele, L. et al. (2016). "Windblown sand saltation: A statistical approach to fluid threshold shear velocity". In: *Aeolian Research* 23, pp. 79–91.

Sherman, D.J. (2020). "Understanding wind-blown sand: Six vexations". In: *Geomorphology* 366, p. 107193.

Stefan, Catalin (2021). *World Atlas of Sand*. URL: http://www.sand-atlas.com/en/.

Sun, Q. et al. (2001). "DEM Applications to Aeolian Sediment Transport and Impact Process in Saltation". In: *Particulate Science and Technology* 19, pp. 339–353.

The Great Green Wall (n.d.). URL: https://www.greatgreenwall.org/.

Valance, A. et al. (2009). "Granular medium impacted by a projectile: Experiment and model". In: *The European Physical Journal E* 30, pp. 43–54.

Wang, D. et al. (2008). "Statistical analysis of sand grain/bed collision process recorded by high-speed digital camera". In: *Sedimentology* 55, pp. 461–470.

World atlas of desertification (n.d.). URL: https://wad.jrc.ec.europa.eu/.

Xiao, F. et al. (2017). "Sand particle lift-off velocity measurements and numerical simulation of mass flux distributions in a wind tunnel". In: *Journal of Arid Land* 9, pp. 331–344.

Xing, M. (2007). "The harmonious character in equilibrium aeolian transport on mixed sand bed". In: *Geomorphology* 86, pp. 230–242.

Yin, X. et al. (2021). "Splash function for the collision of sand-sized particles onto an inclined granular bed, based on discrete-element-simulations". In: *Powder Technology* 378, pp. 348–358.

You-Xing, C. et al. (2019). "An Experimental Study on Splash Functions of Natural Sand-Bed Collision". In: *Journal of Geophysical Research* 124, pp. 7226–7235.

Zhang, W., J.H. Kang, et al. (2007). "Visualization of saltating sand particle movement near a flat ground surface". In: *Journal of Visualization* 10, pp. 39–46.

Zhang, W., Y. Wang, et al. (2007). "Two-phase measurements of wind and saltating sand in an atmospheric boundary layer". In: *Geomorphology* 88, pp. 109–119.

Zhang, Y. et al. (2020). "A Numerical Study of Aeolian Sand Particle Flow Incorporating Granular Pseudofluid Optimization and Large Eddy Simulation". In: *Atmosphere* 11, p. 448.

Ringraziamenti

Sono molte le persone che voglio ringraziare, non solo per il supporto nei mesi della tesi, ma soprattutto per il supporto in tutti questi anni di studio perchè senza di loro non sarei mai arrivato ad oggi, a scivere queste poche righe per poterli ringraziare.

Abbraccio profondamente mia madre e mio padre e li ringrazio per il sostegno che mi hanno dato in questi anni, per la pazienza nel sopportarmi nei periodi (troppi) in cui sono stato così distratto dallo studio da non accorgermi di quanto meritassero il mio più sincero ringraziamento. Senza di loro davvero non sarei qui. Ringrazio mio fratello, che è stato anche un compagno di viaggio, e di stanza, per questi cinque anni di università. Il suo aiuto e il suo affetto sono stati essenziali, e lo saranno per sempre.

Ringrazio Riccardo e Filippo, i miei più cari amici, coinquilini per poco, e compagni di avventura di sempre. Spero di condividere con voi tutte le mille storie che verranno. Ringrazio Caterina per le sue fondamentali lavate di capo e le lunghe passeggiate, e Margherita, Maria Laura ed Elena, perché sono delle amiche insostituibili. Ringrazio Valeria, che nonostante la lontananza mi è stata vicino. Ringrazio tutto il Gruppo, con cui ho condiviso i momenti spensierati di questi anni.
Ringrazio Luca, Fiallo e tutto il gruppo di amici più pazzo che conosca, perchè senza di loro, le immancabili cene e i racconti del Cricetameron, non ce l'avrei davvero fatta.

Ringrazio Federico, che ho incontrato per caso il primo anno e che da allora è rimasto sempre, nei momenti migiori e soprattutto in quelli peggiori. Ho condiviso con lui questi anni di gioia e fatica, e spero che continui a sopportarmi anche negli anni futuri.

E per ultima, ringrazio Martina. Ringrazio il giorno in cui le ho chiesto di prendersi una birra con me, e ringrazio lei per aver accettato. Da allora è stata la mia migliore amica, la mia più grande confidente, il mio sostegno. A lei devo ogni giorno di felicità che ho passato da allora fino ad oggi, e spero anche nel tempo che verrà. Vorrei ringraziarla per tante cose, ma per fortuna riesce a leggermi con un solo sguardo. Qundi, senza perdermi in chiacchere: grazie.